To the Graduate Council:

I am submitting herewith a thesis written by Jason Fowlkes entitled "Growth of Silicon Microcone/Microcolumn Arrays by Nanosecond Pulsed-Laser Irradiation". I have examined the final copy of this thesis for form and content and recommend that it be accepted in partial fulfillment of the requirements for the degree of Master of Science with a major in Metallurgical Engineering.

Anthony J. Pedraza, Major Professor

We have read this thesis

and recommend its acceptance:

D. H. Lowndes

Carl J. McHargue

Accepted for the Council:

Associate Vice Chancellor and

Dean of the Graduate School

Growth of Silicon Microcone/Microcolumn Arrays by Nanosecond Pulsed-Laser Irradiation

A Thesis

Presented for the

Master of Science

Degree

The University of Tennessee, Knoxville

Jason Fowlkes

August 1999

Dedication

Dedicated to Robert, Vicky, and Robin Fowlkes

Acknowledgements

I would like to thank first and foremost, Dr. Antonio J. Pedraza, for his patience and insight during this work. Dr. Pedraza's criticism was always constructive as to aid my learning experience and for this I am very thankful. Dr. Doug Lowndes and Dr. Chris Rouleau of Oak Ridge laboratory had a huge impact in my work aiding in the form of technical content, answering a plethora of questions, and supplying a large portion of the equipment used.

Doug Fielden, Frank Holiway, Larry Smith, Ray Bellamy, Sandy Maples, Randy Stooksbury, Karla Lawrence, Greg Jones, and Mark Potter were courteous and efficient in their individual assistance and vital in their collective assistance. Of all the individuals listed above, a great number indeed, not one ever treated me with anything but a professional and joyous attitude. I never saw one of these people in a bad mood!

Won-Seok Kim aided in several experiments in this work adding experimental insight and criticism when necessary. Along with his assistance, Won-Seok was a joy to work with and in him I have found a great friend. I would like to thank Neil Oldham for his input during my work as well as several SEM photomicrographs he allowed me to use in this work. Finally, I would like to thank Dr. Carl McHargue and Dr. Hanno Weitering for serving on my thesis committee.

Abstract

A self-organized array of silicon spikes was grown on Si (100) and Si (111) substrates by pulsed KrF laser irradiation. The spike morphology was sensitive to the background gas present during irradiation, the number of laser pulses, the total pressure of the background gas, the partial pressure of gases in a binary gas mixture, and the laser fluence. The spikes that developed during pulsed KrF irradiation in air resembled columns and were so termed "microcolumns". The morphology produced from irradiation in SF_6 gas were termed "microcones". A spike morphology did not develop on Si wafer when irradiation was carried out in Ar, N_2, 5% H_2 – Ar, and He.

The microcone/microcolumn morphology was characterized using SEM, EDS, X-ray diffraction, AES, and scanning profilometry. The microcolumns were found to consist of silicon in the bulk with a small oxygen concentration at the surface. Both the microcolumn and microcone morphologies grew in the direction of the incident laser irradiation. The microcolumn morphology developed strictly in the fluence range of 2.7 – 3.6 J/cm^2. The morphology first appears following 200 – 300 laser pulses as small surface ridges ~ 1 μm high. The microcolumns grow in height as the number of laser pulses increases. The microcolumns saturate in height between 800 – 1 000 laser pulses at 30 – 35 μm. The maximum microcolumn density of ~ 2x10^6 col/cm^2 is achieved between 1 000 and 1 200 laser pulses. The microcolumns are cylindrical with diameters of ~ 2 – 3 μm and have a 2 –3 μm diameter tip at their vertical termination. This tip was the portion of the microcolumn melted by the last laser pulse incident on the Si target.

The microcolumns protruded above the initial Si wafer surface by as much as 10 – 20 μm.

The microcone morphology, produced during laser irradiation in SF_6, developed over the entire fluence range tested of 0.9 – 3.8 J/cm^2. The microcones first developed as surface ridges after 750 – 1 000 laser pulses. The surface ridges produced in SF_6 were of the same size and morphology as the surface ridges that were produced in air. The microcones protruded by as much as 40 μm above the initial wafer surface after 2 000 – 3 000 laser pulses. Each microcone had a 2 – 3 μm spherical tip at its vertical termination. The fully developed microcones produced with 2 000 – 3 000 laser pulses had a complex morphology. The growth of small cones ~ 1 – 3 μm long developed on the microcone sides, the cones grew normal to the primary microcone growth direction and grew as the number of laser pulses was increased.

The microcones/microcolumns were found to grow by a mechanism similar to the VLS mechanism of whisker growth described by R.S. Wagner. [41] The microcones/microcolumns grow by deposition of Si from the vapor phase at the 2 – 3 μm tip that is re-melted with each laser pulse. The Si vapor deposits preferentially at the molten spike tips because of the high accommodation coefficient of the liquid phase compared with the solid phase. However, the vapor phase deposition occurs by a "catalyst-free" VLS mechanism. The laser pulse acts to simultaneously produce the flux of Si required for deposition and melt the tips of the microcolumns and microcones providing the deposition location. Scanning profilometry showed the laser etching of Si to be more efficient in gas environments conducive to spike growth. For instance, the etched depth of Si (100) per pulse was 25x greater in air than in He. Thus, more Si vapor

is available in the plasma plume during irradiation in air than in He. Supersaturation of the liquid tip by the high pressures of Si in the plasma plume surrounding the tip causes the deposition of Si at the Si(s) – Si(l) interface as the liquid attempts to reestablish equilibrium. Therefore, with each laser pulse the liquid tip rises above the wafer surface on a solid Si pedestal.

Table of Contents

Chapter **Page**

1. Literature Review.....1

1.1 Introduction.....1

1.2 Pulsed Laser Ablation.....2

1.2.1 Excimer Lasing.....2

1.3 Laser-Material Interactions.....2

1.3.1 Material Optical Properties.....2

1.3.2 Mechanisms of Absorption.....5

1.3.3 The Nature of a Laser Driven Process.....5

1.4 Laser Ablation Processes.....10

1.4.1 Erosional Sputtering.....12

1.4.2 Cone Attributes.....17

1.4.3 Hydrodynamic Sputtering.....21

1.4.4 Redeposition (A Secondary Mechanism).....28

1.4.5 Vapor Plume Characteristics.....31

1.5 The VLS Whisker Growth Mechanism.....42

1.5.1 VLS Mechanism Description.....42

1.5.2 The Kinetics and Crystallography of VLS Crystal Growth.....44

1.5.3 Instabilities in the Whisker Morphology.....48

1.5.4 VLS Whisker Tip Sharpening.....51

1.5.5 VLS Whisker Crystallography.....51

1.6 The Etching of Silicon Wafer by Molecular Species.....51

1.6.1 High Temperature Etching of Si Wafer by F_2.....51

1.6.2 The Laser Induced Etching of Si by SF_6.....56

1.6.3 The High Temperature Etching of Si by an O_2 Molecular Beam.....57

2. Experimental Procedure.....60

2.1 Sample Preparation Procedure.....60

2.2 Laser Irradiation Procedure.....60

2.3 Post-Irradiation Morphology and Microstructure Characterization Techniques.....65

2.3.1 Scanning Electron Microscopy.....65

2.3.2 Scanning Profilometry.....65

2.3.3 Auger Electron Spectroscopy.....65

2.3.4 X-ray Diffraction.....66

3. Results.....68

3.1 Si Microcolumns Grown in Air.....68

3.1.1 Si Microcolumn Evolution and Growth (0 – 1 200 pulses).....68

3.1.2 Si Microcolumn Growth (> 1 200 pulses).....86

3.1.3 Redeposition during Si Target Etching.....86

3.1.4 Fluence Dependence of the Microcolumn Morphology.....91

3.2 The Chemical Composition and Crystallinity of the Microcolumns.....94

3.3 Silicon Microcolumn Morphology formed in SF_6.....97

3.3.1 Similarities in the Air and SF_6 Microcolumn Morphologies.....100

3.3.2 Temporal Evolution of Si Microcolumns in SF_6.....104

3.3.3 The Fluence Dependence of the KrF – SF_6 Induced Microcone Morphology.....112

3.4 Background Gases not Accessory to Si Microcolumn Evolution and Growth.....113

3.5 The Effect of Background Gas Changes during Irradiation on Preexisting Morphology.....117

3.6 Microcolumn Morphology Changes Induced by an Oxygen Partial Pressure Reduction.....124

3.7 N_2 Removal from the Microcolumn forming Ambient.....124

3.8 The Effect of Reducing the Total Pressure of Air on Si Microcolumn Height.....129

3.9 The Etching of Si Microcolumns by 5% HF Acid.....133

4. Discussion.....135

4.1 The Erosional Sputtering Mechanism.....135

4.2 Hydrodynamic Processes.....136

4.2.1 Hydrodynamic Sputtering.....137

4.2.2 Non-Uniform Surface Heating.....141

4.3 Si Transport via the Vapor Phase and Deposition at the Liquid Microcone/Microcolumn Tips.....148

4.4 The Si Vapor Flux Produced in SF_6 and Air.....155

4.5 Laser-Induced Etching of Si.....156

4.5.1 Etching in SF_6.....156

4.6 The High Temperature Etching of Si by O_2 Gas.....158

4.7 The Geometry of the Si Surface Etch Pits.....158

5. Conclusions.....161

References.....165

Vita.....172

List of Tables

Table **Page**

1.1 Rare gas halide molecules and their highest gain transitions for lasing action. [1, 2]....3

1.2 Non thermal, electronic excitations resulting from laser-light and semi-conductor target interactions....6

3.1 Average, maximum microcolumn height as a function of the total pressure of air present during KrF irradiation of Si (100) wafer....130

List of Figures

Figure **Page**

1.1 The simulated melt penetration as a function of time for c-Si melted with 193 nm laser pulses at various energy densities.....8

1.2 The simulated melt penetration depth plotted against the laser energy density for 248 nm, 32 ns laser irradiation of both a-Si and c-Si.....9

1.3 The c-Si melting threshold as a function of pulse duration for three different excimer laser wavelengths.....11

1.4 This figure illustrates the formation of cones on the surface of Si_3N_4 after many pulses of an excimer laser.....13

1.5 These SEM micrographs show the evolution of the conical topography in Si_3N_4 as a function of fluence and number of shots.....14

1.6 Polyimide Dupont Kapton type-HN film, 125 μm thick, irradiated at 0.040 J/cm^2..15

1.7 Dupont Kapton type-HN films irradiated with 248 nm excimer radiation and a fluence of 0.100 J/cm^2.....16

1.8 The cross-section of a cone that has formed on a YBCO target following pulsed laser irradiation.....18

1.9 Propane gas flame-melted single crystal germanium.....20

1.10 SEM micrograph of 30 keV Ar^+ ion bombardment of Ag (111) surface showing cone growth on a specific grain.....22

1.11 Polycrystalline Au sputtered with 12 ns pulses of ArF radiation with an energy density of 2.5 J/cm^2.....23

1.12 Periodic surface structures produced by irradiating fused silica, SiO_2, with

approximately 50 shots of 248 nm, 500 fs excimer laser.....25

1.13 A schematic illustration of hydrodynamic sputtering.....26

1.14 Single-crystal p-type Si sputtered with 12 ns, 248 nm excimer radiation with an energy density of 6 J/cm^2.....27

1.15 The above SEM sequence shows the evolution of Si columns as the number of 193 nm laser pulses provided to a Si (100) wafer is increased.....28

1.16 Laser induced melt expulsion and vaporization.....32

1.17 A plasma developed over the surface of a steel using a 10.6 μm CO_2 laser.....34

1.18 a) Temporal behavior of a frequency-doubled Nd-YAG laser used to irradiate a silicon target. b) The thermal response from the pulse. c) 288 nm neutral Si signal from 1 J/cm^2 irradiation.....35

1.19 Emission at 5 mm from the silicon target; a) 288 nm neutral Si signal, b) 413 nm Si^+, c) and 318 nm Si^{2+}. E_d = 1 J/cm^2.....36

1.20 Ratio of the time-integrated emission from Si^+ and Si^{2+} states (385.6/386.2 and 455.26 nm, respectively) to the emission from the 390.55 nm neutral Si state as a function of incident KrF laser energy density.....38

1.21 TOF spectrum as a function of distance from the c-Si target for Si nanoparticles. The laser fluence during target ablation was 2 J/cm^2.....40

1.22 c-Si irradiated with 248 nm radiation, laser energy density range 5 – 8 J/cm^2, in 1 Torr of flowing Ar gas.....41

1.23 Schematic illustration of VLS growth from a Au-Si alloy drop.....43

1.24 Whisker growth from many Au-Si eutectic drops. On half of the substrate a 100 Å gold film was deposited.....45

1.25 Periodic arrays of Si nanowires grown using sharp Si spikes as Au/Si alloy droplet locations.....46

1.26 A plot of the impinging flux of atoms vs. supersaturation for a condensation reaction.....47

1.27 A plot of Au-Si supersaturation vs. Au-Si drop diameter. Curve 2 represents a more perfect crystal than curve 3.....49

1.28 Periodic instabilities in diameter in Si whisker growth. The instabilities occur in whiskers with diameters ~ < 50 μm.....50

1.29 Sharpening of a Au-Si whisker using the etch, HF:HNO_3:H_2O, in the ratio 1:40:1..52

1.30 A VLS whisker grown in the [111] direction which was periodically doped during growth with phosphorous.....53

1.31 A VLS whisker that has grown in the [110] direction.....54

1.32 A Si whisker grown by the VLS method in a temperature gradient.....55

1.33 Si (100) wafer etched by a pulsed O_2 molecular beam at 1 123 K. The facets of the pits are of {111} and {113} orientations.....59

2.1 A view looking down on the laser laboratory.....61

2.2 Two color photographs of the equipment attached to the vacuum chamber.....63

3.1 The Si microcolumn forest produced in air using 2 000 laser pulses of energy density 3.0 J/cm^2.....69

3.2 The beginning stages of Si microcolumn formation.....70

3.3 Pulsed laser irradiation of Si (111) wafer produces the same surface features present on Si (100) wafer for low numbers of pulses.....71

3.4 The surface fractures that form at low numbers of laser pulses on the Si wafer surface widen as additional laser pulses are applied to the wafer.....73

3.5 Si microcolumns evolve after 600 KrF pulses in air, which protrude above the initial Si wafer surface.....74

3.6 Profilometry scans taken across the short dimension of a rectangular laser spot on Si wafer at various numbers of shots.....75

3.7 Optical micrograph showing the various surface features resulting from 500 laser pulses.....76

3.8 Surface ridges form as a result of non-uniform heating of the surface during pulsed excimer laser irradiation of Si (100) wafer.....77

3.9 Si (100) wafer irradiated with 600 laser pulses.....79

3.10 The Si microcolumn density plotted as a function of the number of KrF laser pulses in air.....80

3.11 Cone and columns are produced on the surface of laser irradiated Si (100) after 1 000 laser pulses.....82

3.12 Si (100) wafer irradiated with 1 000 KrF pulses.....83

3.13 The microcolumns formed inhomogeneously throughout the pulse range tested, 1 – 20 000 pulses.....84

3.14 A view looking vertically down on the tip of a Si microcone.....85

3.15 In the pulse range; 8 000 > NOP > 3 000, the microcolumn coalesce together to form conical, microcolumn complexes.....87

3.16 Si (100) wafer irradiated with 8 000 laser pulses and an energy density of 2.8 J/cm^2.....88

3.17 The well-defined, rectangular laser spot was formed using 2 000 pulses of fluence 3.6 J/cm^2.....89

3.18 A low magnification view of a laser spot edge.....90

3.19 The Si target resolidified at the same time the particulates deposited on the wafer surface.....92

3.20 The morphology above, produced after irradiation with 1 000 pulses at a fluence of 2.7 J/cm^2, is identical to the surface modification generated with 400 pulses of fluence 2.9 J/cm^2.....93

3.21 A fluence of ~ 4.0 J/cm^2 has produced a topography devoid of Si microcolumns. NOP = 320, PRR = 1 Hz, and BG = air, 1 atm.....95

3.22 EDS spectrum of a Si microcolumn body and a fused silica standard.....96

3.23 Auger electron spectroscopy and ion sputtering were used to probe underneath the microcolumn surface and determine the location of the oxygen concentration detected using EDS.....98

3.24 A diffraction pattern from a Si wafer that was irradiated with 1 000 pulses of energy density 3.4 J/cm^2.....99

3.25 Irradiation in 1 atm SF_6 flowing at 0.20 SCFM with 2 040 KrF pulses produced the morphology above.....101

3.26 A secondary growth occurs on the SF_6 microcones normal to the primary growth direction.....102

3.27 Following 750 pulses in SF_6, the columns have yet to form. The pits shown in the figure have a surface roughness of ~ 4 000 Å.....103

3.28 Topography profiles produced with increasing number of pulses at E_d = 2.9 J/cm^2,

PRR = 3 Hz, and BG = 1 atm SF_6 (< 0.10 SCFM)..... 105

3.29 The waves surrounding the pits interrupt the background PSS. The pits penetrate deep into the wafer..... 106

3.30 A profilometry scan across a laser groove that was produced with 300 KrF pulses in SF_6 gas..... 107

3.31 Pits have formed in the center of the laser irradiated area following 780 pulses each of energy density 1.5 J/cm^2..... 108

3.32 A network of interconnected Si microcones is produced when Si wafer is irradiated with 2 040 laser pulses in SF_6 gas..... 110

3.33 A secondary growth accompanies the primary microcone growth. The arrow points in the direction of the primary microcone growth direction..... 111

3.34 The etching rate of Si (100) in SF_6 increases substantially at fluences greater than or equal to 3.8 J/cm^2..... 114

3.35 1 320 pulses in 5% H_2 – Ar did not produce the microcolumn morphology..... 115

3.36 A plot of the ablation/etch depth vs. the number of laser pulses of Si in air, SF_6, and He..... 116

3.37 The Si wafer was irradiated in two different gas environments. 400 pulses in air at a fluence of 3.1 J/cm^2 produced the surface ridges critical for Si microcolumn evolution. An additional 2 160 pulses in N_2 produced the morphology seen above..... 118

3.38 Si microcolumns grown with numbers of laser pulses between ~ 500 – 1 000 have periodic changes in their diameters that oscillate along each column's length..... 119

3.39 A Si microcolumn that has been wrapped in a sleeve of oxide following a two-stage laser irradiation treatment in air followed by O_2..... 121

3.40 Microcolumn growth in 5% $O_2 - N_2$ has ensued at the preexisting SF_6 microcone tips..... 122

3.41 A schematic representation of the morphology that results when the fully-developed microcone structures are irradiated with 500 KrF pulses in 5% $O_2 - N_2$..... 123

3.42 A higher magnification micrograph of the growth step in a dual microcone – microcolumn..... 125

3.43 Si microcolumns fabricated in 5% $O_2 - N_2$ (left figure) are columnar-like structures with constant column diameters..... 126

3.44 A Si microcolumn formed in 20% $O_2 - Ar$..... 127

3.45 Irradiation in the presence of Ar causes a decrease in the surface ridge density and hence a reduction in the microcolumn density..... 128

3.46 The Si wafer in a) was irradiated in 760 Torr air. $E_d = 2.9$ J/cm^2, NOP = 1 000, and PRR = 2 Hz. Irradiation under the same conditions in 100 Torr air is shown in b). The microcolumn density has decreased as a result of the decrease in total air pressure..... 131

3.47 The Si microcolumns produced in 1 Torr air b) are more cylindrical than those produced in 760 Torr air a). a) $E_d = 2.8$ J/cm^2, PRR = 4 Hz, and NOP = 1 500. B) $E_d = 2.8$ J/cm^2, PRR = 4 Hz, and NOP = 3 000..... 132

3.48 Irradiation with 2 200 pulses in air generated a forest of both Si microcolumns and cones. A 15:00 min. etching procedure followed the irradiation to determine the compositional difference between Si microcolumns and cones..... 134

4.1 A schematic representation of the hydrodynamic sputtering process when the surface asperity height (6 – 8 μm) is greater than the melt depth (~ 900 nm)..... 138

4.2 A schematic demonstration of liquid Si flowing via a surface tension gradient that has formed as a result of an excimer laser pulse..... 144

4.3 The above schematic aids in understanding the "onion-dome" morphology of the tip that resides atop each Si microcone/microcolumn..... 146

4.4 The groove produced in Si (100) wafer from the laser irradiation in SF_6 is more uniform and deep than the groove produced from laser irradiation in He..... 157

4.5 The probability of exciting an SF_6 molecule is increased by multiple reflections that occur in the KrF – SF_6 induced etch pits. Assuming a 25% excitation efficiency of SF_6 by 248 nm laser light, the absorption efficiency of SF_6 will increase by at least 4x in the surface etch pits..... 160

Chapter 1

Literature Review

1.1 Introduction

An excimer laser pulse, 25 ns in duration, incident on a polished target, significantly alters the surface morphology and microstructure. Most notably, from the laser-target interaction, a fluence dependent cone-like morphology forms. This phenomenon has been noted in metals, semiconductors, polymers, and dielectrics. The cone morphology, previously viewed as deleterious in pulsed laser, thin film deposition, due to its direct association with stoichiometry loss, could find uses as light-trapping devices and electron emitters.

The aim of this research is to perform critical experiments for the development of a new model that explains the evolution of cone/column morphologies in silicon, in response to excimer laser irradiation. Current models describing cone growth mechanisms fail to explain the morphological characteristics we have observed in laser ablated silicon. The morphology changes produced during irradiation were analyzed by scanning electron microscopy (SEM), electron dispersive spectroscopy (EDS), Auger electron analysis (AES), X-ray diffraction, and scanning profilometry. The morphology changes were studied as a function of the number of laser pulses, background gas, gas pressure, and the energy density.

1.2 Pulsed Laser Ablation

1.2.1 Excimer Lasing

An excimer laser emits monochromatic pulsed, coherent photons at ultraviolet wavelengths. The excimer lasing process occurs by excitation of rare gas halide molecules through an electric discharge. Voltages of 10-20 kV can produce a pulse of 120 MW/cm^2, which corresponds to a fluence of 3.0 J/cm^2. Table 1.1 lists rare gas halide molecules and their highest gain transitions from electric discharge excitation. The laser transitions occur 10 – 50 ns after the electrical discharge excitation. [1] The transition products are an unbound ground state molecule and an energetic photon, hν. The unbound ground state dissociates in less than 1 ps, thus providing an excitation to ground state lifetime ratio of ~ 10 000 making rare gas halide excitation an efficient source of ultraviolet pulses.

1.3 Laser-Material Interactions

1.3.1 Material Optical Properties

The optical properties of a material determine the amount of electromagnetic radiation it absorbs. The refractive index of a material quantitatively describes the absorption of incident radiation. The refractive index has a real and an imaginary part [1]

$$m = n + ik$$

Both the real and imaginary parts of the refractive index can be determined through the experimental determination of the real and imaginary parts of the dielectric constant [1]

$$\varepsilon(\omega) = \varepsilon_1(\omega) + i\varepsilon_2(\omega)$$

where ω is the frequency of the radiation.

Table 1.1 Rare gas halide molecules and their highest gain transitions for lasing action. [1, 2]

RGH Molecule	Wavelength (nm)
F_2	157
ArCl	175
ArF	193
KrCl	222
KrF	248
XeBr	282
XeCl	308
I_2	342
XeF+	351, 353

Sources :

[1] W. W. Duley, p. 6 and 36 in UV Lasers : Effects and Applications in Materials Science, Cambridge University Press, 1996

[2] E. J. Eliot, p. 48 in Ultraviolet Laser Technology and Applications, Academic Press, Inc., San Diego, 1995

Excimer optical wavelengths are four orders of magnitude larger than the lattice constant of an arbitrary solid material. This large difference allows the use of a macroscopic quantity, such as the complex refractive index, to describe matter's response to ultraviolet light. [3] The reflectivity, R, derived from the material's refractive properties, provides the amount of coupling between laser light and material [3]

$$R = (n-1)^2 - (ik)^2 / (n+1)^2 - (ik)^2$$

Jellison et al. found the reflectivity of Si under 248 nm irradiation to be 0.63 and 0.70 in the solid and liquid, respectively. [4] The solid reflectivity measurement of 0.63 for Si is an average from room temperature to the melting point.

The absorption of the incident radiation as a function of depth can be calculated using the Beer-Lambert Law

$$I(x) = I_o e^{-4\pi kx / \lambda}$$

Where I_o is the incident light intensity and λ is the wavelength of the radiation. The attenuation coefficient is defined as

$$\alpha = 4\pi k / \lambda$$

and the penetration depth of the radiation into the material is α^{-1}. [1] Aspnes et al. found that the absorption coefficient of Si at 300 K at 248 nm excimer wavelength is 1.81×10^6 cm^{-1}. [5] For multiphoton excitations, which occur at high incident photon energies, the attenuation coefficient becomes intensity dependent. The above mathematical relations give quantitative results concerning the amount of radiation absorbed, yet carry no information regarding the mechanisms of absorption.

1.3.2 Mechanisms of Absorption

The primary interactions of laser-light and material are non-thermal. Examples of non-thermal, electronic state transitions are shown in Table 1.2. In semiconductors, electrons are excited to the conduction band from the valence band by absorption of a photon with energy, hν, greater than the band gap energy. This process is termed interband absorption. Intraband absorption occurs when free electrons in the conduction band absorb a photon and are increased to greater energy states within the band.

Electron – electron interactions occur within ~ 10^{-14} s of excitation. [6] Electron plasmas form in the conduction band when high densities of free carriers occupy similar energy states in the band. Electron – electron and electron – plasma interactions establish an effective carrier temperature that is far greater than the lattice temperatures. [7]

Electron – phonon collisions occur 10^{-11} – 10^{-12} s after photon absorption. [6] Heat transfer to the lattice from the electrons leaves the free carriers with energies just above the conduction band. Electrons still have energies greater than the band gap energy when they are located just above the conduction band. This energy is lost when the electron recombines with a hole in the valence band. The recombination energy transfers to a free carrier in the conduction band. [6]

1.3.3 The Nature of a Laser Driven Process

If a gaseous medium is introduced above the surface of a target, and a laser pulse strikes the target, given the proper gas, the laser-activated gas can etch the target. The time required for the reaction step to occur is characterized by τ_r. The laser pulse simultaneously excites electronic states that interact with elementary excited lattice states

Table 1.2 Non-thermal, electronic excitations resulting from laser-light and semiconductor target interactions.

Interband excitations
Excitation of electron-hole pairs with energy greater than the band gap energy, $h\nu > E_g$.
Intraband excitations
Excitation of conduction band electrons to higher energy levels within the same band. [5]
Defects and impurities
Defects and impurities make it possible for photons of energies less than the band gap to excite electrons from the valence band to conduction band. These disruptions of the crystal lattice form permissible states in the forbidden gap by which sub-gap energies can produce a conducting electron-hole pair.
Multiphoton Excitations
High power laser pulses can produce multiphoton excitations. These excitations create virtual states in the forbidden gap, creating more paths for exciting electrical carriers. The efficiency of a given wavelength laser-material interaction is increased via these pathway. [8]

Sources :

[5] D. E. Aspnes and A. A. Studna, *Phys. Rev. B* **27**, 985 (1985)

[8] D. Bauerle, p. 15 - 28, 173 - 190, 251 - 254, and 262 - 264 in Laser Processing and Chemistry, 2nd Ed., Springer - Verlag, Berlin, Heidelburg, 1996

and heating of the target occurs. The thermalization of the excitation energy occurs in a relaxation time τ_T. If the reaction step lags behind the thermalization of lasing energy

$$\tau_T < \tau_r$$

and the process is thermal, or pyrolytic. [8] The opposing case

$$\tau_T > \tau_r$$

leads to a photochemical, or photolytic process. [8] If relaxation times among the two processes are approximately equal, a laser-material interaction characteristic of both can occur. The combined process is termed photophysical.

If adequate laser energy is supplied to a target, both photochemical and thermal processes can yield material removal. This being the case even though heat conduction in the bulk dissipates a significant amount of the absorbed energy. Excimer laser processing can produce temperatures as high as 10^4 K in shallow absorption depths. [8] Shinn estimated the surface temperature of Si irradiated with 248 nm radiation and a fluence of 1.3 J/cm^2 to be 2 700 °C. [12]

Wood et al. developed a melting model for the pulsed laser processing of silicon. [13] Using a 41 ns, full-width, half-maximum (FWHM) XeCl pulse of fluence 3.0 J/cm^2 they calculated the maximum melt-front penetration into silicon to be 0.8 μm. [13] De Unamuno and Fogarassy computed the melt depth in c-Si as a function of time for a laser pulse duration of 50 ns and a laser wavelength of 193 nm (Figure 1.1). [14] Figure 1.2 shows the melt penetration depth as a function of laser energy density for a 248 nm, 32 ns laser pulse. [14]

De Unamuno and Fogarassy also calculated the c-Si melting threshold as a function of the full-width half-maximum (FWHM) pulse duration. [14] Both the simulated and

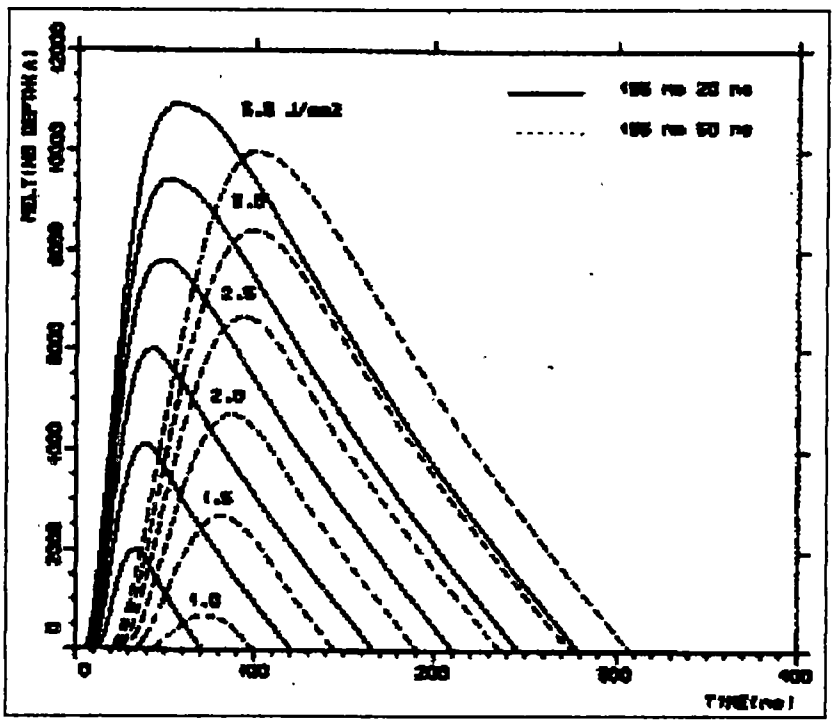

Figure 1.1 The simulated melt penetration as a function of time for c-Si melted with 193 nm laser pulses at various energy densities. The pulse width of the dashed plot was 50 ns and the pulse width of the solid line was 20 ns. [14]

Source :

[14] S. De Unamuno and E. Fogarassy, *Appl. Sur. Sci.* **36**, 1 (1989)

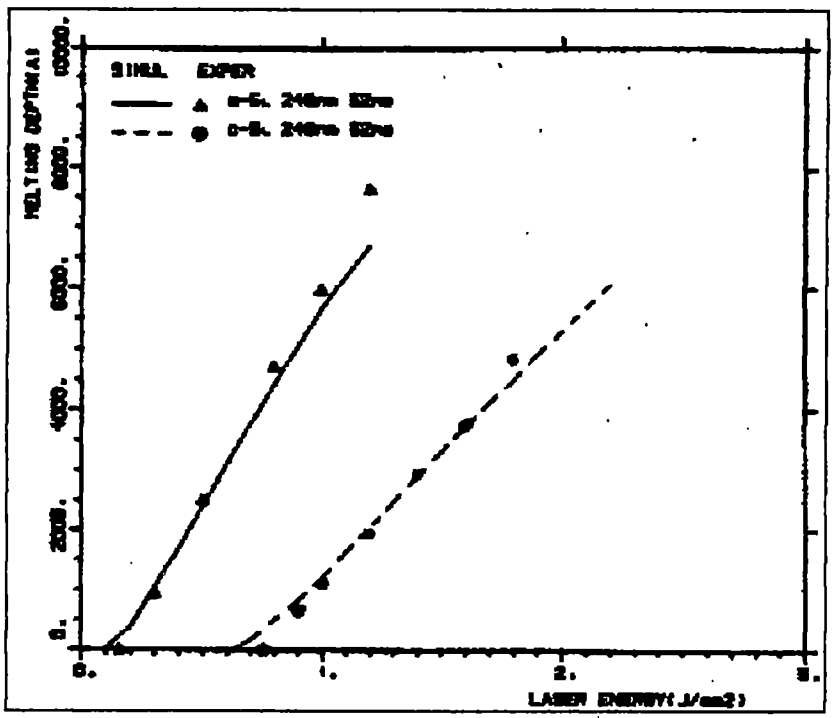

Figure 1.2 The simulated melt penetration depth plotted against the laser energy density for 248 nm, 32 ns laser irradiation of both a-Si and c-Si. Experimental data points are also included in the plot. [14]

Source :

[14] S. De Unamuno and E. Fogarassy, *Appl. Sur. Sci.* **36**, 1 (1989)

experimental data are presented in Figure 1.3. The simulated curve for 248 nm laser irradiation gives a c-Si melting threshold value of ~ 0.55 J/cm^2 for a pulse duration of 25 ns. [14]

Shinn et al. reported ablation, i.e., material removal, of silicon at an energy density as low as ~ 1 J/cm^2 when irradiated with a 14 ns ArF pulse in 1 000 Torr of He. In contrast to these results, Wood and others calculated no vaporization at fluences up to 5 J/cm^2 for 41 ns XeCl radiation. Even considering the longer pulse duration and longer wavelength of a 41 ns XeCl pulse yielding a lower power density, it is hard to imagine such a discrepancy in vaporization energy density for the same material.

Heating rates up to 10^{15} K/s can be generated over a pulse width at FWHM of 20-50 ns. [8] The result of such heating rates is vaporization of the target, expulsion of liquid, thermal shock, and modified microstructure and surface morphology. [15] However, the response to a laser pulse and the form in which that material changes is dictated by the material's properties. Thus, it is a material's properties that ultimately determine the active laser sputtering mechanism.

1.4 Laser Ablation Processes

Miotello and Kelly describe several mechanisms for laser ablation also denoted as laser sputtering. [15] Concentration here will be on laser processes that will promote a surface topography that will be the scope of this work. Erosional sputtering does not describe a truly primary sputtering mechanism but it is rather a description of a surface modification leading to the formation of cones. [15] The second process, hydrodynamic sputtering, is a primary ablation mechanism that also leads to the formation of cones. [15]

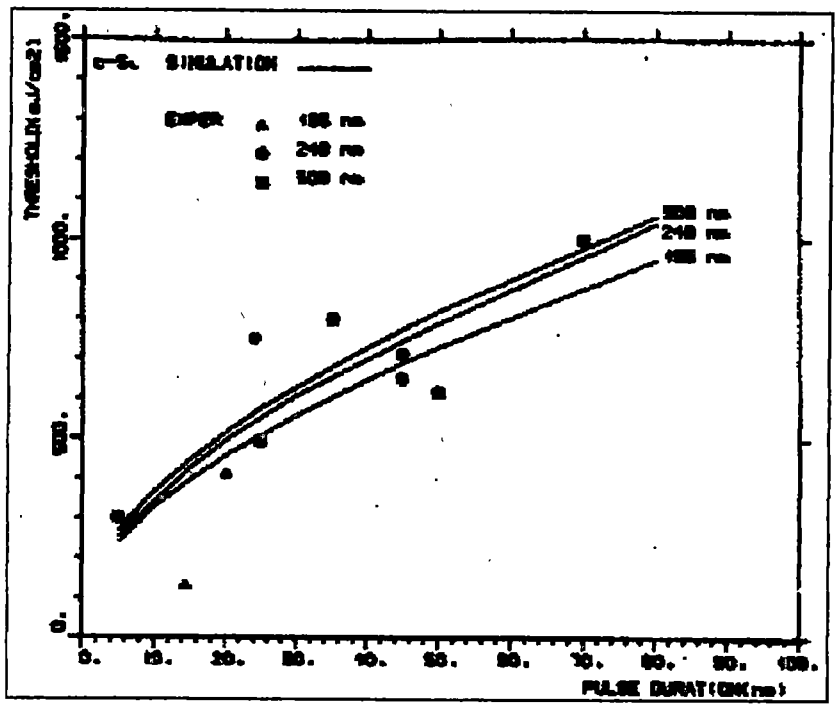

Figure 1.3 The c-Si melting threshold as a function of pulse duration for three different excimer laser wavelengths. Both simulated and experimental data are included in the plot. [14]

Source :

[14] S. De Unamuno and E. Fogarassy, *Appl. Sur. Sci.* **36**, 1 (1989)

Finally, the importance, for the cone morphology formation, of the vapor plume ejected by an irradiation target will be analyzed together with material redeposition on the target.

1.4.1 Erosional Sputtering

One characteristic of erosional sputtering, also known as radiation hardening, is the decrease in ablated material arriving at a mass spectrometer, as the number of pulses is increased. This can be understood considering the following. In many targets laser irradiation promotes, by decomposition of the target material, the formation of a fine dispersion of particulates that are more resistant to laser ablation than the target. Thus, if a laser pulse is applied to the target of an energy density in excess of its sputter threshold yet less than the threshold for ablation of the particulates, the underlying target can be sputtered leaving the surface particulates unmodified. This process is shown schematically in Figure 1.4 for Si_3N_4. The effect of this process is to form "cone-like" structures on the target surface. Figure 1.5 shows SEM micrographs of Si_3N_4 cones and the effects on cone morphology as the fluence and number of pulses are changed. [16]

Figure 1.6 exemplifies the loss in mass spectrometer signal as the number of laser shots increases. The sputtered sample was polyimide, Dupont Kapton type – HN. [17] Initially, the mass spectrometer signal is 4, arbitrary units, and corresponds to a surface morphology similar to the top-left micrograph in Figure 1.7. At 750 shots, the sputtering rate falls to a value of less than 1 and cones, like those at the top-right of Figure 1.7, are formed. As the target material erodes away the surface area continually increases. The erosion eventually halts when the fluence drops below the threshold value due to the surface area increase.

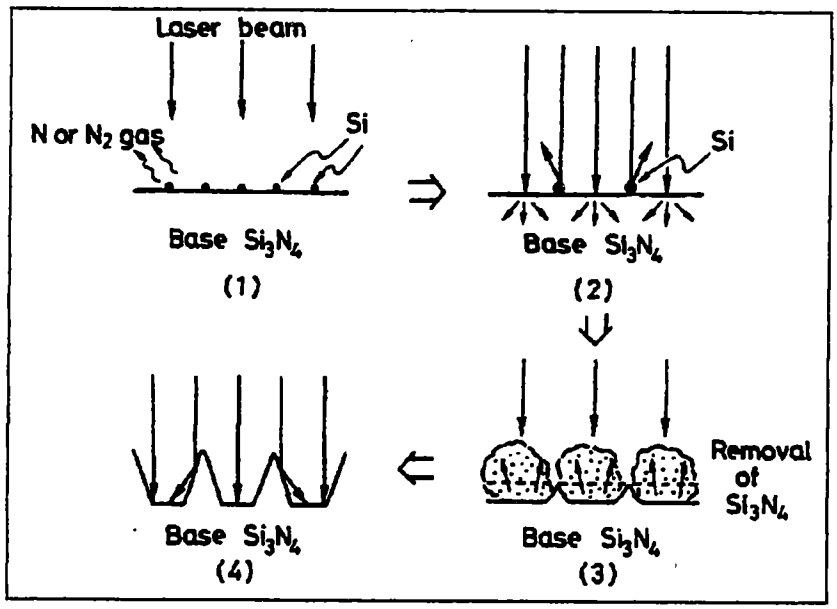

Figure 1.4 This figure illustrates the formation of cones on the surface of Si_3N_4 after many pulses of an excimer laser. At fluences less than 5 J/cm^2 the cones form as the nitride decomposes to nitrogen gas and silicon droplets. The silicon droplets redeposit on the target and successive pulses continue to erode Si_3N_4. However, the Si_3N_4 erodes at a much greater rate than the silicon and a cone morphology develops. In this particular example, the impurities came from the target itself and were not externally introduced. [16]

Sources :

[16] I. Miyamoto and H. Maruo, *Proc. SPIE* **1279**, 66 (1990)

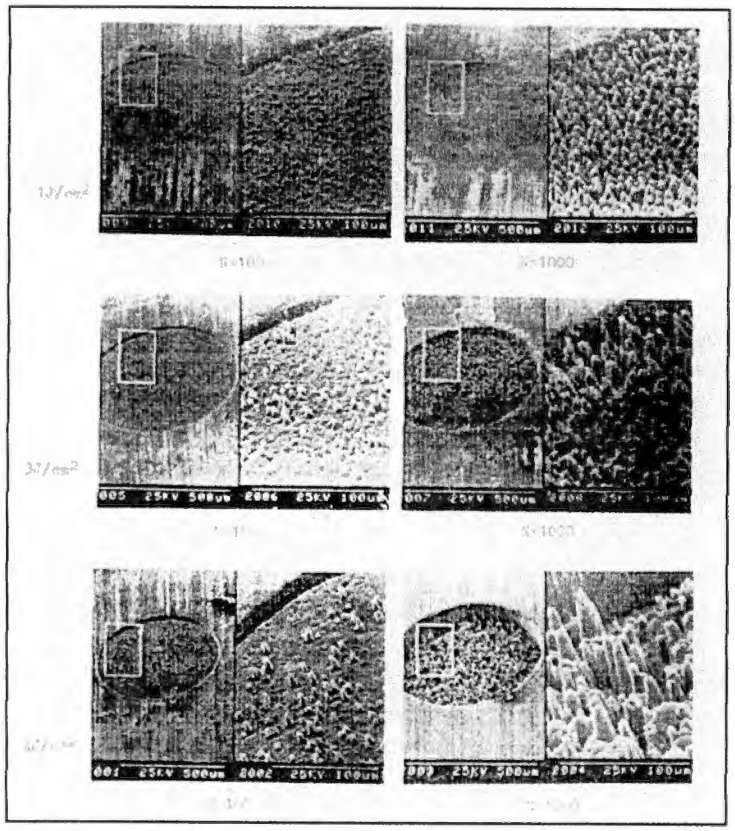

Figure 1.5 These SEM micrographs show the evolution of the conical topography in Si_3N_4 as a function of fluence and the number of shots. As the fluence is increased the number of cones per unit area decreases but their height increases. The cones grow larger in height with increased numbers of pulses. It is relevant to mention that with an erosional sputtering mechanism columns can not break the plane of the original target surface. [16]

Source :

[16] I. Miyamoto and H. Maruo, *Proc. SPIE* **1279**, 66 (1990)

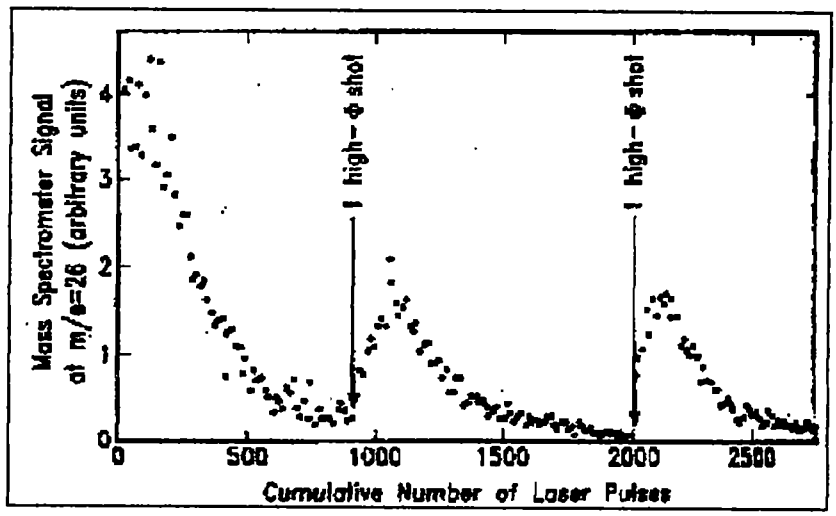

Figure 1.6 Polyimide Dupont Kapton type-HN film, 125 μm thick, irradiated at 0.040 J/cm^2. As the conical surface topography forms and the target becomes radiation resistant, a 0.480 J/cm^2 pulse removes the radiation resistant cones and again significant ablation proceeds. Krajnovich and Vazquez concluded that carbon segregation at the cone tips led to the radiation hardening phenomenon in polyimide. [17]

Source :

[17] D. J. Krajnovich and J. E. Vazquez, *J. Appl. Phys.* **73(6)**, 3001 (1993)

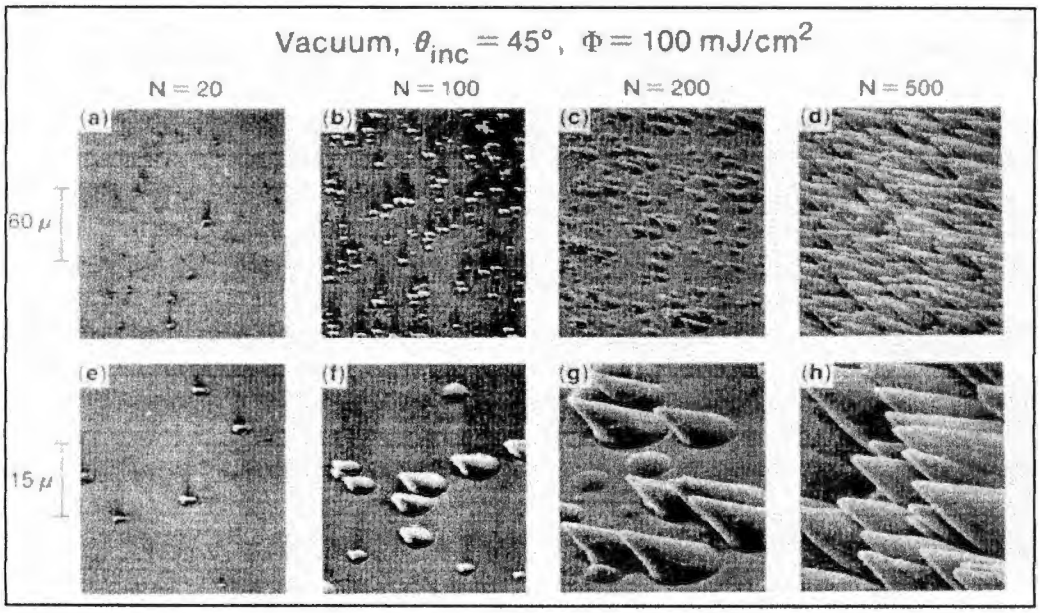

Figure 1.7 Dupont Kapton type-HN polyimide films irradiated with 248 nm excimer radiation and a fluence of 0.100 J/cm^2. The number of pulses increases from left to right in the figure. The laser pulse were incident at 45° off the polyimide surface normal. The cones have grown in this direction. [17]

Source :

[17] D. J. Krajnovich and J. E. Vazquez, *J. Appl. Phys.* **73(6)**, 3001 (1993)

Figure 1.6 shows that removal of the cone morphology has an abrupt affect on the ablation rate. Cumulative laser irradiation of the Kapton type-HN film using an energy density of 40 mJ/cm^2 produced target coning. However, one pulse of 480 mJ/cm^2 removed the cone morphology from the target surface. [17] Continuing irradiation at 40 mJ/cm^2, following the high fluence burst, saw the mass spectrometer signal again increase as the process of cone formation began anew.

The polyimide cones shown in Figure 1.7 arose due to carbon enrichment at the cone tips during laser irradiation. The carbon enrichment raised the ablation threshold at the cone tips preventing material removal from these locations. The 480 mJ/cm^2 pulse ablated both the carbon enriched zone and the polyimide effectively removing the cone morphology. A similar enrichment process occurs in YBCO superconductor when irradiated at ultraviolet wavelengths, Figure 1.8. [18, 19]

The cone morphology has also been formed in an elastomer – carbon black composite by an erosional mechanism. [20] Using KrF laser irradiation, Ono and others found the elastomer to preferentially ablate leaving behind carbon-enriched cones. The cones had good viscoelastic properties, determined under Brinell-loading, and were recommended by Ono for use as sealing and packing materials. [20]

1.4.2 Cone Attributes

The term "cone" properly describes the morphology obtained in YBCO target as illustrated in Figure 1.8. However, this surface topography is characteristic of polymers, insulators, metals, ands semiconductors and can take on many shapes and sizes. As a few examples, cones can have spherical caps at their tops, varying apex angles, cluster

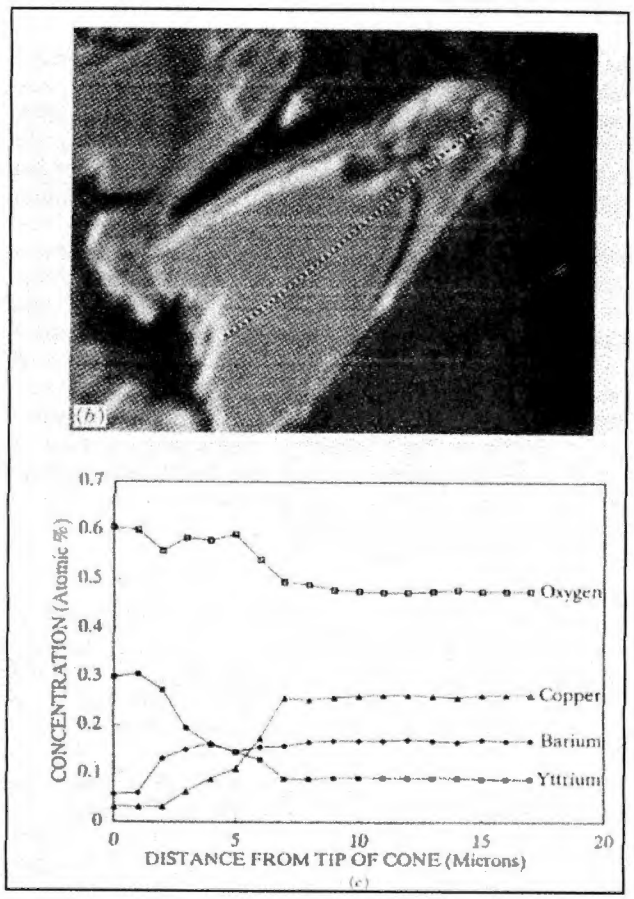

Figure 1.8 The cross-section of a cone that has formed on a YBCO target following pulsed laser irradiation. The affects of fluence are evident in the cross-section sample at the top of the figure. The melt depth at the tip is far greater than the penetration of the laser pulse on the cone sides. There also appears to be a compositional variation between the irradiated and non-irradiated areas referring to the electron probe scan at the bottom of the figure. The scan was taken along the line in the micrograph. During each laser pulse, 2 J/cm^2, a small amount of target is melted but on resolidification higher melting point species such as Y_2O_3 and Y_2BaCuO_5 resolidify first pushing Y and Cu towards the surface. [19] Cu evaporates and after many pulses, in this case 1000 / site, Y segregates to the surface forming a Y - rich layer of higher ablation threshold. Cones subsequently form. Figure from Foltyn et al. 1994. [18, 20]

Sources :

[18] S. R. Foltyn, R. E. Muenchausen, R. C. Estler, E. Peterson, W. B. Hutchinson, K. C. Ott, N. S. Nogar, K. M. Hubbard, R. C. Dyer, and K. D. Wu, *Appl. Phys. Lett.* **59(5)**, 594 (1990)

[19] T. Aselage and K. Keefer, *J. Mater. Res.* **3(6)**, 1279 (1988)

[20] S. R. Foltyn, "Surface Modification of Materials by Cumulative Laser Irradiation", p. 89 - 113 in Pulsed Laser Deposition of Thin Films (D. B. Chrisey and G. K. Hubler, eds.) Wiley - Interscience, New York, 1994

together, etc. [21] Cone height can vary from a few microns up to 10^2 microns and the cone structures point in the direction of the incident laser pulse.

Singh et al. investigated the cone surface morphology, structures they termed laser induced micro-rough structures (LIMS), formed in SiC and YBaCuO superconductor. In the case of SiC they found the micro-rough structures to form in a specific fluence window, namely 2.6 – 3.5 J/cm^2, using 25 ns KrF pulses. [22] Singh and others defined the following general characteristics regarding LIMS; the existence of a specific energy window for LIMS formation, formation in the direction of the incident laser beam, *periodicity of the structures dependent on the periodicity of the surface "holes"*, *ablation/etch pits at SiC grain boundaries*, and evolution based on the number of laser pulses received at a particular area on the target. [22] The cone morphology also forms from energy delivery systems other than excimer laser irradiation.

Partial melting on one end of a single-crystal germanium rod using a propane torch produced a single, sharp cone. [23] Germanium samples melted with high impurity concentrations formed spherical globules at the tips of the cones several microns in diameter. Dickinson et al. found the cone surface morphology to depend strongly on the presence of oxygen during heating and the amount of rod melted. Melting the entire rod produced no cone structure, illustrating the requirement of a liquid – solid interface for cone growth. The presence of oxygen during melting produced a "fractal-like" GeO webbing surrounding the cone formed. [23] Figure 1.9 shows a cone formed by propane melting and the fractal GeO growth. [23]

Bombardment using 30 keV Ar^+ ions produces cones on Ag (111) and Ag (100) monocrystalline material. [24] Ghose et al. found the cone density to be dependent on

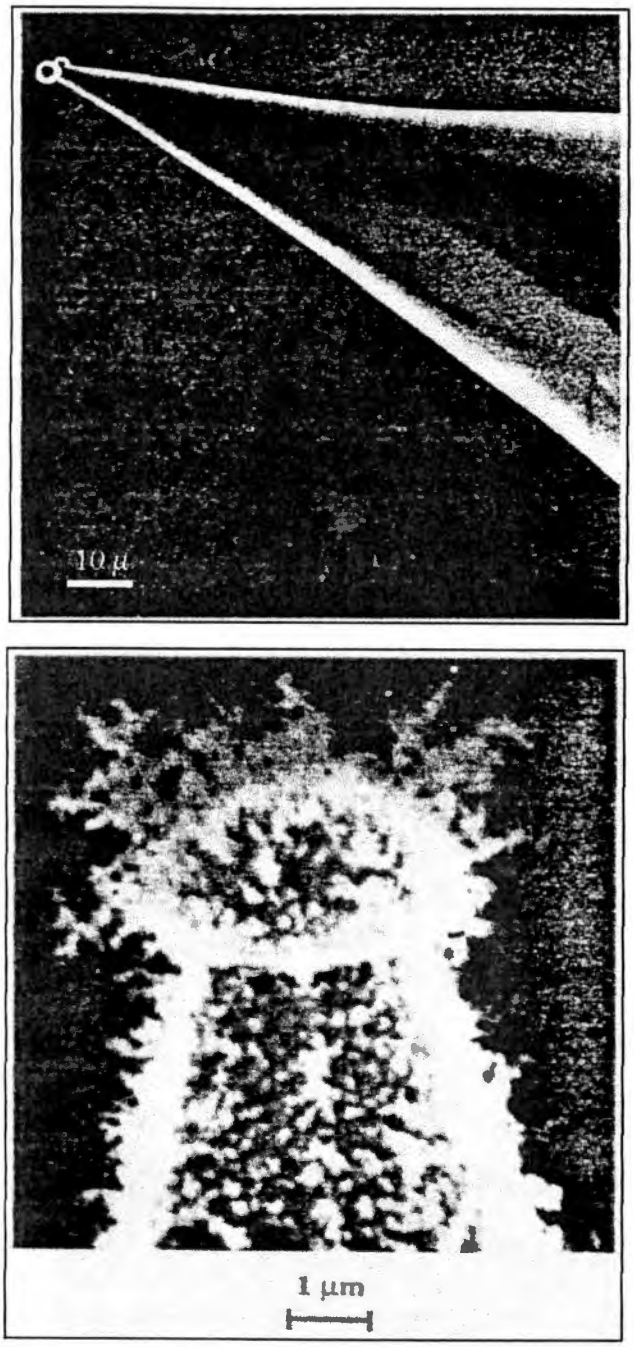

Figure 1.9 Propane gas flame-melted single-crystal germanium. a) SEM micrograph of a cone formed following melting in air. [23] The cone is perpendicular to the rod-end surface normal. b) Following flame-melting, the Ge rod was placed in a furnace at a temperature between 600 - 700 °C, before cooling in air, and a fractal, filamentary growth resulted that surrounds the cone. EDS showed the growth to contain oxygen and Ge.
Source :

[23] M. L. Dawes, J. T. Dickinson, L. C. Jensen, and S. C. Langford, *Nanotechnology* 5, 101 (1994)

the crystal orientation. Figure 1.10 shows the center of Ag (111) surface sputtered with $1x10^{19}$ ions/cm^2. [24]

The cone morphology has been shown to grow in all materials including composites. [18] Radiation hardening from an excimer laser pulse, ion bombardment, and a propane gas torch have all been shown to grow cones in a wide range of materials from metals to superconductors. [17 –19, 23, 24] In addition to radiation hardening, hydrodynamic sputtering is another mechanism conducive to the formation of the cone morphology using an excimer laser pulse. [21]

1.4.3 Hydrodynamic Sputtering

Material accelerated away from a target during an excimer laser pulse due to ultra-fast melting and resolidification is termed hydrodynamic sputtering. [21] Hydrodynamic sputtering requires that surface asperities be present prior to laser irradiation. Subsequent pulses will move each asperity away from the target surface if the following relation holds

$$(4\pi r^3 \rho_l / 3)(\Delta L / \Delta t) > 8\pi r \gamma \Delta t$$

where ρ_l is the density of the liquid, r, the liquid drop radius, and γ is the free energy increase from creation of droplet surface area. [25] The equation states that if the droplet's momentum away from the target exceeds the force-time product arising from increased surface area the droplet will move away from the target. However, due to transient melting, some droplets will be frozen during the expulsion process, Figure 1.11. [25]

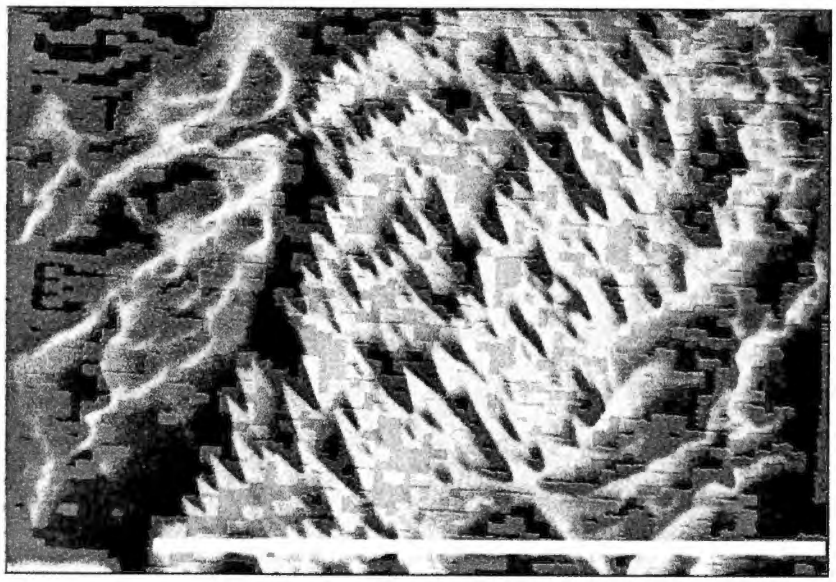

Figure 1.10 SEM micrograph of 30 keV Ar^+ ion bombardment of Ag (111) surface showing cone growth on a specific grain. Each square centimeter received $1x10^{19}$ ions. Scale bar = 1 μm. [24]

Source :

[24] D. Ghose, D. Basu, and S. B. Karmohapatro, *Nucl. Instrum. Meth. Phys. Res.* **B** 1, 26 (1984)

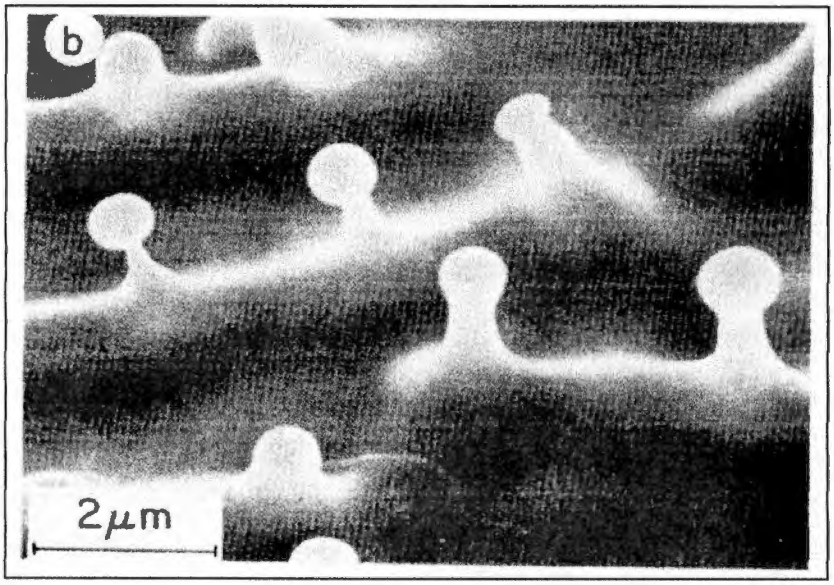

Figure 1.11 Polycrystalline Au sputtered with 12 ns pulses of ArF radiation with an energy density of 2.5 J/cm^2. [25] The expulsion has occurred along PSS, periodic surface structures. The droplets all have diameters of approximately 1 μm and reach several microns above the ridges along which they lie.

Source :

[25] R. Kelly, J. J. Cuomo, P. A. Leary, J. E. Rothenburg, B. E. Braren, and C. F. Aliotta, *Nucl. Instrum. Meth. Phys. Res.* **B9**, 329 (1985)

Examination of Figure 1.11 shows that the expelled droplets lie along laser induced ridges. These ridges are known as periodic surface structures (PSS). PSS are typically spaced periodically along the surface and, in most materials, occur after laser annealing. Figure 1.12 shows complex PSS in fused SiO_2 irradiated with a femtosecond excimer laser. Interference between incident electromagnetic waves and surface polaritons is a currently recognized explanation for PSS formation. [26] A second theory presented by Young et al. explains that capillary waves form by the non-uniform melting of a laser irradiated target surface. [27] In Young's theory, the PSS pattern solidifies in the target during the transient solidification process. [27]

Figure 1.13 shows how the asperity accelerates away from the target surface. If an energy density sufficient to melt the target is applied, the target will melt, and the melt will expand due to the volume change on melting. As the liquid rises in temperature, further expansion occurs due to melt thermal expansion. If the momentum relation above is satisfied, Kelly et al. explains the preexisting asperity will move away from the target surface and concurrently the melt is solidifying toward the wafer surface. The expansion thus solidifies the asperity before it is free of the surface. [25]

In Figure 1.14 single-crystal p-type silicon has been sputtered with 12 ns pulsed 248 nm excimer radiation in vacuum. [28] Using a fluence of 6 J/cm^2, columns, a better term than cone considering their appearance, have been produced which break the original wafer surface plane by approximately 100 μm. Kelly et al. propose that the mechanism of column formation to be hydrodynamic sputtering in view of silicon's high linear expansion coefficient at its melting point. [25, 28] Considering the melt depth during

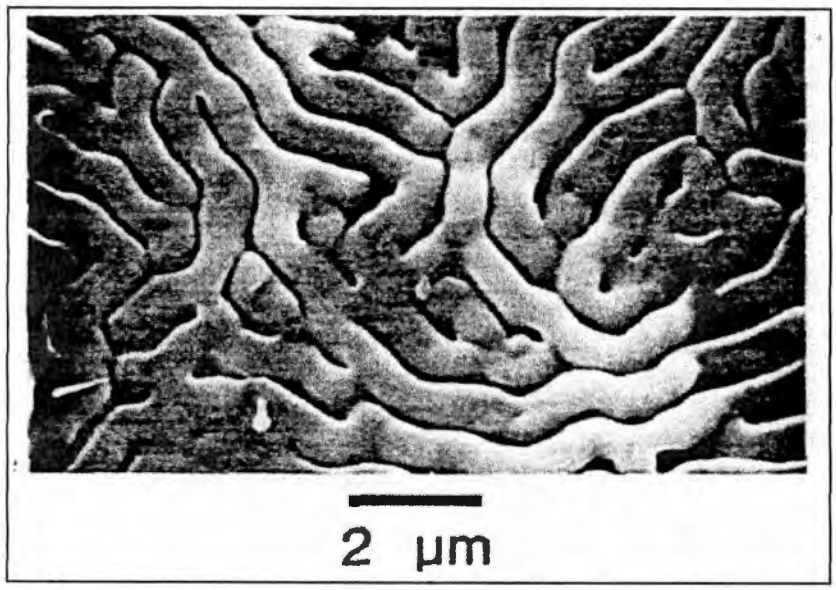

Figure 1.12 Periodic surface structure produced by irradiating fused silica, SiO_2, with approximately 50 shots of 248 nm, 500 fs excimer laser. [26]

Source :

[26] H. Keilmann and Y. H. Bai, *Appl. Phys.* **A29**, 9 (1982)

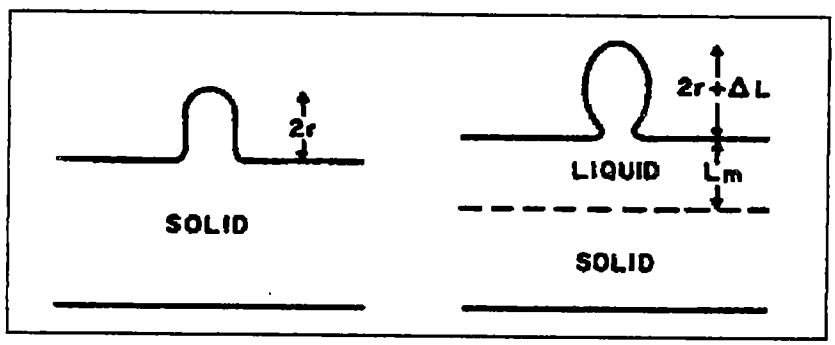

Figure 1.13 A schematic illustration of hydrodynamic sputtering. The left-most schematic shows a solid target surface with a preexisting asperity present. asperity present. Irradiation of this solid with an excimer laser pulse has resulted in hydrodynamic sputtering; the right schematic. The asperity was accelerated away from the target surface due to its momentum away from the surface exceeding the momentum in the opposing direction arising from surface tension. The transient solidification after the pulse was delivered solidified the asperity before it could break free from the target. Both, the expansion accompanying the phase change and thermal expansion were solidified in due to the liquid-solid interface moving towards the surface resulting in the asperity growing away from the target with each laser pulse. [25]

Source :

[25] R. Kelly, J. J. Cuomo, P. A. Leary, J. E. Rothenburg, B. E. Braren, and C. F. Aliotta, *Nucl. Instrum. Meth. Phys. Res.* **B9**, 329 (1985)

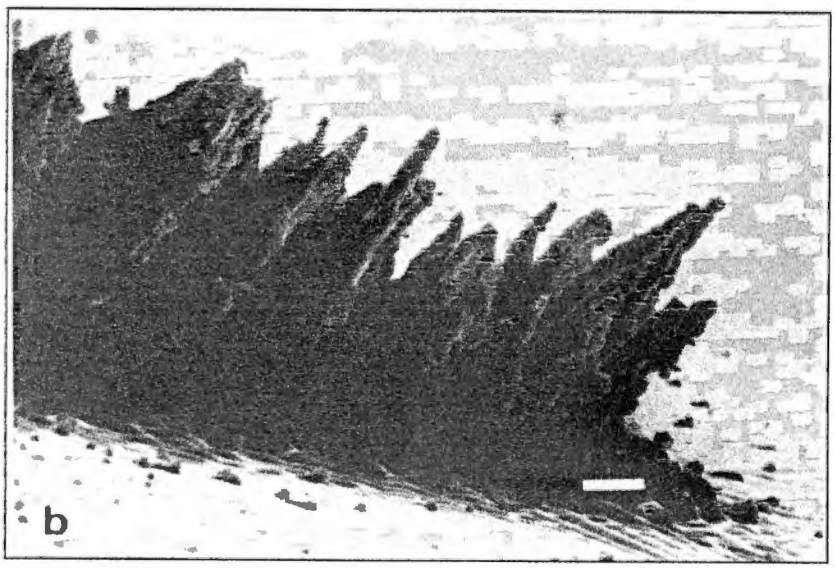

Figure 1.14 Single-crystal p-type Si sputtered with 12 ns, 248 nm excimer radiation with an energy density of 6 J/cm^2. The scale bar shown is 20 μm. [28]

Source :

[28] J. E. Rothenburg and R. Kelly, *Nucl. Instrum. Meth. Phys. Res.*
Aliotta, *Nucl. Instrum. Meth. Phys. Res. B* **1**, 291 (1984)

Kelly's experiment was on the order of a few microns it is hard to imagine such a growth from hydrodynamic effects alone.

Sanchez et al. have observed the formation of whisker-like columns on Si (100) in response to sequential, 193 nm laser irradiation in air. [29] The tall and narrow columns form in a narrow fluence range, 1.5 – 2.5 J/cm^2. The columns are 1 to 2 orders of magnitude taller than the depth of the crater produced during irradiation. [29]

Sanchez et al. attributed the growth of these columns to hydrodynamic processes. Figure 1.15 shows the growth of the columns as the number of pulses is increased. [29] An elevated reticular network forms at numbers of pulses > 200. The formation of this network is ascribed to thermocapillary effects in the shallow, surface melted Si. The reticular network is most prominent in Figure 1.15c. Continued irradiation sees the elevated material draw up to the nodes of the network. Hillocks are then formed at the network nodes (Figure 1.15d) and further ArF irradiation transforms the hillocks into Si columns. [29]

The column growth process as described by Sanchez et al. and Kelly et al. is strictly a hydrodynamic one. However, both Sanchez and Kelly observed redeposition of ablated/etched material around the perimeter of the their laser spots following laser modification of Si. The redeposition of material can be seen in Figure 1.14. [28]

1.4.4 Redeposition (A Secondary Mechanism)

Photons striking a target in vacuum with an energy density just above the sputtering threshold will eject a relatively low density of species. If the density is low enough, species will not interact after ejection and will travel away from the target with,

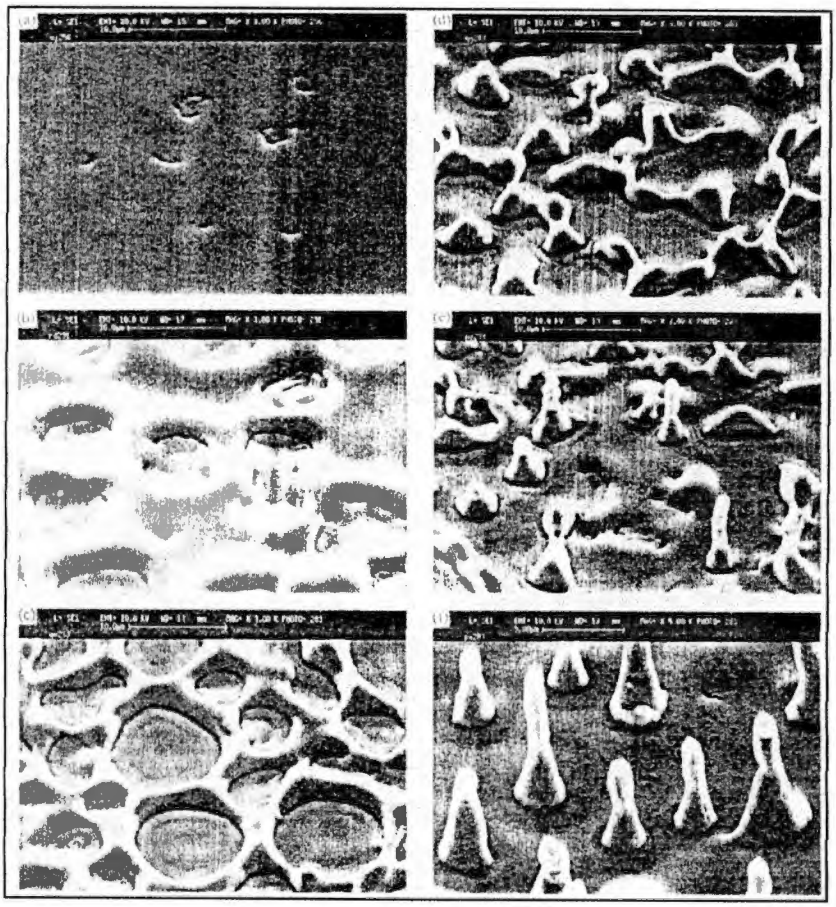

Figure 1.15 The above SEM sequence shows the evolution of Si columns as the number of 193 nm laser pulses provided to a Si (100) wafer is increased. a) Small depressions have formed in the wafer surface after 100 pulses. b) The depressions increase in area. c) As the area of depressions increases a reticular network forms around the depressions. d & e) Hydrodynamic processes cause the network to flow toward the nodes of the network forming hillocks. f) Additional pulses see the hillocks grow and become Si columns. [29]

Source :

[29] F. Sanchez, J. L. Morenza, R. Aguiar, J. C. Delgado, and M. Varela, *Appl. Phys. A* **66**, 83 (1998)

$$v_x > 0$$

the target normal being the x-direction. [15]

A flow velocity can be introduced with either the introduction of a background gas or an increase in the incident energy density. A flow velocity develops when the sputtering rate is approximately 0.5 monolayer/ns. [30] The collisions of ejected species allows the vapor to thermalize and a range of velocities becomes possible, positive or negative

$$\infty > v_x > -\infty$$

The development of a velocity distribution becomes a more rigorous task when flow velocity develops. The use of a shifted Maxwellian becomes necessary

$$F(v_x, v_y, v_z) = C\varepsilon \exp -(m / 2kT)[(v_x - u_k)^2 + v_y^2 + v_z^2]$$

ε is the internal energy term, namely the translational kinetic energy of the species, C is a constant, and u_k is the flow velocity. The k subscript denotes the Knudsen layer. [31, 32] The Knudsen layer is located above the target surface where thermalization of the ejected species occurs. The boundary of the layer is defined as the point in vapor where the sound speed equals the flow velocity. This corresponds to a Mach number of 1

$$M = u_k / a_k$$

From gas dynamics, the sound speed in a perfect gas is [33]

$$a_k = (\gamma k_B T_k / m)^{1/2}$$

The shifted Maxwellian adopted by Kelly et al. results in a fraction of the ejected species being backscattered toward the target. The backscattered particles can either recondense on the target or reflect off. [15]

While in flight, these backscattered species can chemically react with the background gas forming a molecular species. A certain fraction of these species, which can range in size from particulates to nanoparticulates, can redeposit on the target surface. The fraction of species that will redeposit depends on the density of the ablation flux, the background gas pressure, the vapor plume pressure, and the state of the ejected flux, i.e., neutral or plasma.

Depending on the nature of the chemical bond formed, the particle may exhibit ablation resistance to the next laser pulse. Cumulative irradiation will etch the material surrounding the particle forming a cone. Thus, the redeposition of ablated fragments can result in the formation of target cones.

1.4.5 Vapor Plume Characteristics

A primary concern of this work is the availability of species to recondense on the target after ablation/etching. More importantly, a large vapor density will be required such that vapor will have time to eject, collide with other vapor constituents, recondense, and incorporate into the melt before resolidification. Knowledge of the species ejected from the target, their concentrations in the vapor, the kinetic energy of the species, species spatial distribution above the target, and the time evolution of the plume must be known to determine if vapor will incorporate into the melt.

When the energy density exceeds the ablation threshold, material will leave the target and propagate outward, normal to the target. A recoil pressure is generated from the outward flow expelling liquid, as well as vapor, as shown schematically in Figure 1.16. [8] With increased laser light intensity the vapor ejected increases and reaches a point at

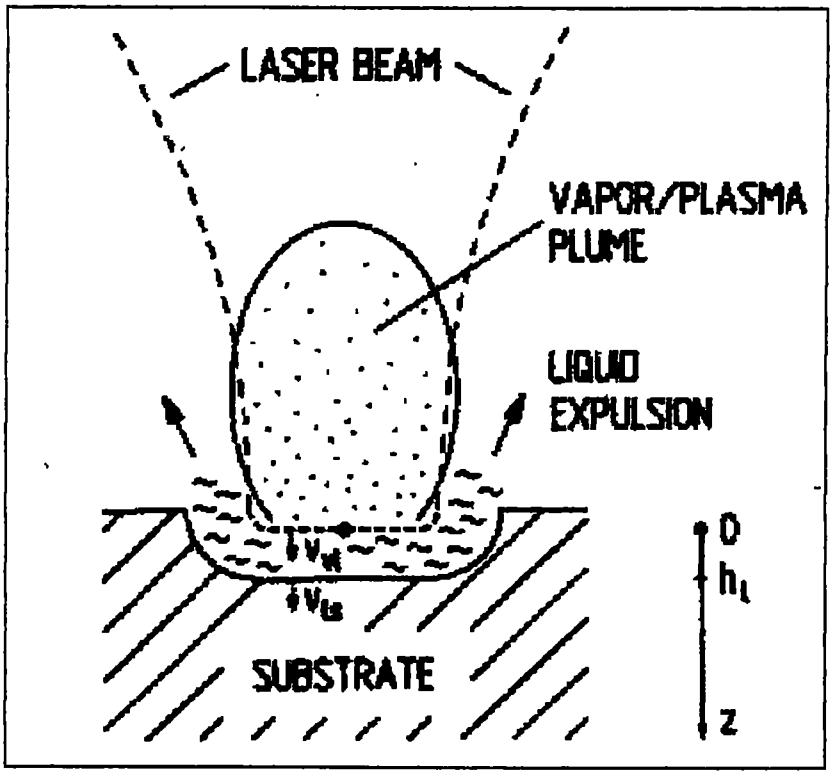

Figure 1.16 Laser induced melt expulsion and vaporization. The melt depth is h_l. [8]

Source :

[8] D. Bauerle, p. 15 - 28, 173 - 190, 251 - 254, and 262 - 264, Laser Procesing and Chemistry, 2nd ed., Springer - Verlag, Berlin, Heidelburg, 1996

which the laser interacts significantly with the vapor. High intensities can be reached with excimer lasers that ionize the vapor plume forming a plasma.

At laser light intensities just under approximately 10^7 W/cm^2 the laser can ionize the plume significantly but the Mach number remains less than 1 restraining the plume from propagating outward; Figure 1.17. [8] In the intensity range 10^{10} W/cm^2 > I > 10^7 W/cm^2 most incident laser light is absorbed in the plume and the target is shielded from a significant portion of the radiation. Here, the flow velocity exceeds the sound velocity and the plume propagates.

Hanabusa et al. excited a silicon target with a frequency-doubled Nd – YAG laser using an energy density of 1 J/cm^2. [34] Optical emission spectroscopy was performed to determine the temporal behavior of the 288 nm emission of vaporized Si_I atoms at the target surface. This plot is shown in Figure 1.18. [34] The emission followed the thermal response of the pulse which decayed off after approximately 100 ns. 288 nm emission measurements 5 mm from the target yielded a neutral silicon velocity of 1.3 ± 0.2 x10^6 cm/s at peak emission. [34] The emission signals at 5 mm are shown in Figure 1.19. [34]

Si_{II} and Si_{III} emissions were also detected 5 mm from the target. Velocities for both species at peak emission were 2.7 ± 0.3 x10^6 cm/s and 4.4 ± 0.5 x10^6 cm/s, respectively. Interestingly, Bialkowski and co-workers found emission from Si, around the melting threshold, ≅ 0.7 J/cm^2, irradiated with KrF to peak at approximately 0.75 μs in contrast to the calculated value of 300 ns. They claim neutral Si forms a Knudsen layer above the target that decelerates ionic species and accelerates neutral Si. [35]

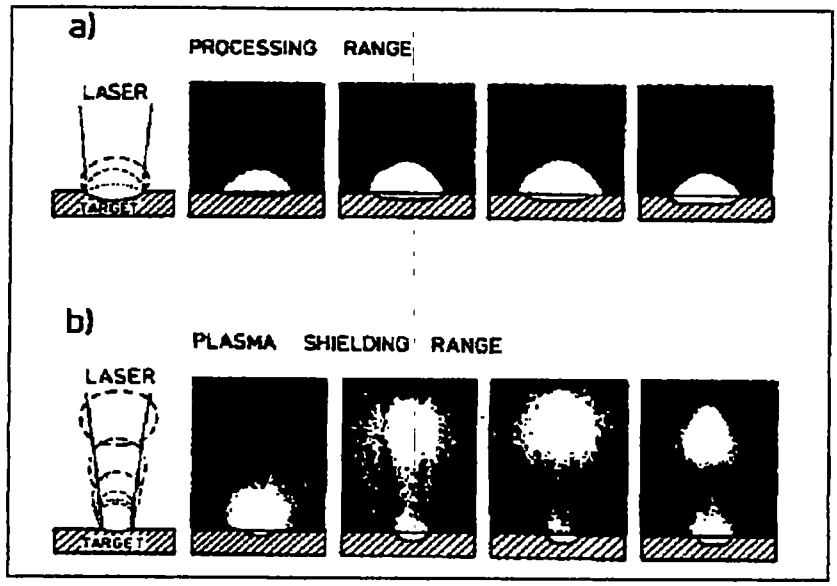

Figure 1.17 A plasma developed over the surface of a steel using a 10.6 μm CO_2 laser. The plume behavior in a) occurs at intensities slightly below 10^7 W/cm^2 with a relatively small concentration of ionized species. b) In the plasma shielding range the time evolution shows the plume advancing away from the target. Here the plasma is ionized sufficiently to partly shield the target from the incident intensity. The intensity range of this behavior is $10^7 < I < 10^{10}$ W/cm^2. [8]

Source :

[8] D. Bauerle, p. 15 - 28, 173 - 190, 251 - 254, and 262 - 264, Laser Processing and Chemistry, 2nd Ed., Springer - Verlag, Berlin, Heidelburg, 1996

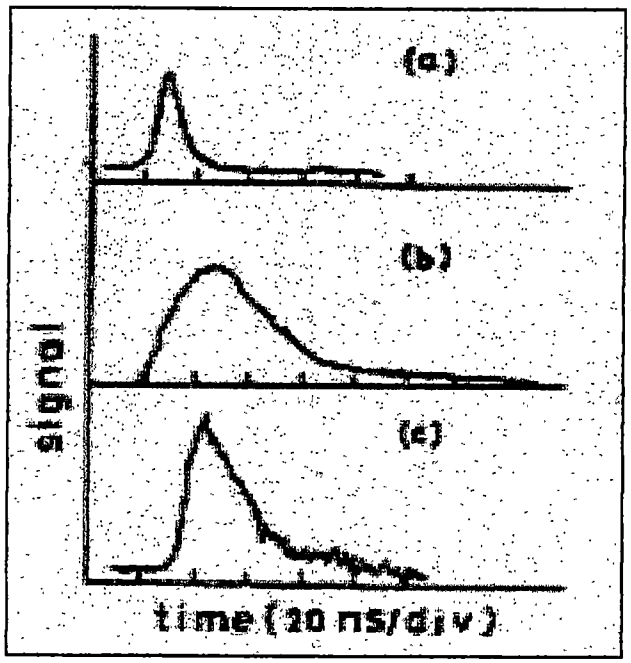

Figure 1.18 a) Temporal behavior of a frequency-doubled Nd - YAG laser used to irradiate a silicon target. b) The thermal response from the pulse. c) 288 nm neutral Si signal from 1 J/cm^2 irradiation. [34]

Source :

[34] M. Hanabusa and M. Suzuki, *Mater. Res. Soc. Symp. Proc.* **4**, 559 (1982)

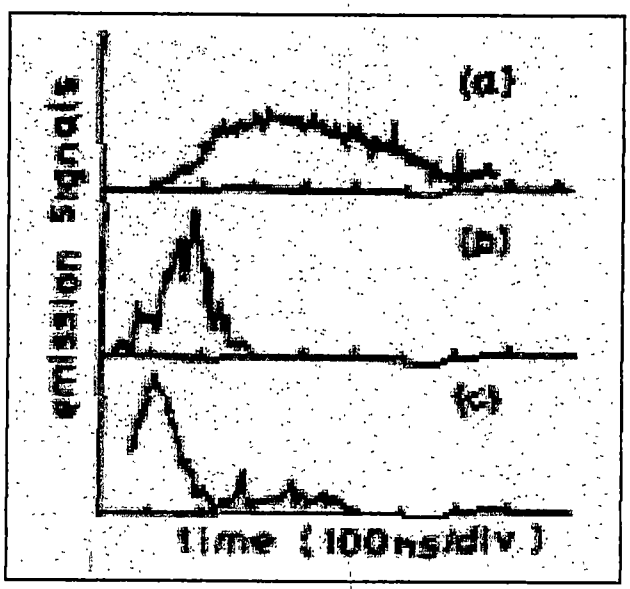

Figure 1.19 Emission at 5mm from the silicon target following pulsed laser ablation with a Nd-YAG laser; a) 288 nm neutral Si signal, b) 413 nm Si^{+}, c) and 318 nm Si^{2+}. $E_d = 1$ J/cm^2. [34]

Source :

[34] M. Hanabusa. And M. Suzuki, *Mater. Res. Soc. Symp. Proc.* **5**, 559 (1982)

Shinn et al. measured relative emission of Si_I, Si_{II}, and Si_{III} from p-type Si (100) wafer at various energy densities shown in Figure 1.20. [12] Emission from all species increased with increasing laser energy density. Hanabusa and co-workers found all ejected species' speeds to be independent of energy density. [34]

The introduction of a background gas affects the propagation of ejected species. Ejected ions can react with the background gas to form molecules that hinder their propagation. [36] The presence of a background gas during irradiation also increases the number of species with negative velocities that can ultimately recondense on the target.

Movtchan et al. studied the optical emission from ejected vapor species when c-Si was ArF irradiated in O_2, He, and Ar. [37] The plasma emission spectra from irradiation in 200 mTorr O_2 with an energy density of 2 J/cm^2 showed intense emission from Si_I and Si_{II} vapor species. Superimposed with the strong atomic and ionic emission bands were weak, broad (~ 10 nm) emission bands. [37] These weak emission bands correlated with a photoluminescence spectrum from a Si – SiO_x nanocluster thin film produced by PLD under the same irradiation conditions. [37]

Le et al. investigated the temperature of ejected Si and SiO by laser-induced fluoresence (LIF) to determine the degree of Si oxidation in flight to the substrate. [38] Knowledge of the degree of oxidation in the vapor phase during PLD aids in controlling the composition and size of the nanocluster thin film produced. They found the oxidation of SiO to occur in the temperature range 400 – 2 000 K. [38] Le and others concluded that the laser pulse dissociates the O_2 molecule, the Si and O atoms interdiffuse in the vapor, and the Si and O chemically react as

$$Si^* + O^* + M^* \rightarrow SiO^* + M^*$$

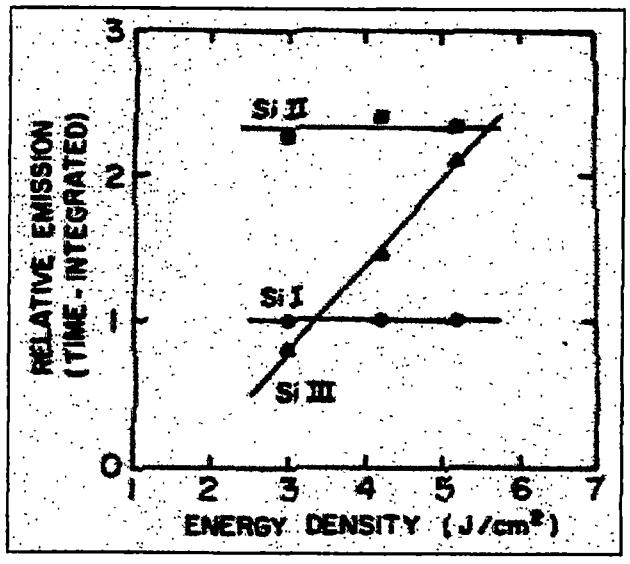

Figure 1.20 Ratio of the time-integrated emission from Si^{+} and Si^{2+} states (385.6/386.2 nm and 455.26 nm, respectively) to the emission from the 390.55 nm neutral Si state as a function of incident KrF laser energy density. [12]

Source :

[12] G. B. Shinn, F. Steigerwald, H. Stiegler, R. Sauerbrey, F. K. Tittel, and W. L. Wilson Jr., *J. Vac. Sci.Technol.* **B 4(6)**, 1273 (1986)

where M is a background gas molecule that absorbs some of the binding energy and the asterisk denotes that the products can be in the ground or excited state. [38]

Si – SiO_x nanocluster emission band maxima, determined from time-of-flight spectrum, revealed that some of the nanoclusters formed in the vapor phase were backscattered back toward the Si target. The first emission maximum detected represented the initial flux of nanoclusters expanding away from the Si wafer. Figure 1.21 shows that the detection time of the initial flux increases as the emission probe was moved further away from the Si wafer target. [37]

The time required to detect the second emission maximum *decreased* as the emission probe – target distance was increased. (Figure 1.21). Movtchan et al. attributed this result to the probe actually moving *closer* to the backscattering point in the plasma of the nanoclusters. [37] Movtchan et al. observed the target microscopically following a thin film deposition operation and found a considerable amount of redeposited nanoparticles on the Si wafer target. [39] The existence of the two nanoparticle flux were verified using a gated fast ICCD camera to monitor the plume expansion. [37]

Similar time-resolved imaging of visible plasma luminescence from ablated c-Si has been performed by Geohegan et al. [39] In Figure 1.22 the visible plasma luminescence at various times after laser irradiation are shown for c-Si wafers ablated with KrF laser pulses in the fluence range 5 – 8 J/cm^2 in 1 Torr Ar gas. After 20 μs collisions of the plume species with the background gas has slowed its velocity from 2 cm/μs to 0.01 cm/μs. [40] Following 300 μs the plume has reflected off the target surface.

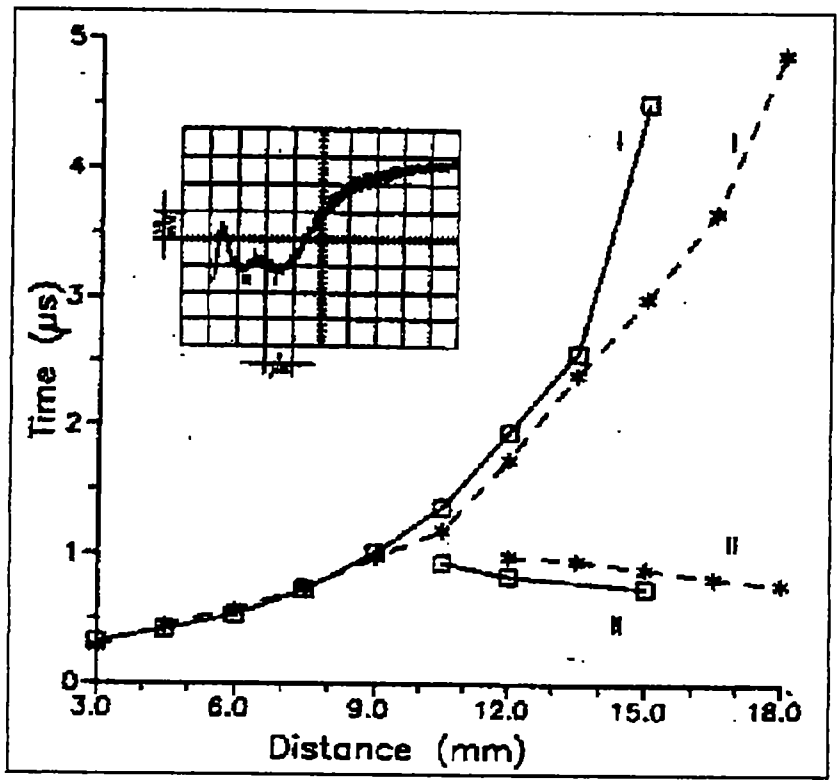

Figure 1.21 TOF spectrum as a function of distance from the c-Si target for Si nanoparticles. The laser fluence during target ablation was 2 J/cm^2. The dashed line corresponds to a 245 mTorr O_2 background gas pressure and the solid line a 375 mTorr O_2 pressure. The inset TOF signal shows the existence of two emission maxima during a particular ablation experiment at a set distance from the target. The first maxima corresponds to the initial nanoparticle flux. At increased distance from the target the appearance of this maximum is delayed in time. (Plot I) The second flux maximum registers faster as the target - probe distance is increased. (Plot II) This suggests the nanoparticles in flux II are backscattered toward the target from a particular point in the plasma. [37]

Source :

[37] I. A. Movtchan, W. Marine, R. W. Dreyfus, H. C. Le, M. Sentis, and M. Autric, *Appl. Sur. Sci.* **96 - 98**, 251 (1996)

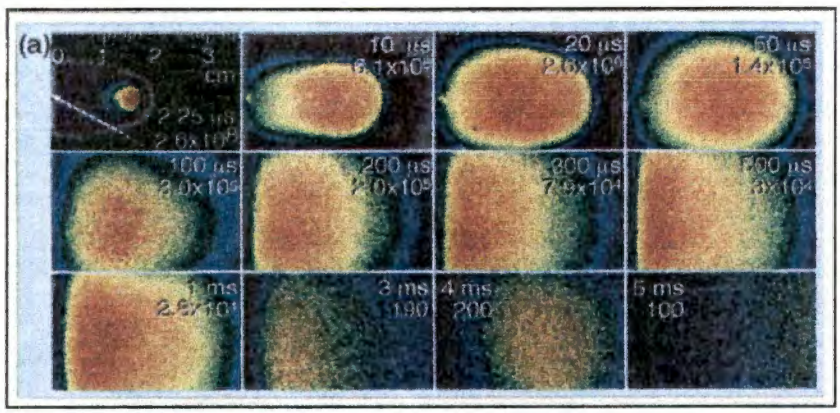

Figure 1.22 c-Si irradiated with 248 nm radiation, laser energy density range 5 - 8 J/cm^2, in 1 Torr of flowing Ar gas. The plume loses most of its kinetic energy after 20 µs in colliding with the background gas. After 300 µs the plume has reflected off the target. [40]

Source :

[40] D. B. Geohegan, A. A. Puretzky, G. Dusher, and S. J. Pennycook, *Appl. Phys. Lett.* **73(4)**, 438 (1998)

1.5 The VLS Whisker Growth Mechanism

1.5.1 VLS Mechanism Description

Silicon whiskers of high aspect ratio are grown from the vapor phase via a vapor-liquid-solid mechanism (VLS). Wagner and Ellis first recognized this mechanism at the Bell laboratory in 1964. [40] Whiskers grown by this mechanism are used in electron field emission applications where a reduction in the whisker tip diameter can yield attractive emission results.

The VLS mechanism requires the formation of a low melting point eutectic alloy consisting of an impurity element and the desired element for whisker growth. The system that will be considered here is silicon whiskers grown using gold as an impurity. A thin gold film ~ 50 Å thick is deposited on a single crystal silicon substrate and heated such that the film breaks up into small islands. The silicon whiskers will grow from these small islands. Thus, the whisker diameter will be equal to the prior gold island diameter.

Gold is chosen as the impurity because it forms a eutectic alloy with silicon and it has a melting point much lower than that of silicon. The melting point of pure gold and pure silicon is 1410 °C and 1065 °C, respectively. [42] Silicon and gold form a eutectic just under 400 °C (Figure 1.23). [43]

A schematic diagram of VLS crystal growth is shown in Figure 1.23. [44] The liquid islands of gold on the solid, silicon substrate will come to equilibrium with the Si substrate via diffusion, forming a Au-Si liquid alloy. The composition of the Au-Si eutectic alloy is dictated by the Au-Si phase diagram.

Introduction of $SiCl_4$ and H_2 gases above the substrate will result in hydrogen reduction at the liquid eutectic surface. Adjustment of the total gas pressure to

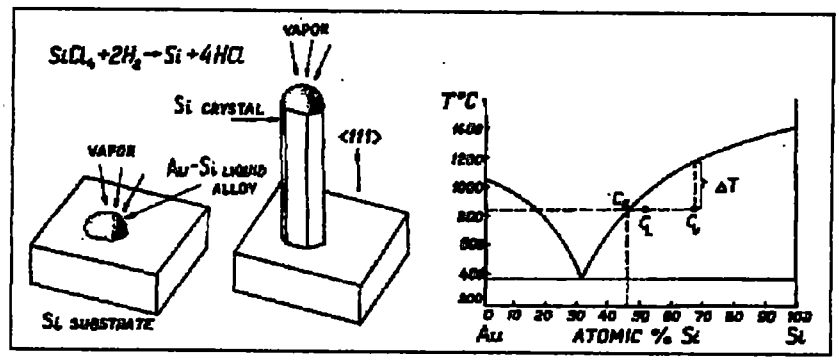

Figure 1.23 Schematic illustration of VLS growth from a Au-Si alloy drop. C_v is the concentration of Si at the vapor-liquid interface and C_L the concentration near the solid-liquid interface. Both exceed the equilibrium solubility of silicon at this temperature forcing Si to deposit at the solid-liquid interface. This lifts the drop away from the substrate surface forming the whisker. [44]

Source :

[44] E. I. Givargizov, "Growth of Whiskers by the Vapor-Liquid-Solid Mechanism" , p. 79 - 145 in Series : Current Topics in Materials Science, Vol. 1 (E. Kaldis, ed.) North - Holland, Amsterdam, 1978

supersaturate the liquid Au-Si drop with silicon will result in silicon deposition at the $Si_{substrate}$ – $[Si\text{-}Au]_{liquid}$ interface. A constant pressure of $SiCl_4/H_2$ over the substrate will result in the liquid drop raising above the substrate surface as more and more Si deposits at the solid-liquid interface (Figure 1.24). Whiskers grown by the VLS mechanism are unidirectional, as shown in Figure 1.24, due to anisotropy in the solid-liquid interfacial energy. [44] Westwater et al. have fabricated periodic arrays of Si nanowires in (111) wafer patterned by etching, gaseous and aqueous, of SiO_2, followed by an Au-Si alloy VLS mechanism. [45] These arrays are shown in Figure 1.25.

1.5.2 The Kinetics and Crystallography of VLS Crystal Growth

Examination of Figure 1.24 illustrates that the normal growth rate of the whiskers far exceeds the lateral growth rate. This stems from the accommodation coefficient being ~ 1 for a deposition of vapor on liquid, and << 1 for vapor deposition on solid. [46, 47] For a condensation reaction, from gas kinetics, the crystal growth rate can be written as

$$J = \alpha\sigma p_o(2\pi mkT)^{-1/2}$$

α being the accommodation coefficient and σ, the supersaturation of vapor. The accommodation coefficient consists of two parts

$$\alpha = \alpha_1\alpha_2$$

α_1 is the probability of atoms adsorbing to a surface and α_2 the probability the adsorbed atom will incorporate into the growing lattice. Figure 1.26 shows, for a constant crystal growth rate, the degree of supersaturation required for vapor – solid (VS) deposition is far greater than for a vapor – liquid (VL) crystal.

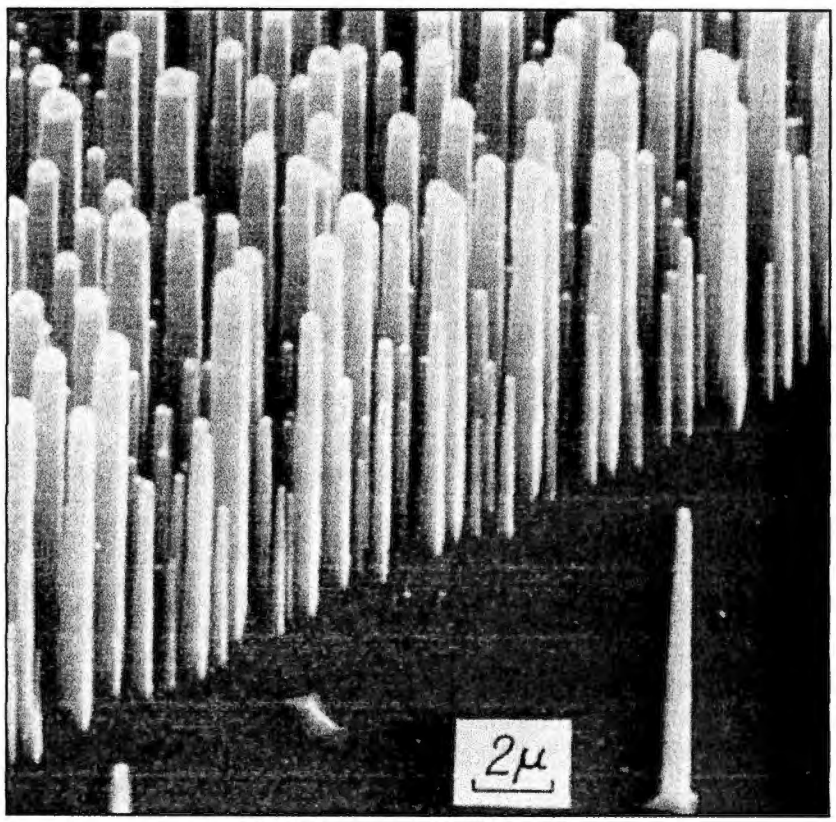

Figure 1.24 Whisker growth from many Au-Si eutectic droplets. On half of the substrate a 100 Å gold film was deposited. As the temperature of the substrate was increased the gold film broke into islands from surface tension. Temperatures were adequate to initiate diffusion ensuring each gold drop became a Au-Si eutectic. Individual whiskers grew from each island. [44]

Source :

[44] E. I. Givargizov, "Growth of Whiskers by the Vapor-Liquid-Solid Mechanism" , p. 79 - 145 in Series : Current Topics in Materials Science, Vol. 1 (E. Kaldis, ed.) North - Holland, Amsterdam, 1978

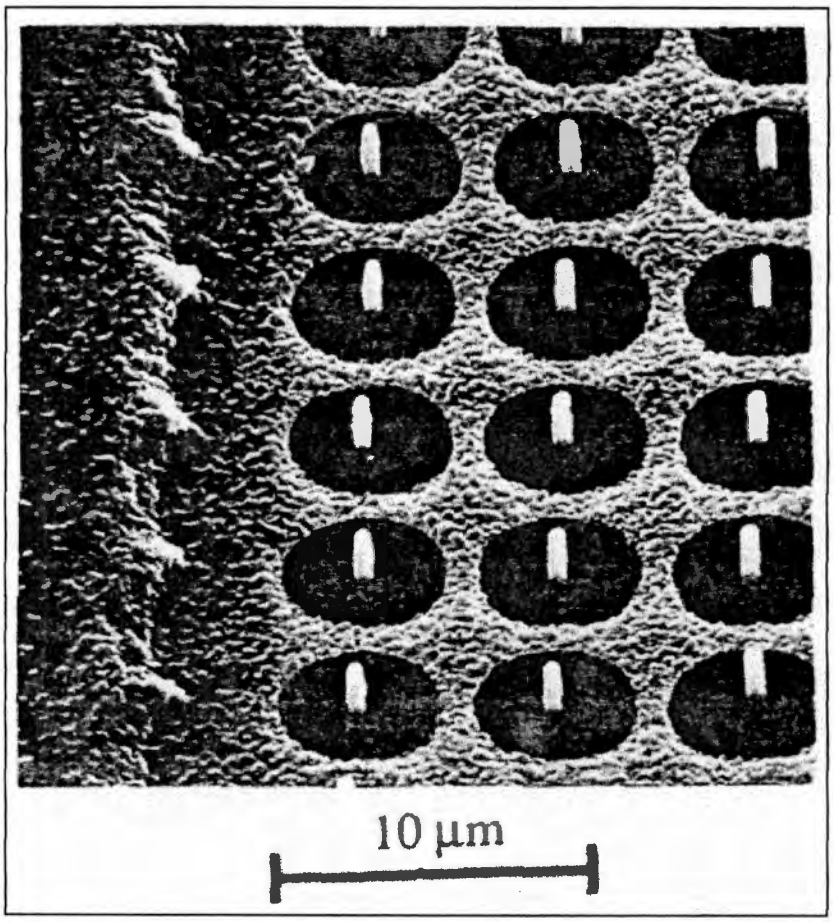

Figure 1.25 Periodic array of Si nanowires grown using sharp Si spikes as Au/ Si alloy droplet locations. The arrays were patterned on an Si wafer using a SF_6 plasma etch and KOH anisotropic wet etch. [45]

Source :

[45] J. Westwater, D. P. Gosain, and S. Usui, *Jpn. J. Appl. Phys. Vol.* **31**, *pt. 1, no. 10* (1997)

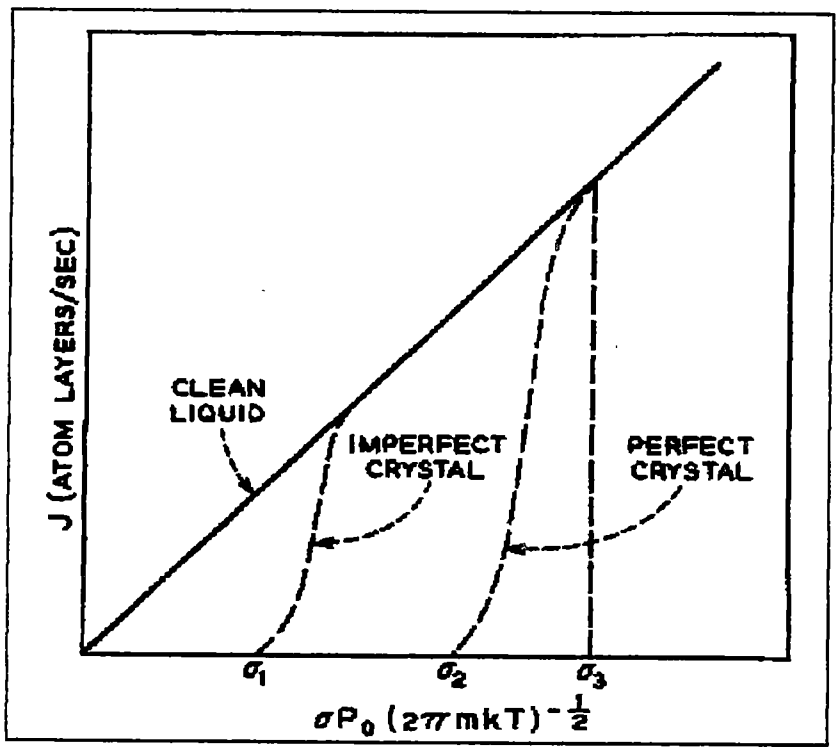

Figure 1.26 A plot of the impinging flux of atoms vs. supersaturation for a condensation reaction. For a clean liquid, the accommodation coefficient is one and any supersaturation deposits crystal forming atoms. A solid surface with a dislocation or a perfectly smooth nucleation surface require considerable supersaturation before vapor will incorporate. [44]

Source :

[44] E. I. Givargizov, "Growth of Whiskers by the Vapor-Liquid-Solid Mechanism", p. 47 - 145 in Series : Current Topics in Materials Science, Vol. 1 (E. Kaldis, ed.) North - Holland, Amsterdam, 1978

The Gibbs-Thompson effect limits the minimum eutectic drop radius attainable in the VLS process. The Gibbs-Thompson equation is

$$\Delta\mu / kT = \Delta\mu_o / kT - [4\Omega\alpha_{vs} / kT][1 / d]$$

where $\Delta\mu$ is the difference in chemical potentials of Si in the vapor and in the crystal, $\Delta\mu_o$ is the same difference for a perfectly smooth, planar interface, Ω is the atomic volume of Si, and α_{vs} is the specific free energy of the whisker surface. The critical diameter, or minimum diameter, d_c, occurs when $\Delta\mu / kT = 0$ or

$$\Delta\mu_o / kT = [4\Omega\alpha_{vs} / kT][1 / d_c]$$

This can be understood physically considering Figure 1.27. [44] For either curve in the figure, a decrease in the tip diameter will decrease the amount of real supersaturation available at the tip. A critical diameter is reached where the equilibrium solubility, at a particular temperature, becomes so high the tip can not supersaturate to deposit. Figure 1.27 also shows that the more apt a surface is to accommodate vapor, curve 3 as opposed to curve 2, the smaller the critical diameter.

1.5.3 Instabilities in the Whisker Morphology

Interestingly, VLS whisker growth can show periodic instabilities in diameter. [48] Figure 1.28 shows periodic instabilities in VLS whisker growth. [44] These instabilities depend on whisker diameter and disappear when whisker diameters are approximately > 0.5 μm.

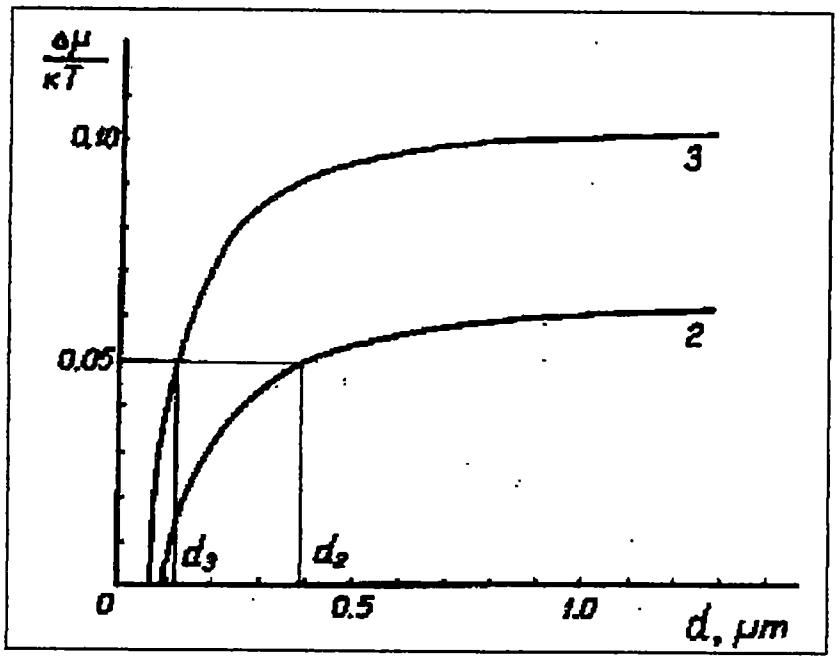

Figure 1.27 A plot of Au-Si supersaturation vs. Au-Si drop diameter. Curve 2 represents a more perfect crystal than curve 3. Both substrates have minimum diameters fixed by the Gibbs-Thompson effect, i.e., at a critical eutectic drop diameter, the drop is unable to supersaturate and therefore unable to grow. The plot also shows that the larger the eutectic drop diameter, the higher a whisker will grow. [44]

Source :

[44] E. I. Givargizov, "Growth of Whiskers by the Vapor-Liquid-Solid Mechanism", p. 47 - 145 in Series : Current Topics in Materials Science, Vol. 1 (E. Kaldis, ed.) North - Holland, Amsterdam, 1978

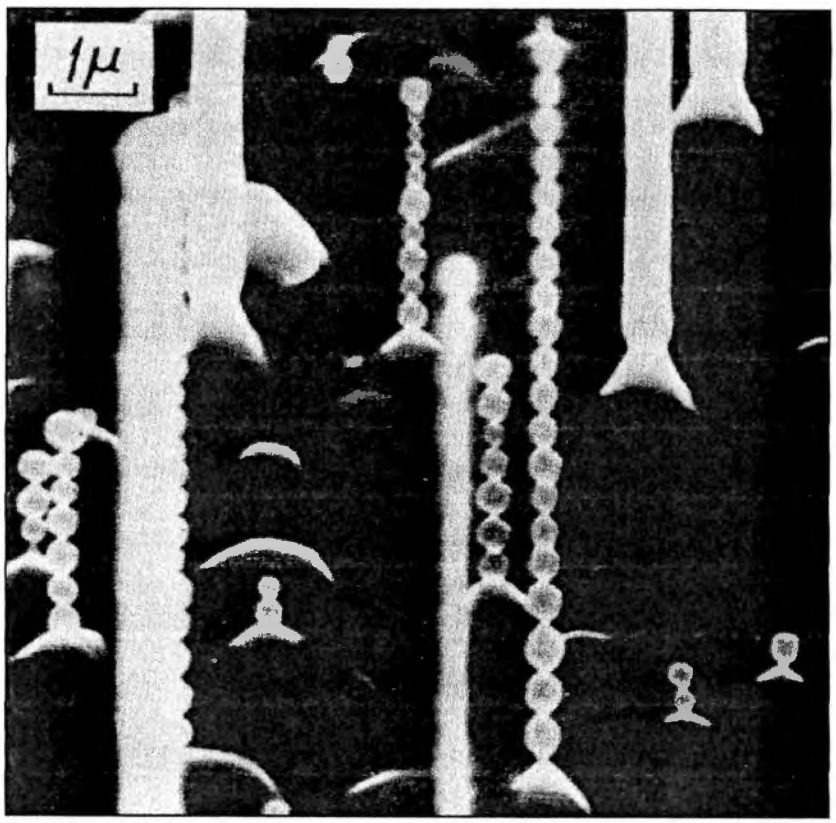

Figure 1.28 Periodic instabilities in diameter in Si whisker growth. The instabilities occur in whiskers with diameters ~ < 0.50 μm. [44]

Source :

[44] E. I. Givargizov, "Growth of Whiskers by the Vapor-Liquid-Solid Mechanism" , p. 45 -145 in Series : Current Topics in Materials Science, Vol. 1 (E. Kaldis, ed.) North - Holland, Amsterdam, 1978

1.5.4 VLS Whisker Tip Sharpening

An etching procedure can supplement VLS growth to produce nanometer tips for field emission. An etch of $HF:HNO_3:H_2O$, ratio 1:40:1, etches the interface between whisker and alloy cap as shown in Figure 1.29. [49] Tips of radii approximately 50 nm were produced. An oxidation/etch procedure can also produce sharpening of the tips for emission applications. [50]

1.5.5 VLS Whisker Crystallography

VLS whiskers grown on a (111) substrate have been shown to grow in the [111] direction. [43] A periodically phosphorous doped silicon whisker clearly shows planar [111] growth as steps with alternating phosphorous doping (Figure 1.30). Figure 1.31 shows a whisker that has grown in the [110] direction. The phosphorous doping and etch procedure showed that the [110] whisker grew by Si atom deposition via the liquid eutectic on two {111} plane variants. Lastly, whiskers can branch during growth corresponding to transfer of growth to another (111) plane; Figure 1.32.

1.6 The Etching of Silicon Wafer by Molecular Species

1.6.1 High Temperature Etching of Si Wafer by F_2

Aliev and co-workers studied the adsorption of F_2 on Si (100) wafer as a function of temperature. [51] Using an automatic ellipsometer operating at a wavelength of 633 nm Aliev et al. investigated adsorption in the temperature range 214 – 873 K. At $T > 530$ K the adsorption layer consists of SiF, SiF_2, and SiF_3. [51, 52] Below $T = 650$ K, the

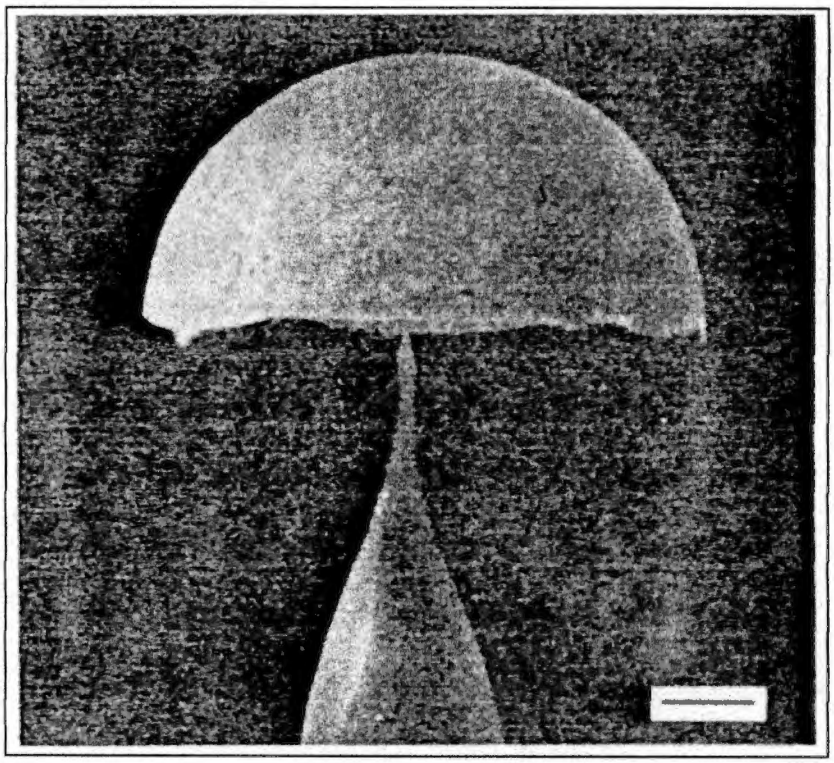

Figure 1.29 Sharpening of a Au-Si whisker using the etch, $HF:HNO_3:H_2O$, in the ratio 1:40:1. The marker is 1 μm. [49]

Source :

[49] E. I. Givargizov, A. N. Kiselev, L. N. Oblenskaya, and A. N. Stepanova, *Appl. Sur. Sci.* **67**, 73 (1993)

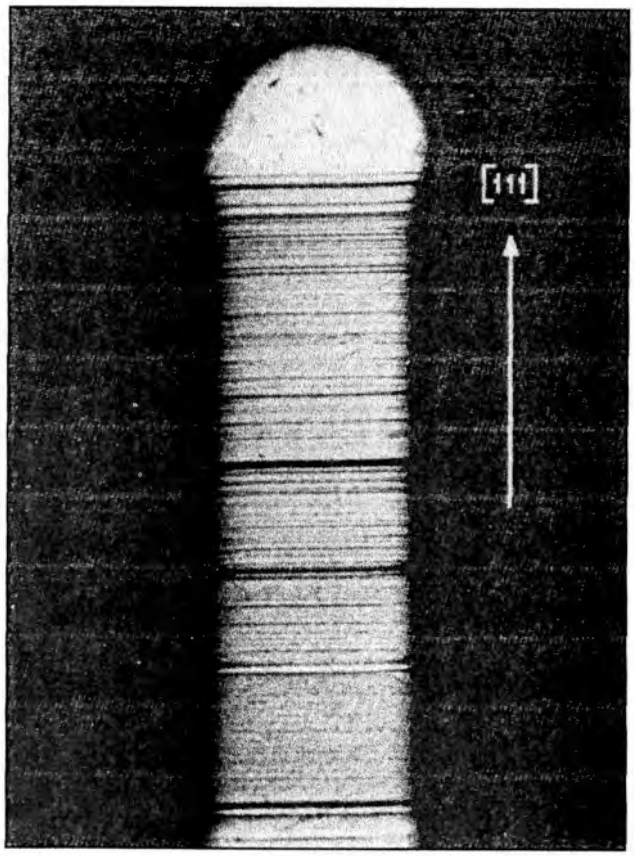

Figure 1.30 A VLS whisker grown in the [111] direction which was periodically doped during growth with phosphorous. The doping shows that crystal growth occurs explicitly via the (111) surface plane. The approximate magnification is 100x and the whisker growth was performed under isothermal conditions. The whisker was etched to reveal the planar doping. [43]

Source :

[43] R. S. Wagner, "VLS Mechanism of Crystal Growth" p. 47 - 119 in Whisker Technology (A. P. Levitt, ed.) Wiley - Interscience, New York, 1970

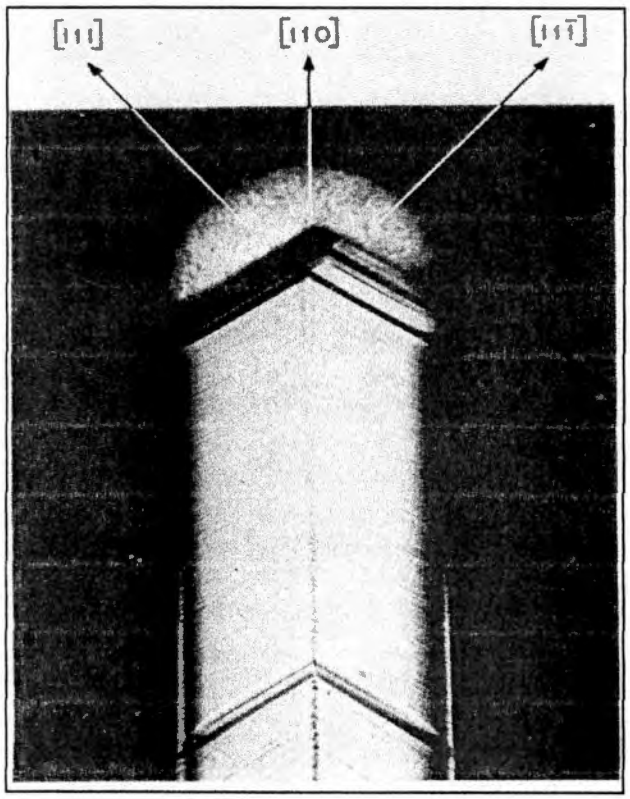

Figure 1.31 A VLS Si whisker that has grown in the [110] direction. The above whisker grew in the [110] direction yet on the atomic scale atoms bonded on two {111} planes to lift the Au-Si drop above the original substrate surface. The same etch and dope procedure as in Figure 1.30. The magnification is ~ 200x. [43]

Source :

[43] R. S. Wagner, "VLS Mechanism of Crystal Growth" p. 47 - 119 in Whisker Technology (A. P. Levitt, ed.) Wiley - Interscience, New York, 1970

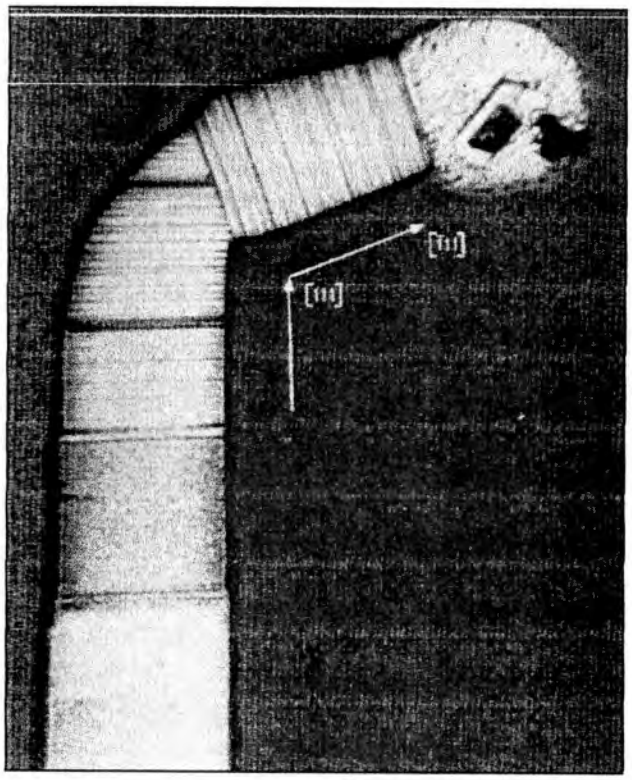

Figure 1.32 A Si whisker grown by the VLS method in a temperature gradient. During growth of the above silicon whisker the temperature on the right side of the whisker was raised above that of the left. The growth followed the change in temperature yet maintained growth on a {111} plane. The growth direction changed from the [111] to [-111]. Magnification approximately 100x. The dope and etch procedure used here is the same as in Figure 1.30. [43]

Source :

[43] R. S. Wagner, "VLS Mechanism of Crystal Growth" p. 47 - 119 in Whisker Technology (A. P. Levitt, ed.) Wiley - Interscience, New York, 1970

adsorption layer was found to remain on the substrate after the F_2 flow was turned off and the vacuum deposition chamber was evacuated. [51]

No adsorption layer formed on the Si surface at T ~ 873 K due to etching. In fact, Aliev et al. found the rate of etching to be so high that substantial changes in surface roughness occurred during experimentation. The surface roughness decreased from that which existed after chemical-mechanical polishing and etching to prepare the Si surface for adsorption. [51]

1.6.2 The Laser Induced Etching of Si by SF_6

Silicon is inert in the presence of SF_6 gas at room temperature. SF_6 can be made reactive with Si through multiphoton absorption of CO_2-laser irradiation [8]

$$SF_6(g) + nh\nu \rightarrow SF_6^*(g).$$

The vibrationally excited SF_6^* chemisorbs on the Si surface and dissociates as [8]

$$SF_6^*(g) \rightarrow 2F^- + SF_4(\uparrow).$$

The F^- ions have small atomic radii ~ 0.64 Å allowing them to penetrate into Si, through the Si interstitial positions, forming a fluorosilyl layer. [8, 53 – 56]

The fluorosilyl layer, 10 – 30 Å thick, consists mostly of the molecular species SiF_3. [6, 53 – 56] Spontaneous etching results from this layer at temperatures as low as 300 K. Gaseous species that emerge from the Si surface are SiF_2, SiF_4, Si_2F_6, and Si_3F_8. [8, 53 – 56] The dominant volatile product depends on temperature. At T = 800 K, SiF_2 is the major etch product.

1.6.3 The High Temperature Etching of Si by an O_2 Molecular Beam

Ohkubo et al. investigated the surface reaction of a pulsed O_2 molecular beam with Si (100) and Si (111) for a range of temperatures. [57] At temperatures above 1 000 K, O_2 was found to etch the Si (100) surface. Desorption studies were carried out with a quadrupole mass spectrometer to determine the volatile species. Gaseous SiO was detected by the mass spectrometer above 1 000 K. [57]

Molecular beam relaxation spectra of the gaseous SiO produced from the molecular beam – Si surface reaction yielded information concerning the reaction path for formation of SiO(g). [57] Ohkubo and co-workers found the formation of SiO(g) to be a multi-step process. The O_2 chemisorbs at ledges on the Si (100) surface, an intermediate oxide forms briefly, and volatile SiO forms and desorbs.

Figure 1.33 shows a SEM photomicrograph of Si (100) etched by an O_2 molecular beam at 1 173 K. [57] The etch pits had facets of {111} and {113} variants. Similar ethcing experiments on Si (111) wafer produced the same SiO(g) yield, at constant temperature, as was produced during the etching of Si (100) wafer. However, etch pits were not observed on the Si (111) surface. [57]

Nakamura et al. used a multiphoton ionization mass spectrometer to determine the gaseous species produced when Si (111) was heated to a temperature of 1 150 ± 150 K in a low pressure ambient, $10^{-6} - 10^{-4}$ Pa, of O_2(g). [58] Following 30 minutes of O_2(g) exposure to high temperature Si (111), multiphoton ionization mass spectrometry signals were received characteristic of the species O_2^+, $^{28}SiO^+$, $^{29}SiO^+$, and $^{30}SiO^+$. The surface reaction [58]

$$O_2(g) + 2Si(s) \rightarrow 2SiO(g)$$

was responsible for the production of SiO(g) isotopes.

Nakamura et al. found the Si^+ signal intensity to increase nonlinearly as a function of O_2 gas leak pressure in the chamber. The SiO^+ signal increased nonlinearly with increasing O_2(g) leak pressure in a similar fashion as the Si^+ signal. They attributed the Si^+ signal to the photodissociation of SiO, by [58]

$$SiO\ [X(^1\Sigma^+)] + h\nu \rightarrow Si(^3P) + O(^3P)$$

which requires a dissociation energy of 8.1 eV. The reaction required two photon absorption because the mulitphoton ionization was performed with a Nd:YAG laser operating at 266 nm (4.66 eV) output.

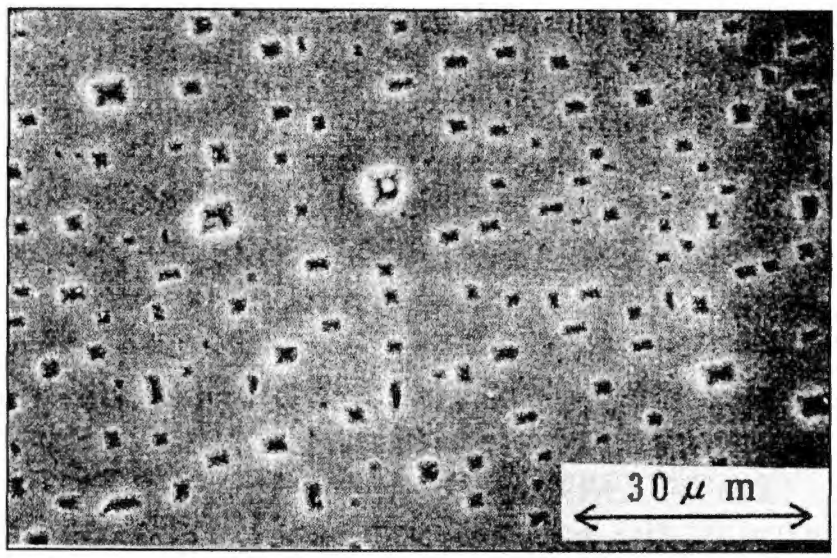

Figure 1.33 Si (100) wafer etched by a pulsed O_2 molecular beam at 1 123 K. The facets of the pits are of {111} and {113} orientations. [57]

Source :
[57] K. Ohkubo, Y. Igari, S. Tomoda, and I. Kusunoki, *Sur. Sci.* **260**, 44 -1992

Chapter 2

Experimental Procedure

2.1 Sample Preparation Procedure

Test grade silicon wafers of (100) and (111) orientations were used in the ablation/etching experiments. Both the (100) and (111) wafers were four inches in diameter, n-type, phosphorous doped, and were purchased from Transition Technology International (TTI). The specified thickness range of the wafers was 475 – 525 μm. The resistivity range for the (100) and (111) wafers were 1.0 – 6.2 Ω cm and 1 – 100 Ω cm, respectively.

The wafers were cut to sizes of ~ 1 x 2 cm^2 prior to introduction into the irradiation chamber. The wafers were scribed on their unpolished surface using a sharp edged diamond tool. Each scribe was made along a <100> direction. A light load was then applied to the unpolished face to cleave the wafer along the scribe. This procedure ensured a sharp, cleaved wafer edge. The native oxide present on each polished wafer was not removed prior to laser surface treatment.

2.2 Laser Irradiation Procedure

A Lambda Physik LPX – 305i excimer laser producing KrF (248 nm) wavelength radiation was used to irradiate the single-crystal Si (100) and (111) wafers.
All laser treatments of Si were carried out at normal laser incidence unless otherwise stated. The experimental set-up is shown in Figure 2.1. Two photographs of the

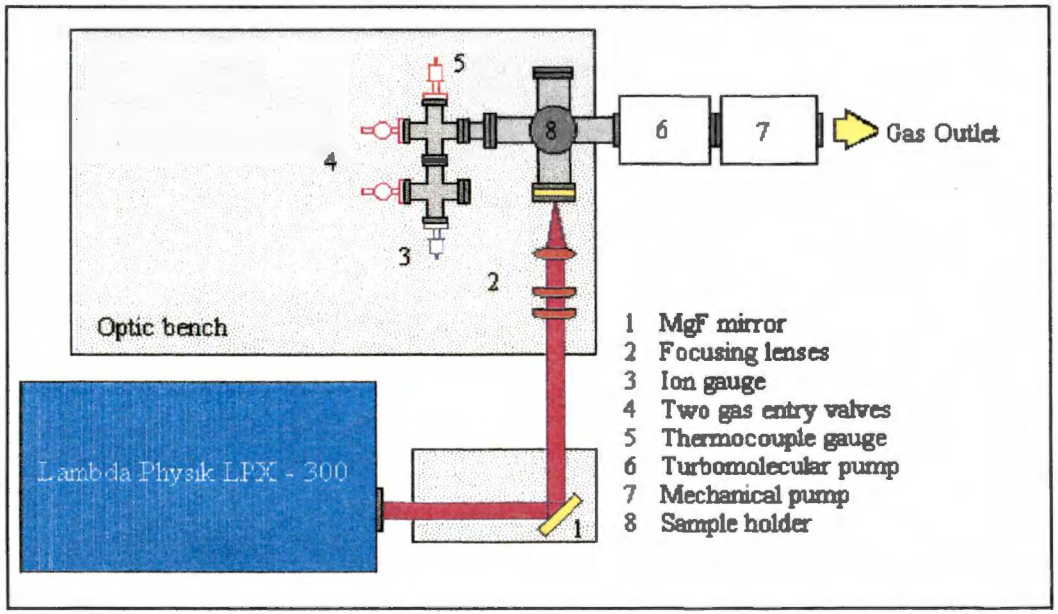

Figure 2.1 A view looking down on the laser laboratory. Both the thermocouple and ion gauge pressure measuring devices are products of Varian. The mechanical pump is a Pascal series Alcatel and the turbomolecular pump is also a Alcatel product. The vacuum chamber was sealed at the flanges by Viton o-rings and the stainless steel conponents forming the chamber were made by Nor-Cal.

irradiation chamber are shown in Figure 2.2. The laser beam emerging from the laser cavity was directed to an optic bench using a MgF_2 coated, fused silica mirror.

The optic bench contained an aperture, a fused-silica lens array, and the irradiation chamber. The aperture, ~ 1 x 2 cm^2, removed the low energy tails of the trapezoidal laser beam energy profile. The laser fluence was varied by adjusting the position of the fused-silica lens array with respect to the sample holder in the irradiation chamber. The laser energy was held fixed among all the experiments performed. Three fused-silica lenses were used to form the beam-focusing array.

Two cylindrical lenses first focused the laser beam. The curved faces of the two lenses were oriented at 90° with respect to one another in order to focus both dimensions of the rectangular laser beam. A bi-convex, spherical lens then provided addition focus to achieve a spot size of ~ 0.2 x 0.7 cm^2.

The focused laser beam entered the chamber via a 2" fused-silica window. The energy of the beam entering the chamber was measured with a Scientech Astral AD30 volume absorber calorimeter. The calorimeter was placed in front of the window to measure the energy and was removed prior to laser treatment. The energy density value striking the target was determined by measuring the laser spot mark produced on the target after irradiation and dividing this number into the energy that was obtained using the volume absorbed calorimeter. Thus, the energy density values reported in this work are average values because the energy profile of the laser beam was not completely homogeneous, even after passing through the aperture.

A wide-range of irradiation conditions were investigated to determine their effects on Si wafer surface morphology. The laser fluence range investigated was from 1 – 4 J/cm^2.

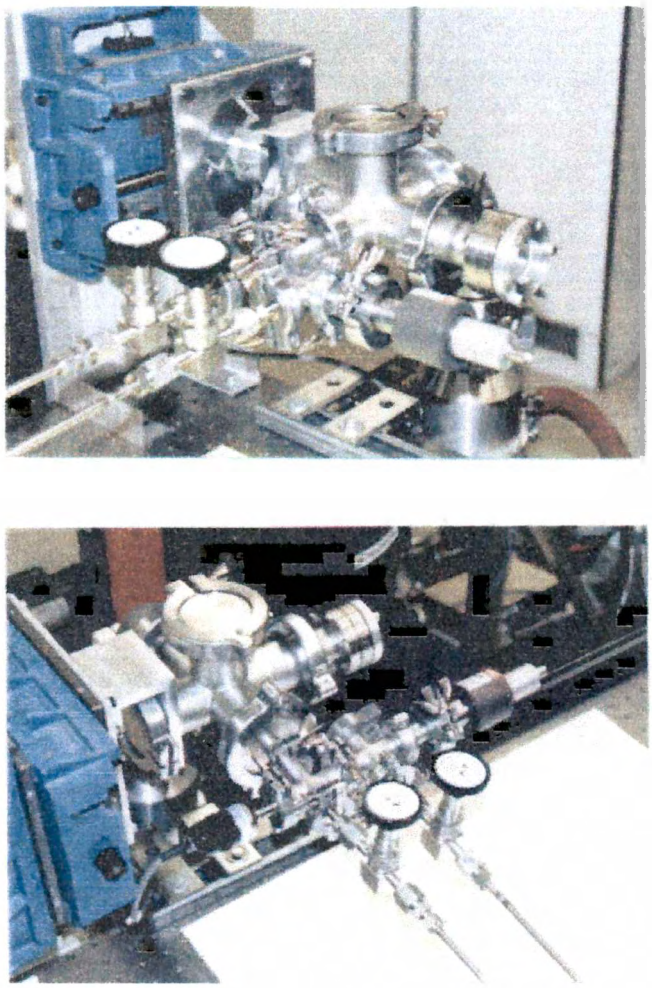

Figure 2.2 Two color photographs of the equipment attached to the vacuum chamber. a) A photograph of the front of the vacuum chamber showing the ion gauge and fused-silica, beam entrance window. b) A side-view of the chamber showing the dual valves for gas introduction (the mass flow controllers were connected in series with these valves during experiments although not shown in this photo) and the thermocouple pressure measurement gauge.

Pulse repetition rates of 1 to 10 Hz were used. The number of laser pulses spanned five orders of magnitude from 1 to 10 000 pulses.

The laser treatments were carried out in a number of background gases including air, Ar, 5% H_2 – Ar, N_2, 5% O_2 – N_2, 20% O_2 - Ar, He, and SF_6. The gases were pure to two decimal places 99.95%. Two different sample holders were used during the experiments depending on the background gas present during irradiation. Samples irradiated in air were not placed in the chamber. Instead, the irradiation was performed in the open atmosphere of the laboratory. The samples were held vertically, at normal incidence to the beam, by way of a perforated stainless steel plate. The plate was connected in series with a mechanical pump. The pump pulled vacuum through the perforations effectively holding the sample in place. Samples irradiated in the other gases listed above were done in the irradiation chamber shown in Figure 2.2.

Tylan brand mass flow controllers regulated the flow of gas into the chamber. The pressure in the chamber was measured using a Varian thermocouple gauge at high pressure (10 – $1x10^{-3}$ Torr) and a Varian ionizing gauge at low pressure ($1x10^{-3}$ – $1x10^{-8}$ Torr). Both pressure gauges were operated from a digital console that also displayed real time pressure measurements. A Pascal series mechanical pump and an Alcatel turbomolecular pump were used to lower the pressure in the o-ring sealed, vacuum chamber. Prior to each experiment the chamber was pumped to a base pressure of $6x10^{-7}$ Torr to remove any gaseous impurities present in the chamber.

2.3 Post-Irradiation Morphology and Microstructure Characterization Techniques

2.3.1 Scanning Electron Microscopy

Following laser processing, the ablated/etched Si wafers were analyzed in a JEOL JSM – 840 scanning electron microscope (SEM). The microscope utilizes secondary electron emission from a sample irradiated with 0 – 20 keV electrons to produce high magnification viewing of the irradiated wafer surface. The electron emission filament was operated at 290 μA and a high voltage of 10 kV. The smallest working distance possible (15 mm) was used during electron microscopy to maximize the resolution of the sample image. Si samples were viewed at angles ranging from 0° to 45° in the microscope.

2.3.2 Scanning Profilometry

A Dektak II scanning profilometer was used to quantitatively characterize the surface topography. The profilometer uses a 5 μm diameter tip to scan the surface of a sample. A vertical resolution of 100 Å is achieved using an induction coil arrangement to detect small displacements of a vertical rod connected to the scanning tip. The horizontal resolution of the instrument is ~ the scanning tip diameter.

2.3.3 Auger Electron Spectroscopy

To determine the surface composition of the irradiated sample, to a shallow depth of ~ 400 nm, Auger electron spectroscopy (AES), coupled with ion sputtering, was used. An electron of sufficient energy can strike an atom of the bulk material such that an orbital

electron is ejected. An outer shell electron will fall into this vacant shell and simultaneously an Auger electron, or x-ray, is ejected. [59] The Auger electron ejected has a characteristic energy that depends on the excited electronic shell, the electronic level of the excited Auger electron, and the nature and chemical environment of the atom in question.

Auger electrons ejected from atoms located over a few monolayers from the material's surface are absorbed. To determine composition changes with depth into the bulk material requires periodically alternating AES and ion sputtering. Ar^+ ions were used to sputter the modified silicon target. AES followed the Ar^+ sputtering to determine the chemical composition of the Si surface.

2.3.4 X-ray Diffraction

X-ray wavelengths are on the order of the interatomic spacings in inorganic materials. Impinging x-rays will scatter on interaction with the electrons, orbiting the periodically spaced atoms, just below the material's surface. The similarity in x-ray wavelength and interatomic spacing will produce interference patterns in the scattered x-rays. Thus, a diffraction pattern is produced when a monochromatic beam of x-rays strikes the surface of a single-crystal or polycrystalline material.

Information is imbedded in x-ray diffraction patterns concerning the chemical and physical arrangement of a material's atomic structure. Diffraction patterns yield specific information about materials such as the degree of crystallinity, the chemical composition, the atomic lattice parameters, and the crystal plane spacings. A Rigaku x-ray

diffractometer was utilized in this work to determine the crystallinity of the Si wafer surface following laser irradiation.

Chapter 3

Results

3.1 Si Microcolumns Grown in Air

3.1.1 Si Microcolumn Evolution and Growth (0 – 1 200 pulses)

Pulsed KrF laser irradiation in 1 atm air produced the silicon morphology shown in Figure 3.1. The surface of the silicon wafer was oriented normal to the laser beam. The cone morphology grew normal to the wafer surface in response to the irradiation. Experiments were conducted to determine if the microcolumns grow in a fixed crystallographic direction or in the direction of the incident radiation. Varying the angle of incidence of the laser pulse from normal to the silicon wafer, as shown in Figure 3.1, to 25° off the surface wafer normal demonstrated that the columns always grow in the incident pulse direction.

The microcolumns grow in length as the number of incident pulses increases. However, a certain number of pulses are required before Si microcolumn development ensues. In Figure 3.2, 250 pulses at 3.0 J/cm^2 have produced topographical changes but no columns have yet evolved. Fractures are present in the sample, which coincide with the {100} planes normal to the (100) surface. Additionally, features associated with melting are seen on the surface, namely ripples and surface ridges. The arrows in Figure 3.2 point to both features. Circular pits are also present in the 250 pulsed sample with initial diameters of ~ 2 – 3 μm. Further irradiation sees these holes expand diametrically with their depth increasing. Pulsed laser irradiation of a Si (111) wafer, shown in Figure 3.3, produced the same morphology as found in (100) wafer.

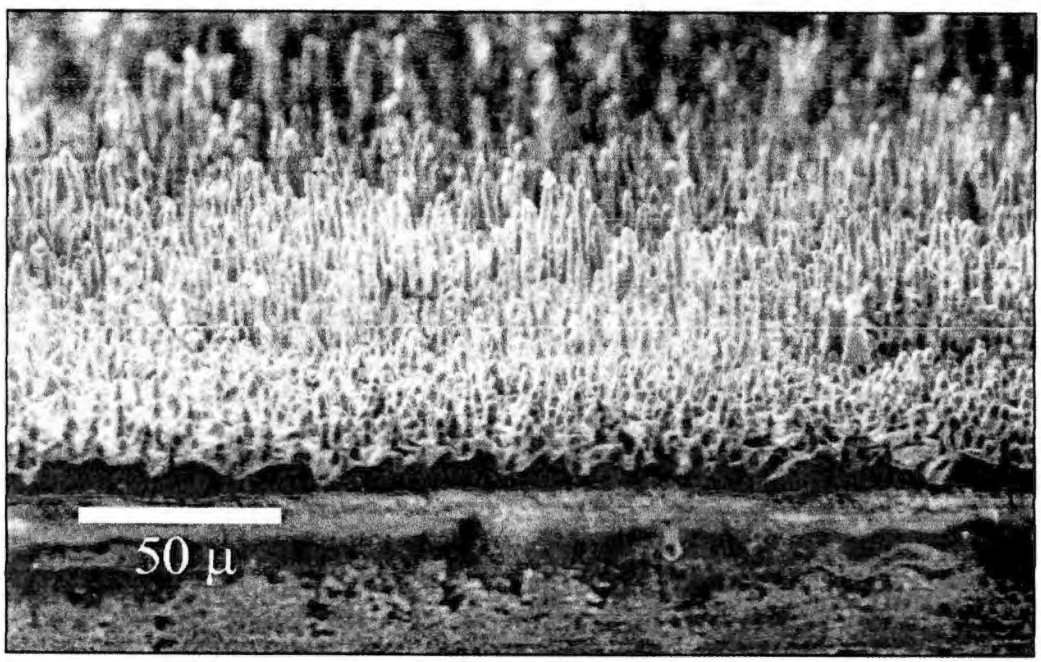

Figure 3.1 The Si microcolumn forest produced in air using 2 000 laser pulses of energy density 3.0 J/cm^2. The wafer is tilted 80° off the wafer surface normal. A pulse repetition rate of 3 Hz was used for irradiation.

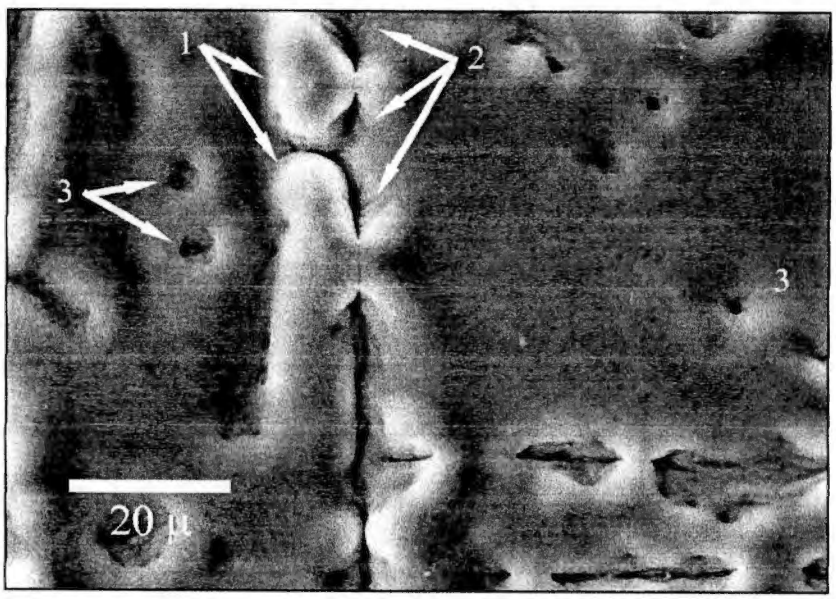

Figure 3.2 The beginning stages of Si microcolumn formation. 1) Surface ridges, 2) ripples, and 3) pits are morphology characteristics of the wafer surface after 250 laser pulses. The wafer has fractured along the surface exposed {100} planes. E_d = 3.0 J/cm^2, pulse repetition rate (PRR) = 2 Hz, background gas (BG) = air, 1 atm.

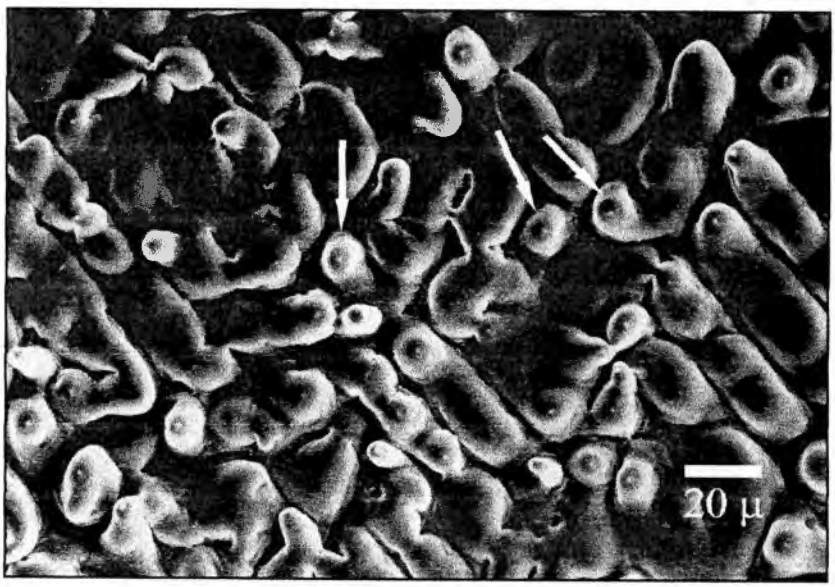

Figure 3.3 Pulsed laser irradiation of Si (111) wafer produces the same surface features present on Si (100) wafer for low numbers of pulses. E_d = 3.0 J/cm^2, PRR = 1 Hz, and the number of laser pulses (NOP) = 200. The surface ridges (arrows in the figure) will evolve into microcolumns when additional laser pulses are provided to the wafer; ~ 200 more. BG = air, 1 atm.

After 500 laser pulses, Figure 3.4 shows that the surface ridges present in Figure 3.2 have now begun to rise above the wafer floor. A profilometry scan on a 600 laser pulsed sample, Figure 3.5, indicated that the ridges rise not only above the wafer floor *but that they also protrude above the initial wafer surface.* Several microcolumns in Figure 3.5 protrude 10 μm above the initial wafer surface! A full range of profilometry scans for different numbers of pulses in air is shown in Figure 3.6.

The fractures present along the wafer surface have begun to widen after 500 pulses as shown in Figure 3.4. In addition, the optical micrograph shown in Figure 3.7, taken following 500 pulses, exhibits clearly that the surface ridges occur most often in close proximity to the surface fractures. Several etch pits are also resolvable in the optical photo.

A change in surface morphology was observed across the laser-irradiated areas. For instance, the surface topography midway between the irradiated spot center and the spot edge (Figure 3.8) is slightly different from that shown in Figure 3.3. The latter figure corresponds to a region close to the center of the laser spot.

The topography shown in Figure 3.8 is devoid of the surface fractures seen previously in the micrograph in Figure 3.3. The surface ridges generated away from the laser spot center evolved in a random pattern. In contrast, surface ridges located in the center of the laser spot evolved exclusively adjacent to surface fractures. These morphological variations are related to the non-uniform melting of the Si wafer surface (section 4.2.2). It will be shown in section 3.1.4 that the microcolumn morphology depends upon laser fluence.

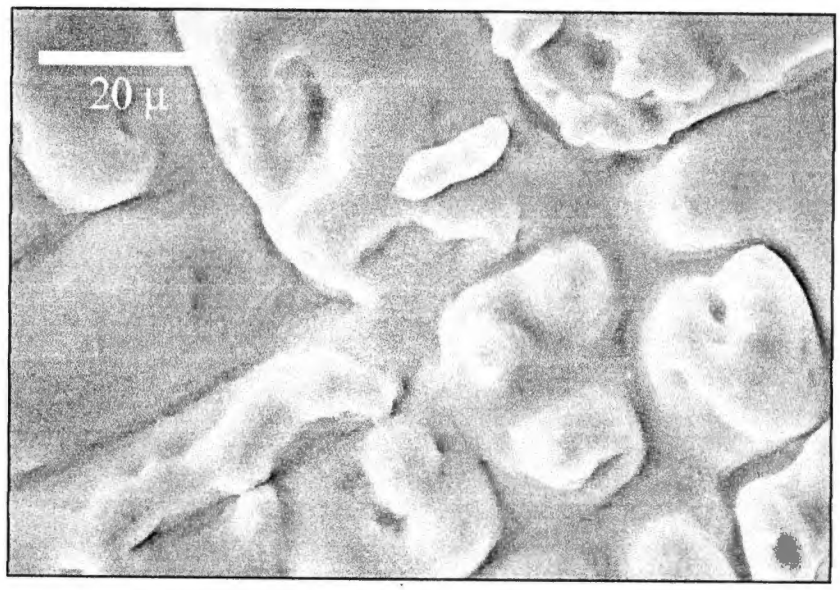

Figure 3.4 The surface fractures that form at low numbers of laser pulses on the Si wafer surface widen as additional laser pulses are applied to the wafer. The surface fractures above have widened after 250 additional pulses compared with the fractures shown in Figures 3.2 and 3.3. In addition, the surface ridges have begun to rise above the wafer floor. Each ridge marks the site of a future microcolumn. E_d = 3.0 J/cm^2, NOP = 500, BG = air, 1 atm, and PRR = 2 Hz.

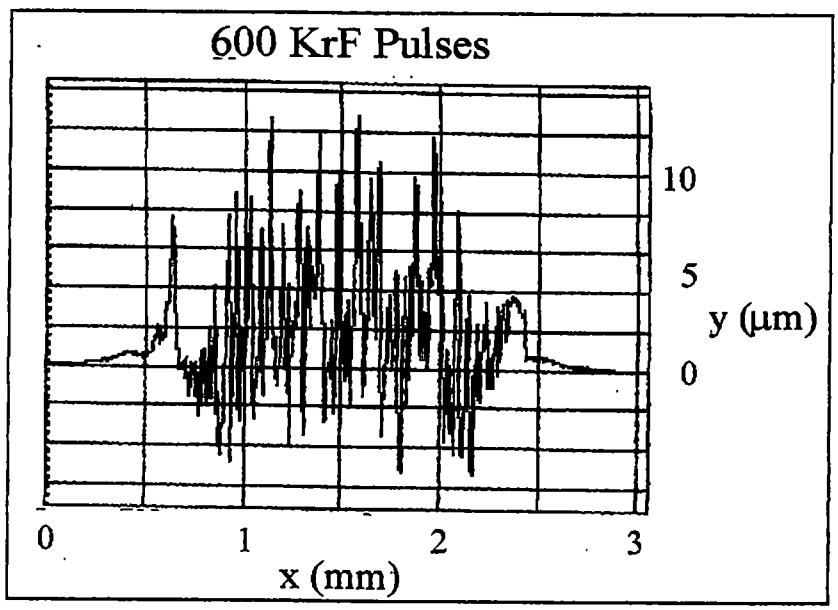

Figure 3.5 Si microcolumns evolved after 600 KrF laser pulses in air, which protrude above the initial Si wafer surface. The peaks at ~ 0.65 mm and ~ 2.4 mm correspond to material that lies outside the laser spot. This material originated in the target, was etched by the laser pulse, and redeposited around the perimeter of the laser spot. This material charges when exposed to a collimated electron beam.

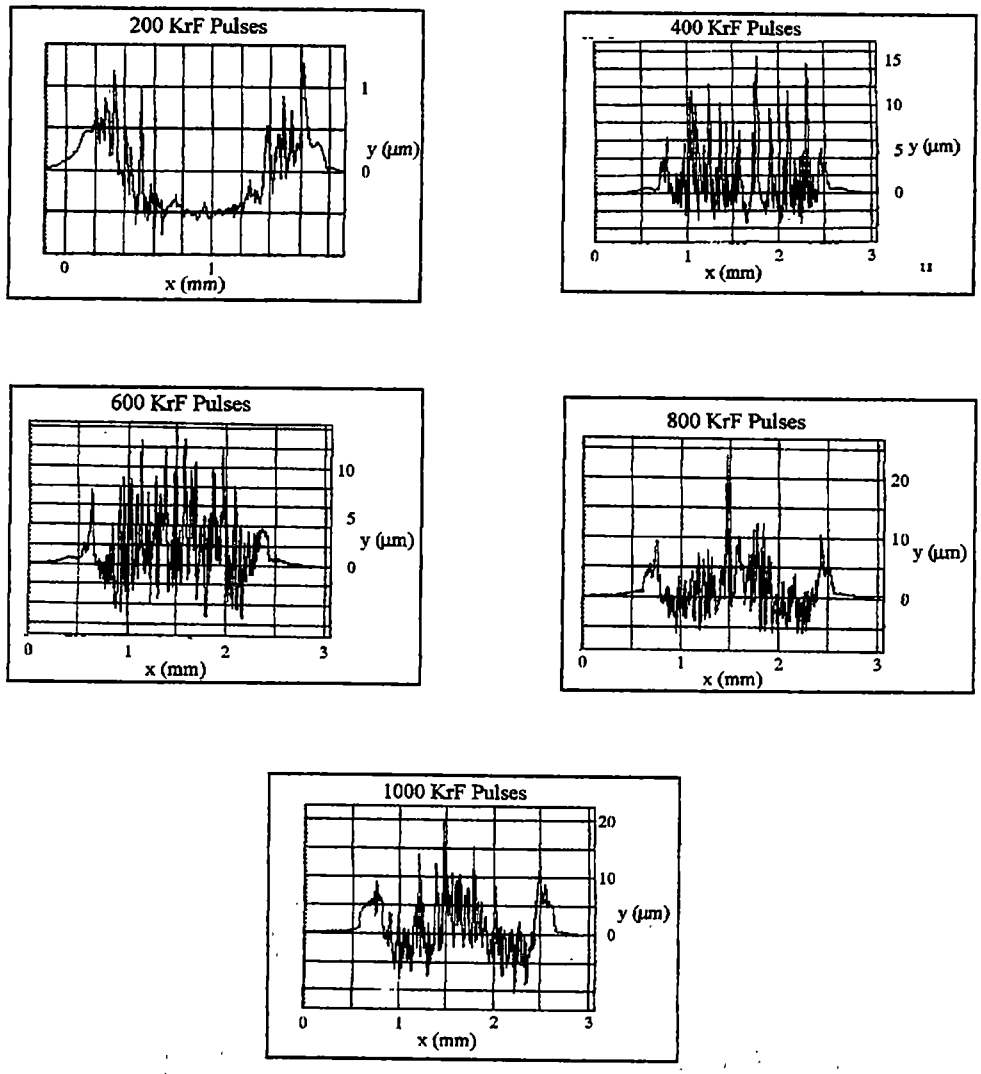

Figure 3.6 Profilometry scans taken across the short dimension of a rectangular laser spot on Si wafer at various numbers of shots. At numbers of pulses > 200, Si microcolumns form that, in some cases, protrude above the initial wafer surface by 20 μm. E_d = 3.0 J/cm^2, PRR = 3 Hz, and BG = air, 1 atm.

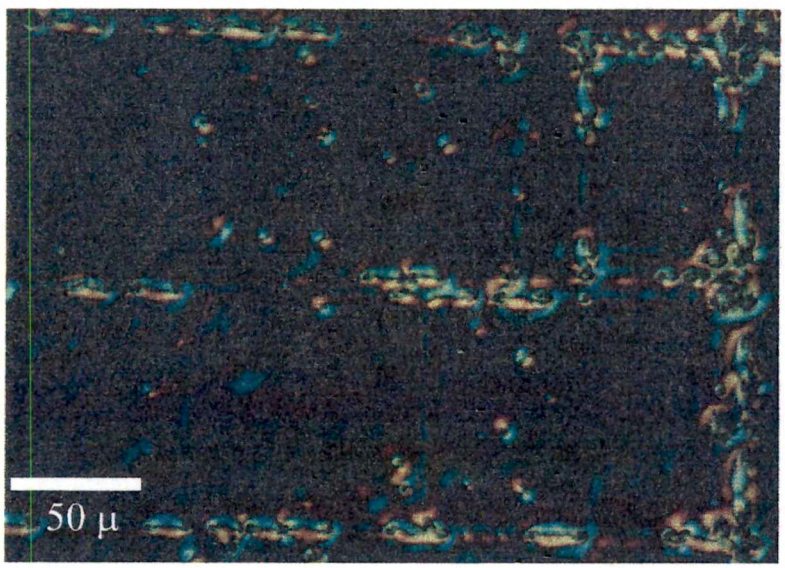

Figure 3.7 Optical micrograph showing the various surface features resulting from 500 laser pulses. The surface instabilities are yellow – green and are located adjacent to the {100} fractures. The pitting appears randomly in the the non-fractured regions; also yellow - green. E_d = 2.8 J/cm^2, PRR = 1 Hz, and BG = air, 1 atm.

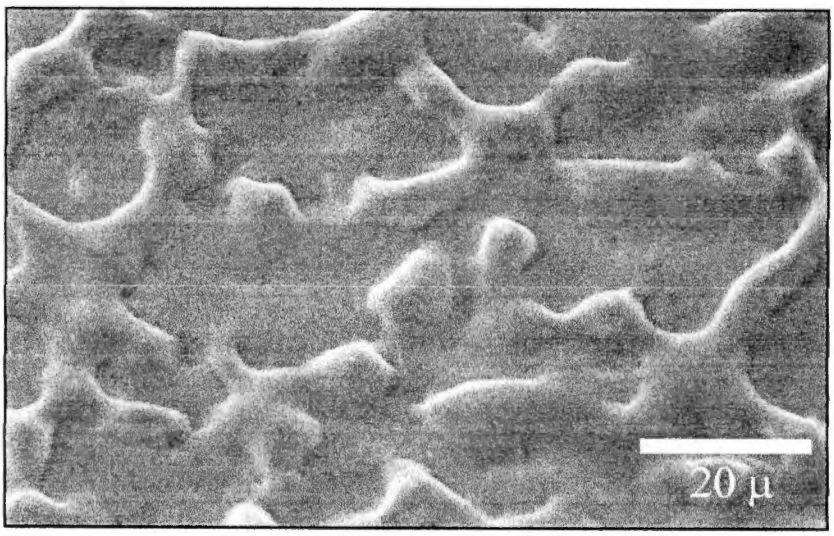

Figure 3.8 Surface ridges form as a result of non-uniform heating of the surface during pulsed excimer laser irradiation of Si (100) wafer. This micrograph was taken midway between the laser spot edge and center. The same surface ridges are present as were shown in Figure 3.3 yet the crystallography oriented fractures are not present. $E_d = 2.9$ J/cm^2, NOP = 400, PRR = 1 Hz, and BG = air, 1 atm.

Figure 3.8 shows surface ridges characteristic of a melted topography. The initiation of surface ridges appears to be related to surface tension effects induced from the laser assisted melting process. For example, the topography shown in Figure 3.8 is analogous in surface morphology to the start of breaking up into small droplets of any thin metallic film, ~ 10 – 30 Å thick, on substantial surface heating.

The fully developed microcolumn density was found to decrease continuously starting at the laser spot center outward to the spot edge. The term fully developed refers to microcolumns that have saturated in height, i.e., extra laser pulses over the saturation value will produce no additional column growth. Section 3.1.3 contains quantitative data concerning the microcolumn density variation with position inside the laser spot.

Between 400 and 600 laser pulses rapid Si microcolumn growth occurs. Comparison of Figures 3.4 and 3.9 shows the drastic change in surface morphology from 100 additional laser pulses. The highest growth rate of Si microcolumns occurred in this laser pulse range. The average, maximum microcolumn length for the 400 pulse and 600 pulse laser samples were 16 and 30 μm, respectively. The length measurements were made on Si microcolumns located at the centers of the irradiated areas using the SEM. Moreover, in this same laser pulse window, 400 – 600 pulses, the column density experiences its highest growth rate.

Referring to Figure 3.10, the column density increases radically from 4.6×10^5 columns/cm^2 after 400 laser pulses to 1.5×10^6 columns/cm^2 following 600 KrF laser pulses, a column density increase of over 300%. The maximum column density achieved with KrF irradiation in air, ~ 2.2×10^6 columns/cm^2, occurred at 1 200 laser pulses. Figure

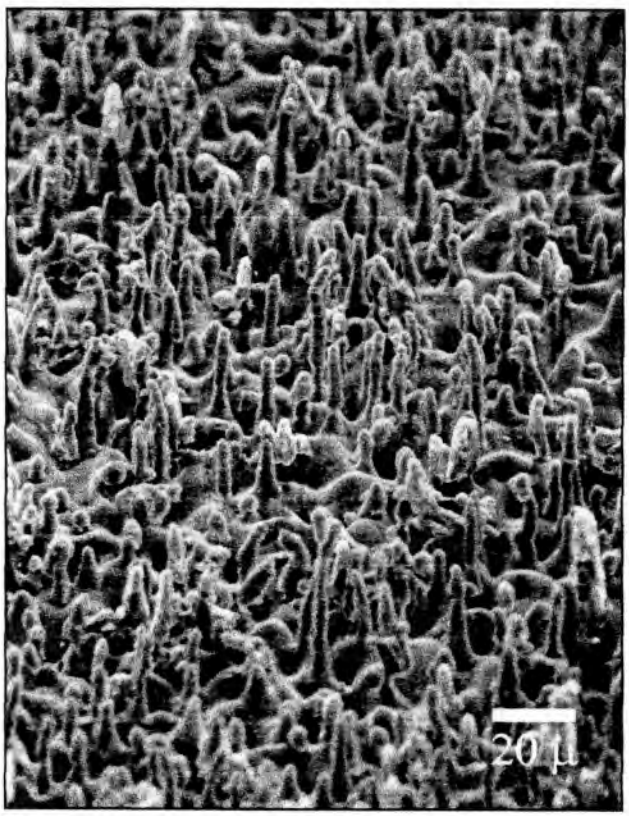

Figure 3.9 Si (100) wafer irradiated with 600 laser pulses. Comparison of this micrograph with Figure 3.4 shows that rapid microcolumn growth has ensued following 100 additional laser pulses. $E_d = 3.3$ J/cm^2, PRR = 3 Hz, and BG = air, 1 atm. Wafer oriented 44° off the Si wafer surface normal in the photo.

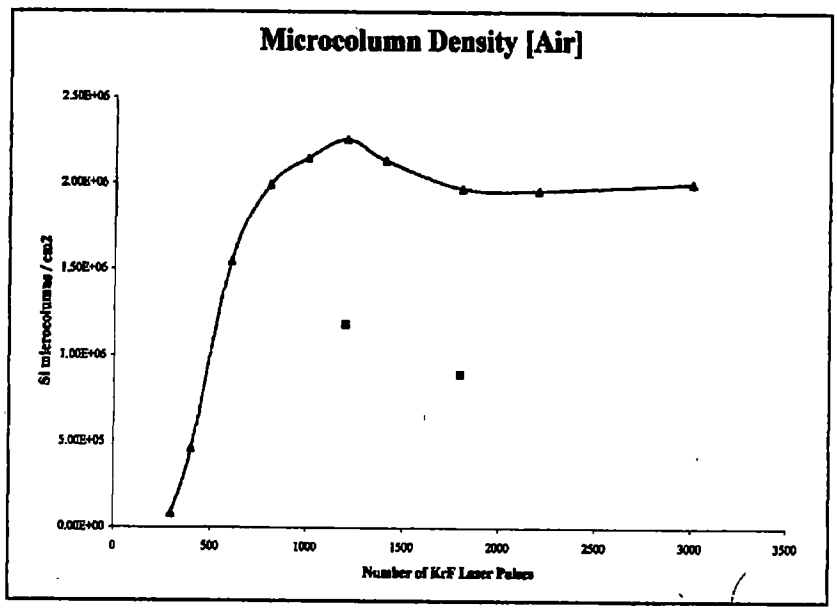

Figure 3.10 The Si microcolumn density plotted as a function of the number of KrF laser pulses in air. The two square data points correspond to irradiation performed in 5% O_2 - N_2. The reduction in oxygen concentration by 3/4 had the affect of reducing the microcolumn density by 1/2. The data points were taken in the center of each sample from one micrograph in an area of 144 μm x 112 μm. E_d = 3.3 J/cm^2, PRR = 4 Hz, and BG = air, 1 atm, and 5% O_2 - N_2, 1 atm (0.10 SCFM)

3.11 shows a high magnification view of the microcolumn density after 1 000 sequential pulses.

Intermixed among the silicon spikes in Figure 3.11 are both cones and columns. Examination of Figure 3.9 shows that mature, i.e., fully-grown, spikes are all columnar. However, 400 additional shots over 600 produce both mature cones and columns. The collimated beam of the SEM causes charging in the material on the cone surfaces whilst columns do not produce charging. SEM micrographs of individual columns were taken to further characterize the morphology.

Inspection of the columns in Figure 3.12 reveals the existence of a spherical, 2 – 3 μm tip terminating each column. Figure 3.13 provides a high magnification view of two Si microcolumns and the spherical tip geometry associated with each. Closer inspection of an individual microcolumn showed that each tip is not a smooth sphere but rather a rough sphere made of concentric rings or steps. Shown in Figure 3.14, each successive concentric step is smaller in diameter than the previous until the tip terminates into a round, spherical tip < 1 μm in diameter.

Surface ridges and 20 μm tall microcolumns coexist in the laser irradiated Si wafer shown in Figure 3.13. The co-existence of these ridges and well-defined microcolumns clearly indicates that the formation of the surface ridges is an inhomogeneous process. For example, surface ridges were present in a wafer that had received 8 000 laser pulses.

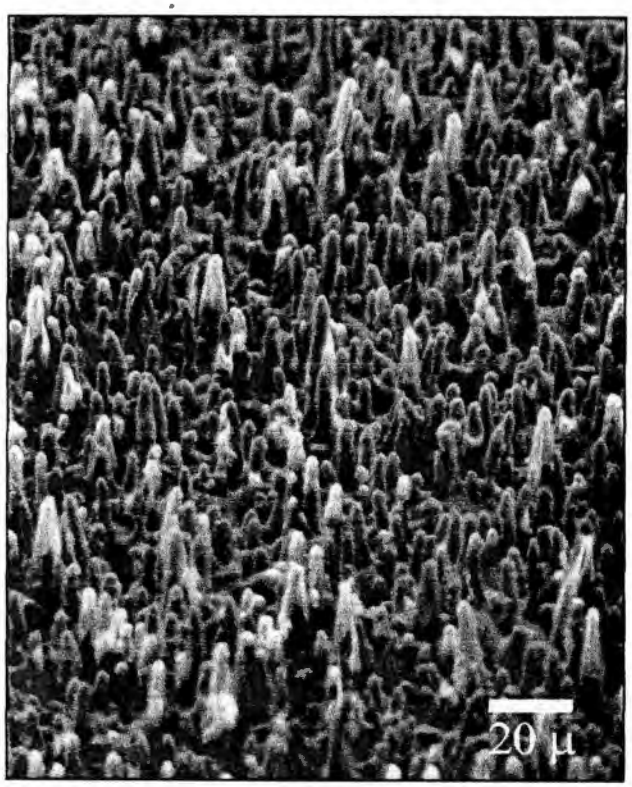

Figure 3.11 Cones and columns are produced on the surface of laser irradiated Si (100) after 1 000 laser pulses. The cones are visibly charging in the above micrograph. The microcolumn density is very close to its maximum value in this figure. E_d = 3.3 J/cm^2, PRR = 3 Hz, and BG = air, 1 atm.

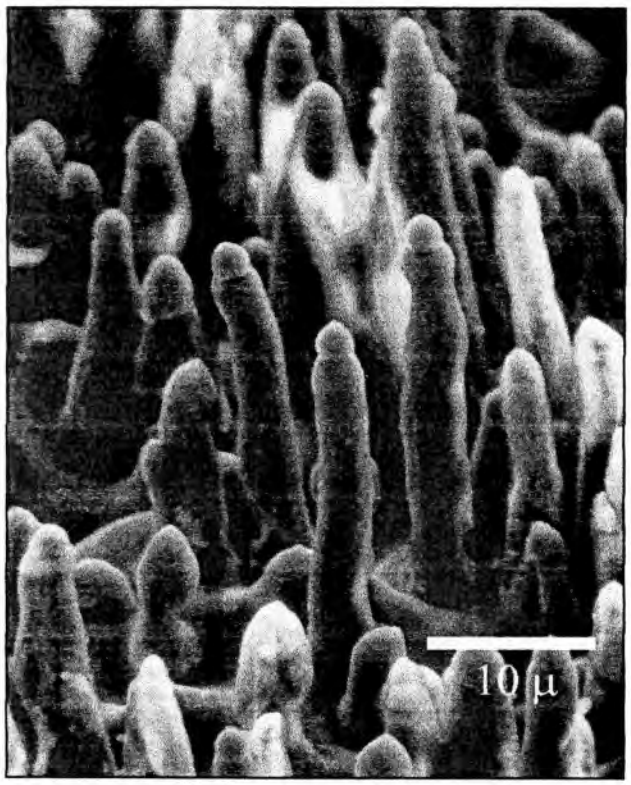

Figure 3.12 Si (100) wafer irradiated with 1 000 KrF pulses. Each of the high aspect ratio Si microcolumns has a 2 - 3 μm spherical tip at the top. In the fore- and background several of the cones are charging. The tall, slender columns retain the conduction properties of the bulk, single-crystal Si wafer. The same wafer as shown in Figure 3.11.

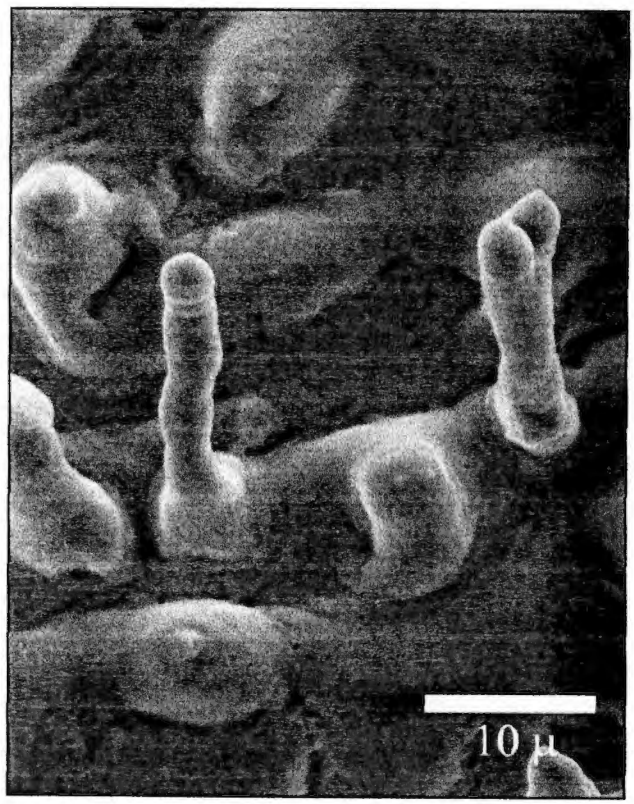

Figure 3.13 The microcolumns formed inhomogeneously throughout the pulse range tested, 1 - 20 000 pulses. Several surface ridges 1 - 5 μm high are shown above. E_d = 3.3 J/cm^2, NOP = 250, BG = air, 1 atm, and PRR = 4 Hz.

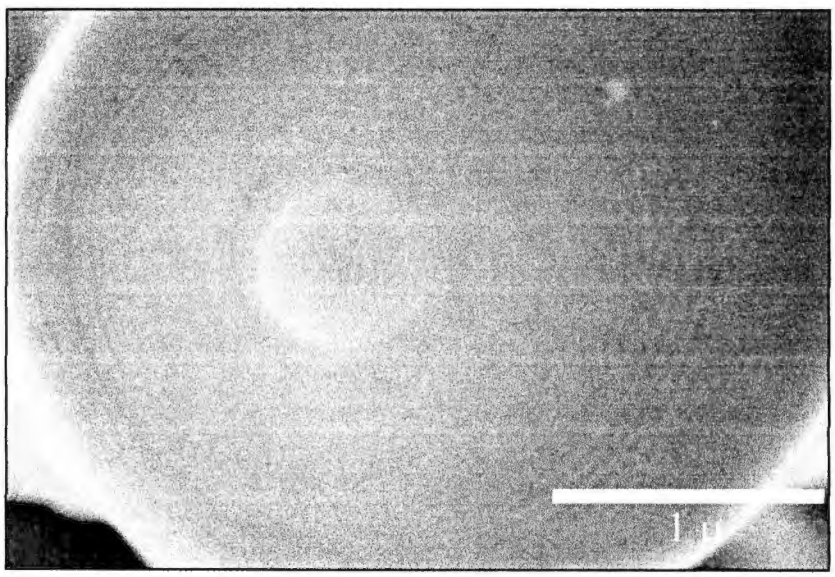

Figure 3.14 A view looking vertically down on the tip of a Si microcone. The tip is made of many nanometer spaced concentric steps which stack together to form the spherical tip. The end termination appears to be a sphere ~ 0.5 μm in diameter. E_d = 1.5 J/cm^2, BG = SF_6, 1 atm (0.20 SCFM), NOP = 2 040, and PRR = 3 Hz.

3.1.2 Si Microcolumn Growth (> 1 200 pulses)

The microcolumn density remains relatively constant between 1 200 and 3 000 laser pulses (Figure 3.10). The Si microcolumns begin to coalesce together following 3 000 laser pulses. The coalescence results in the formation of microcolumn complexes that range in diameter from 10 – 30 μm and contain many microcolumns. These complexes are shown in Figure 3.15. Interestingly, the larger complexes, e.g., complexes of 30 μm base diameters, are conical in shape and have hollow central axes.

Figure 3.16 shows that high numbers of laser pulses, in this case 8 000 pulses, act to substantially decrease the column density. The coalescence process seen after 3 000 laser pulses is not present in this regime. Also apparent in Figure 3.16 is the enlargement of the surface fractures produced at low numbers of pulses. The {100} fractures have widened from nanometer to micrometer sized features after 7 800 pulses. In addition, the same 2 – 3 μm diameter pits were observed. However, after 7 800 pulses the pits had penetrated down into the material forming a funnel. Figure 3.16 illustrates the "funnel-like" penetration. No further changes in morphology were observed up to 20 000 laser pulses.

3.1.3 Redeposition during Si Target Etching

Figure 3.17 shows the macroscopic laser damage induced by sequential laser ablation/etching. Substantial redeposition has occurred around the perimeter of the laser spot. The amount of material outside the spot increases as either the number of laser pulses or the fluence is increased. The cross-section of the material surrounding the laser spot is in the form of a triangle as shown in Figure 3.18. The laser spot side of the

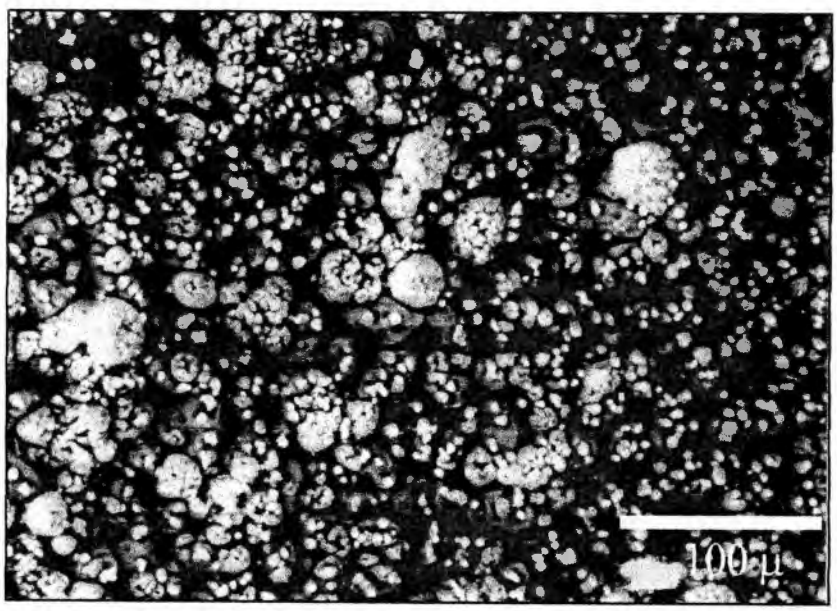

Figure 3.15 In the pulse range; 8 000 > NOP > 3 000, the microcolumns coalesce together to form conical, microcolumn complexes. The larger complexes, 10 - 30 µm in diameter, are hollow down their vertical axis and contain many Si micro-columns. E_d = 3.1 J/cm^2, NOP = 3 000, BG = air, 1 atm, and PRR = 2 Hz

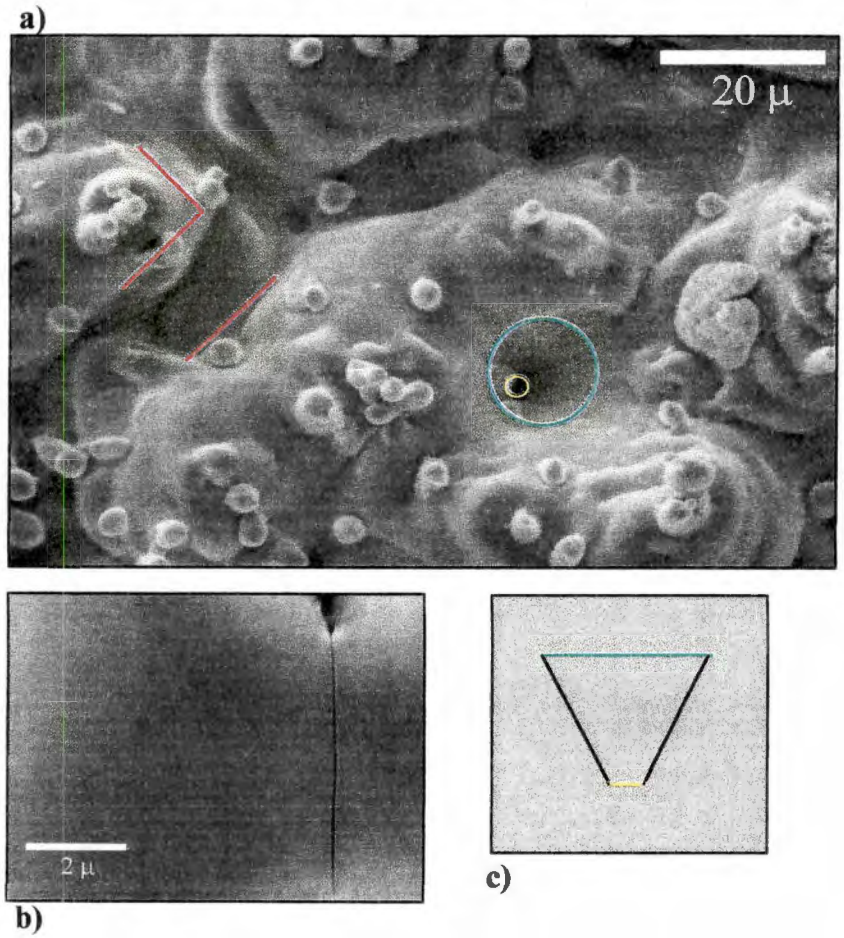

Figure 3.16 Si (100) wafer irradiated with 8 000 laser pulses and an energy density of 2.8 J/cm^2. a) Following 8 000 laser pulses the fracture cavities, initially nanometer wide features, have widened to ~ 10 - 15 μm. E_d = 2.8 J/cm^2, PRR = 2 Hz, and BG = air, 1 atm. b) An initial fracture following 250 pulses, E_d = 3.0 J/cm^2, PRR = 3 Hz. c) Also present in a) are the 2 - 3 μm etch pits. The pits have retained their diameter yet have penetrated into the material in a conical fashion. A top-down view of penetration is shown in a) and c) shows a cross-section.

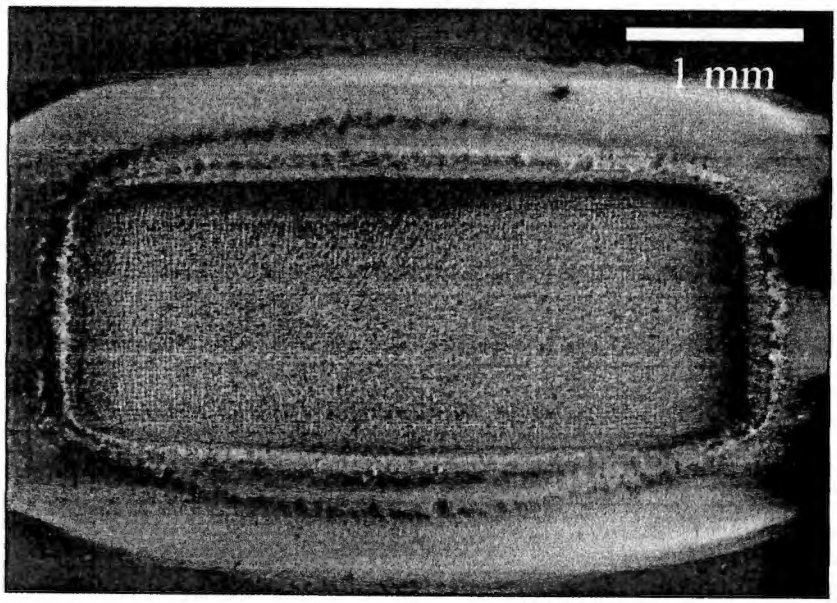

Figure 3.17 The well-defined, rectangular laser spot was formed on the Si wafer surface using 2 000 pulses of fluence 3.6 J/cm^2. The microcolumns appear as dots running in vertical and horizontal directions, i.e., <100> directions. Redeposited material surrounds the spot that charges in response to a focused electron beam. PRR = 5 Hz and BG = air, 1 atm.

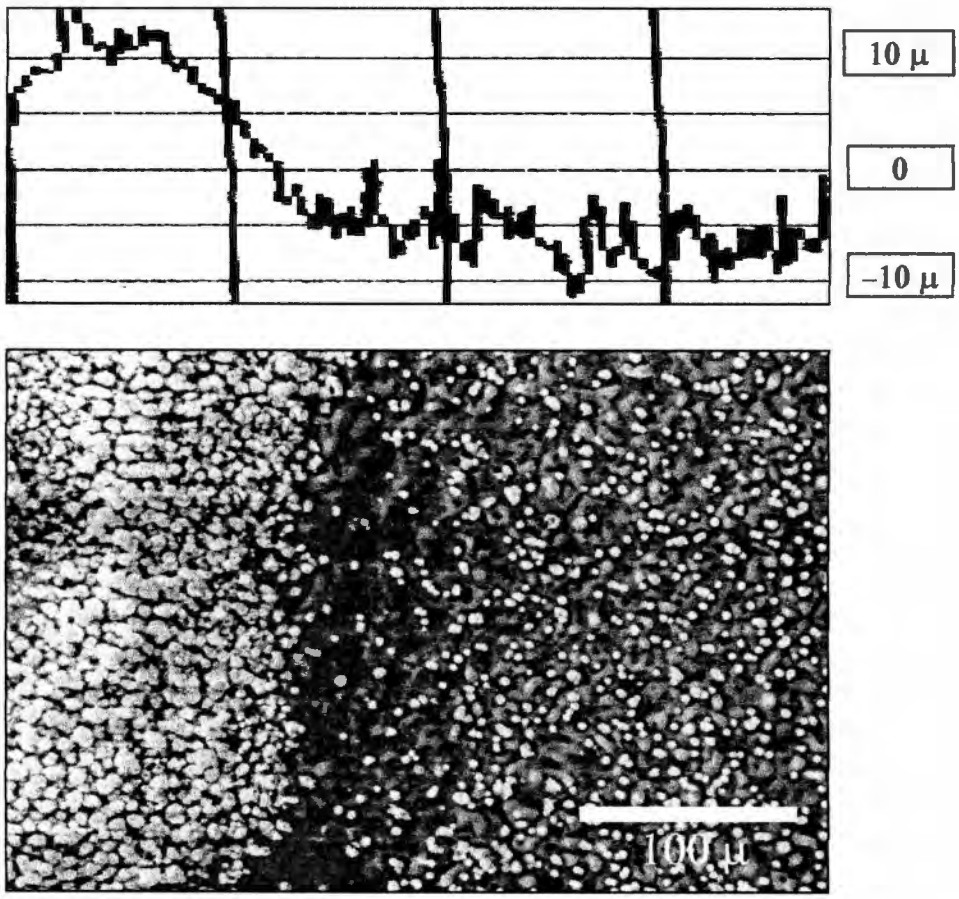

Figure 3.18 A low magnification view of a laser spot edge. The profile scan above the photo corresponds to the vertical topography in the micrograph. The micro-column density falls off right-to-left as a result of the fluence gradient in the laser spot. The sample received 1 000 pulses of energy density 3.1 J/cm^2. The micro-column density has dropped to ~ 1.2x10^6 col/cm^2, 200 μm from the spot edge. At the spot center the density was ~ 2.2x10^6 col/cm^2. The density has dropped by almost half. PRR = 2 Hz and BG = air, 1 atm.

triangle cross-section is made of Si microcolumns that have a density comparable to that found at the center of the spot. These microcolumns differ from those found within the laser spot in that they are plastered with redeposited material. The backside of the cross-section is covered with particulates, which have a size distribution ranging from nanometer to 10 μm particulates. This material charges substantially under a focused electron beam.

The microcolumn density at the sample's center shown in Figure 3.18 was 2.2×10^6 col/cm^2, while at 200 μm from the edge the density fell to 1.2×10^6 col/cm^2. For a freshly gas charged KrF laser tube, i.e., a raw energy output of 1.2 J, the maximum column density existed over roughly 70 – 90 % of the laser spot area.

The redeposition process is evident after 250/300 laser pulses. Small particles were ejected from the target and redeposited inside the laser spot, close to the edges (Figure 3.19). The redeposition of the particulates took place while the silicon was still liquid. The wave-like pattern left in the region around the particulates indicates that the freezing of the target took place immediately after the collision of the particulates with the target.

3.1.4 Fluence Dependence of the Microcolumn Morphology

Si microcolumns were formed in air in the fluence range 2.7 – 3.6 J/cm^2. Irradiation performed with an energy density of 2.7 J/cm^2 and *1000 laser pulses*, Figure 3.20, resulted in a morphology similar to that produced after 400 pulses at an energy density of 2.9 J/cm^2 (Figure 3.8). However, it is important to note that the photomicrograph shown in Figure 3.20 was taken in the center of the laser spot. The comparable morphology shown in Figure 3.8 is located midway between the laser spot center and the spot edge.

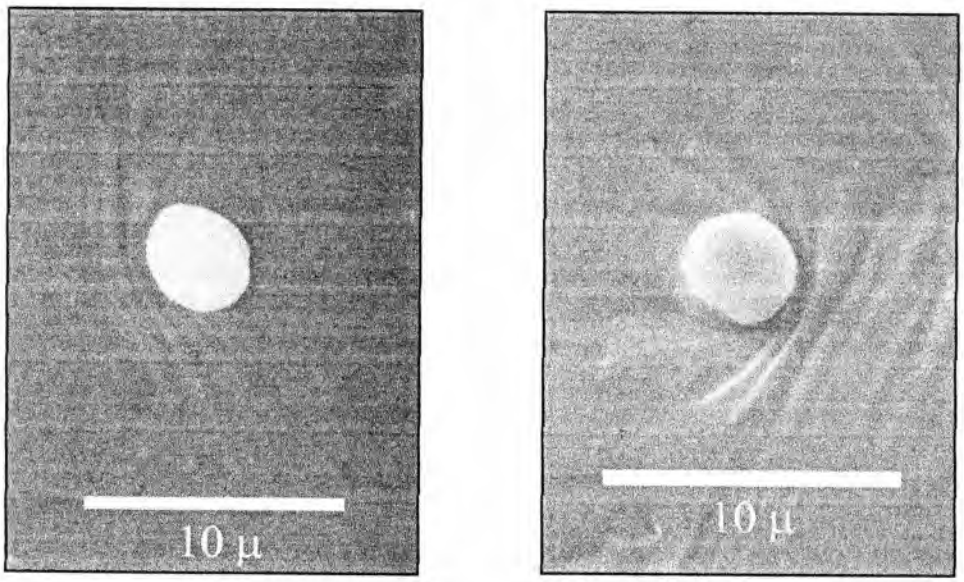

Figure 3.19 The Si target resolidified at the same time the particulates deposited on the wafer surface. The center of the laser spot lies between the two photos shown above. left) $E_d = 2.9$ J/cm^2, NOP = 300, and PRR = 1 Hz. right) $E_d = 2.9$ J/cm^2, NOP = 250, and PRR = 1 Hz. Both samples were irradiated in the presence of 1 atm air.

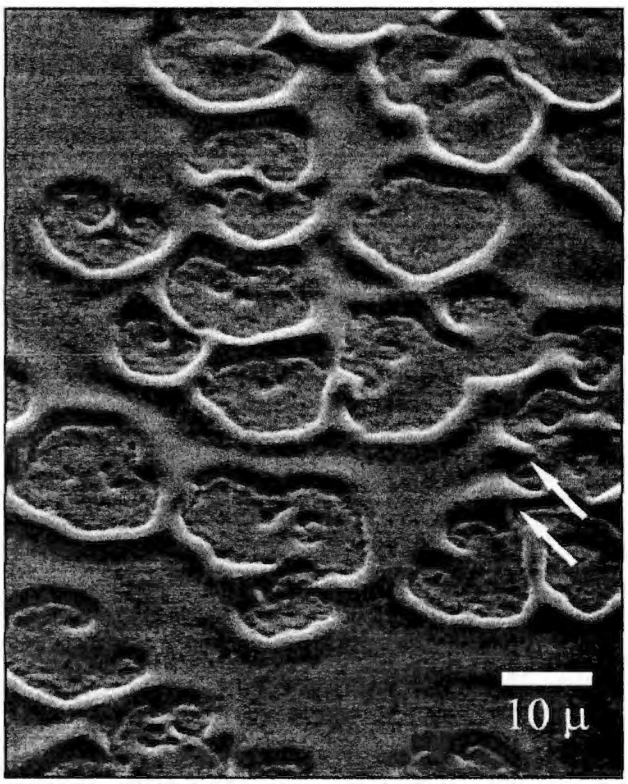

Figure 3.20 The morphology above, produced after irradiation with 1 000 pulses at a fluence of 2.7 J/cm^2, is identical to the surface modification generated with 400 pulses of fluence 2.9 J/cm^2. Lowering the fluence in the range for microcolumn formation acts to slow the evolution and growth rate of the microcolumns. PRR = 5 Hz and BG = air, 1 atm. The arrows point to surface ridges.

In essence, reducing the fluence has the affect of strongly impeding the microcolumn growth rate. The growth rate of the microcolumns decreases asymptotically for laser fluences approaching 2.7 J/cm^2.

On the other hand, for laser fluences higher than 3.6 J/cm^2 no columns formed and after 320 pulses the only surface features present were {100} oriented fracture grooves, Figure 3.21. In contrast to the asymptotic behavior at the lower fluence boundary, the morphology changed drastically at 3.6 J/cm^2.

Within the fluence range for microcolumn evolution, an increase in the fluence produces an increase in the growth rate of the microcolumns. Thus, the number of pulses required to produce the maximum microcolumn height decreases as the laser fluence increases from 2.7 – 3.6 J/cm^2. As an example, the wafer shown in Figure 3.13 received 250 laser pulses of fluence 3.3 J/cm^2, which produced an abundance of microcolumns with heights of ~ 20 μm. The sample exhibited in Figure 3.2 also received 250 pulses but with a lower fluence, 3.0 J/cm^2. No microcolumns populate the laser spot surface area shown in Figure 3.2. Also, the maximum microcolumn density is attained faster as the laser fluence increases.

3.2 The Chemical Composition and Crystallinity of the Microcolumns

Energy dispersive spectroscopy was employed to determine the chemical composition of the Si microcolumns. Figure 3.22a shows the EDS spectrum obtained from a Si microcolumn body. The EDS spectrum shows a large silicon peak and a small oxygen peak. The EDS spectrum of a fused silica standard, shown in Figure 3.22b, was used to determine the relative amounts of silicon and oxygen in the microcolumn body.

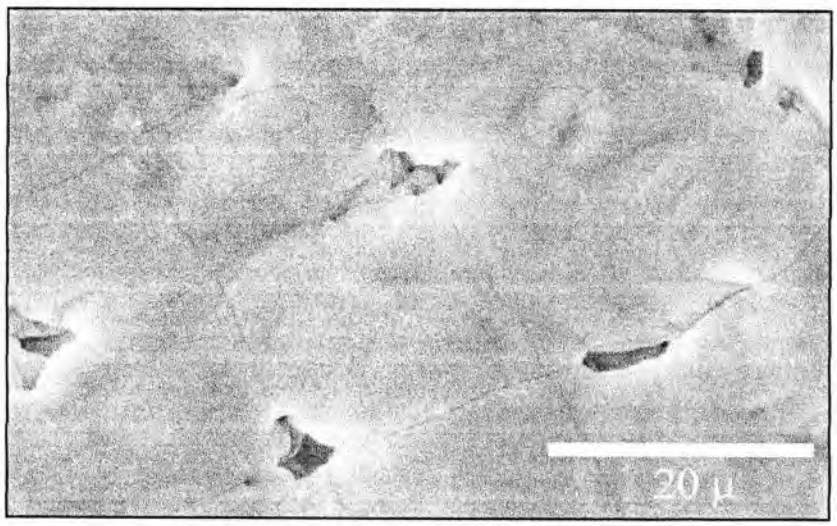

Figure 3.21 A fluence of ~ 4.0 J/cm^2 has produced a topography devoid of Si micro-columns. NOP = 320, PRR = 1 Hz, and BG = air, 1 atm.

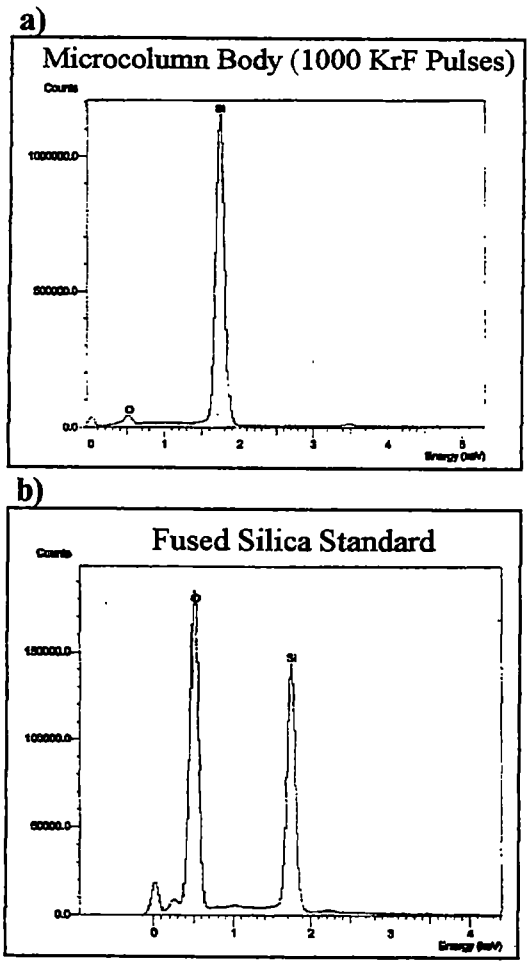

Figure 3.22 EDS spectrum of a Si microcolumn body and a fused silica standard. a) The top EDS spectrum was obtained at a location along the length of a Si microcolumn body. Comparing the microcolumn spectrum to the fused silica spectrum in b) shows the column body to be made mostly of silicon. A small concentration of oxygen is also present in the microcolumn body. $E_d = 3.2$ J/cm^2, NOP = 1 000, PRR = 3 Hz, and BG = air, 1 atm.

Comparison of the two spectra yields a high silicon concentration in the microcolumn body and a low oxygen concentration. EDS also verified the microcolumn tips to consist exclusively of Si. [60]

Auger depth profiling was used to pinpoint the location of the oxygen concentration. Sputtering along the column body and at the base of the column showed the oxygen concentration to be highest at the microcolumn surface. The oxygen concentration continued to decrease with depth into the microcolumns until ~ 1 500 Å into the material at which point the concentration leveled off. Figure 3.23 shows the Auger depth profiles for the column tip and body.

Auger depth profiling at the column tip showed a smaller oxygen concentration, relative to the column body, from the surface inward. The silicon concentration was highest at the column tip having a constant concentration value with sputter penetration. Small concentrations of carbon and nitrogen were detected at all sputtering locations.

X-ray 2θ scans of microcolumns grown on Si (100) wafer produced a diffraction pattern indicative of a silicon powder. The diffraction pattern is displayed in Figure 3.24. The peaks seen in Figure 3.24 are roughly in the correct intensity ratios of a randomly oriented powder. However, the Si (004) peak is larger in intensity than expected for Si a powder. Rocking the diffractometer about the (111) and (220) θ positions produced a constant signal over the entire rocking range in both cases.

3.3 Silicon Microcolumn Morphology formed in SF_6

The microcolumn morphology obtained in SF_6 after sequential laser irradiation differed substantially from the morphology produced in air. The structures formed in SF_6

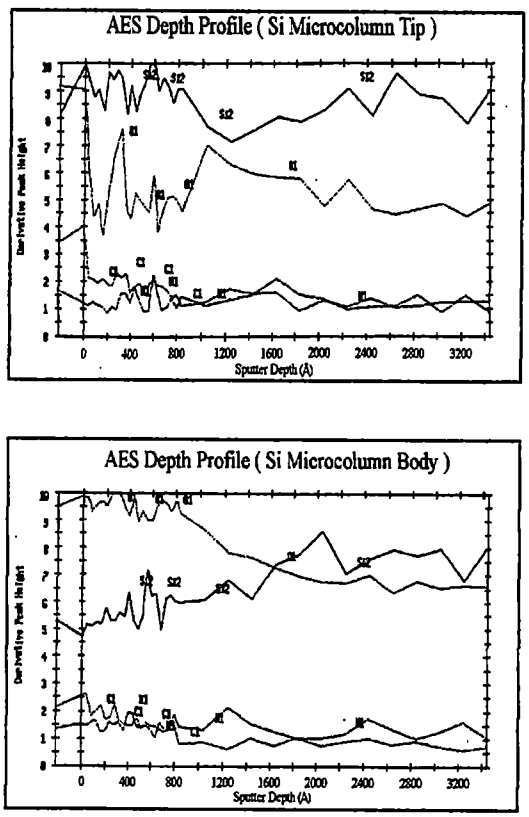

Figure 3.23 Auger electron spectroscopy and ion sputtering were used to probe underneath the microcolumn surface and determine the location of the oxygen concentration detected using EDS. The top profile a) shows the tip to consist mostly of silicon. Both the silicon and oxygen concentrations are constant with sputtering depth. In contrast, the bottom profile b) shows the oxygen to be primarily situated underneath the microcolumn body surface. Sputtering into the microcolumn body found the oxygen concentration to decrease until ~ 1 500 Å under the microcolumn body surface. After 1 500 Å the oxygen concentration became constant. E_d = 3.2 J/cm^2, NOP = 1 000, PRR = 3 Hz, and BG = air, 1 atm

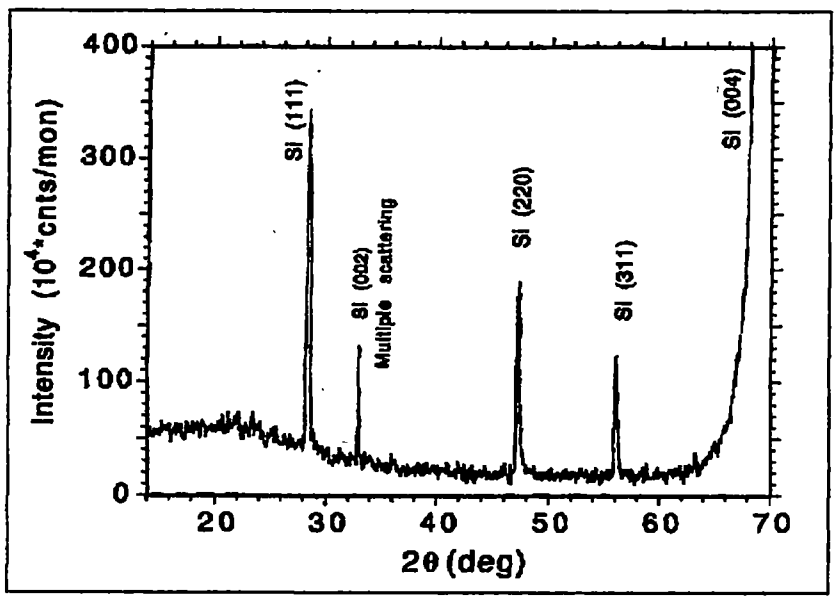

Figure 3.24 A diffraction pattern from a Si wafer that was irradiated with 1 000 pulses of energy density 3.4 J/cm^2. The diffraction pattern is in approximately the correct intensity ratios for a randomly oriented silicon powder. However, x-rays contributed to the pattern from both the underlying substrate and the redeposited material around the laser spot as well as the Si microcolumns. PRR = 4 Hz and BG = air, 1 atm.

were more conical, grew much higher, and had additional growth along their cone sides. Due to their more conical structure, the spikes fabricated in SF_6 will be referred to as microcones in contrast to the microcolumns formed in air. Overall, the morphology realized in SF_6 was much more complex than that afforded in air. The microcolumn morphology produced in SF_6 is shown in Figures 3.25 and 3.26.

3.3.1 Similarities in the Air and SF_6 Microcolumn Morphologies

The same spherical, drop-like shape is observed crowning the SF_6 microcones as was seen in the columns produced in air. Characteristics of the column tips produced in air, such as their diameter and morphology, were also observed in the SF_6 cone tips. For example, the cone tips were 2 – 3 μm in diameter and had the same concentric ring steps as the tips shown previously in Figure 3.14. Moreover, the microcolumn density was also patterned by the surface topography generated at low numbers of pulses. For instance, surface ridges formed adjacent to surface pits in SF_6, a similar phenomena to the forming of these same ridges adjacent to the {100} fractures produced in air.

The surface modification produced in SF_6 at low numbers of pulses is exemplified in Figure 3.27. Repetitive laser irradiation produced a periodic roughening of the wafer surface, i.e., a periodic surface structure (PSS). Pitting was also present in the SF_6 modified surface illustrated in Figure 3.27. The pitting produced during laser irradiation in SF_6 resembles the concentric wave pattern produced when a spherical droplet perturbs a smooth liquid surface. Moreover, the amount of pitting increased as the number of laser pulses increased. Surface ridges began to form in between the network of pits, when pit densities of ~ $1 - 2 \times 10^5$ pits/cm^2 were achieved. Numbers of pulses between

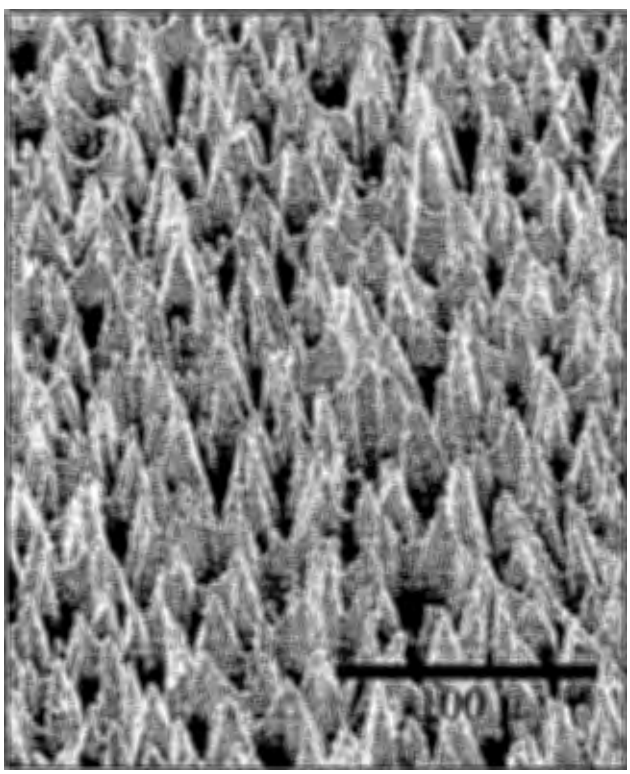

Figure 3.25 Irradiation in 1 atm SF_6 flowing at 0.20 SCFM with 2 040 KrF pulses produced the morphology above. The density and distribution of these structures is more consistent over the laser spot area compared with the columns fabricated in air. E_d = 1.5 J/cm^2, PRR = 3 Hz.

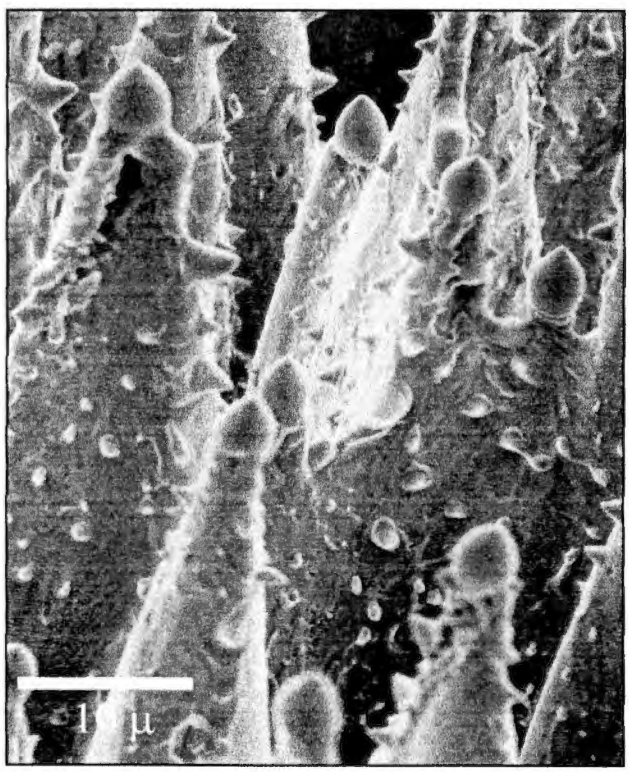

Figure 3.26 A secondary growth occurs on the SF_6 microcones normal to the primary growth direction. In common with air induced growth, each of the microcones has the 2 - 3 μm tip. E_d = 1.5 J/cm^2, NOP = 2 040, PRR = 3 Hz, and BG = SF_6, 1 atm (0.20 SCFM)

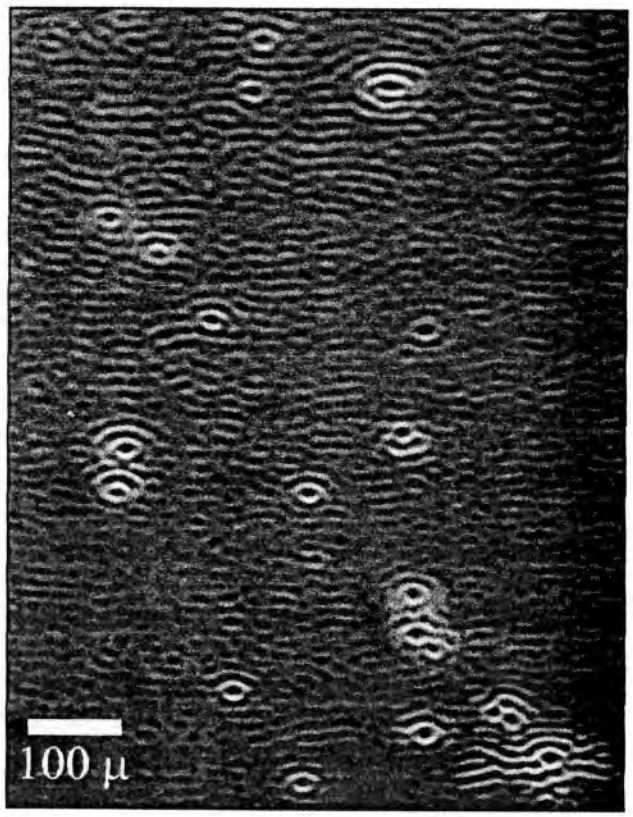

Figure 3.27 Following 750 pulses in SF_6, the Si microcones have yet to form. The pits shown in the figure have a surface roughness of ~ 4 000 Å. These pits are far larger in diameter than those found in the air morphology. $E_d = 2.9$ J/cm^2, PRR = 3 Hz, and BG = SF_6, 1 atm (< 0.1 SCFM)

700 – 1 000 were required to generate such high pit densities. Each individual surface ridge marks the site of a future Si microcone.

3.3.2 Temporal Evolution of Si Microcolumns in SF_6

The numbers of pulses required to initiate microcone growth in SF_6 is much higher than the prerequisite number in air. Following 750 laser pulses, each of energy density 2.9 J/cm^2, a PSS was produced on the (100) wafer surface as shown in Figure 3.27. By this time, a microcolumn density of ~ 2x10^6 col/cm^2 was produced in air under the same conditions.

The progression of laser spot profiles displayed in Figure 3.28 shows that surface roughness begins to increase at 750 laser pulses. This roughening is attributed to the concentric waves shown in Figure 3.27. A high magnification micrograph of the pitting phenomena is shown in Figure 3.29. The laser-induced pits in SF_6 have depths and diameters larger than those produced in air. For instance, surface profilometry on samples produced in SF_6 resolved individual etch pits. An etch pit 0.8 μm deep was produced after 300 pulses in SF_6 (Figure 3.30). The diameter of the profilometry probe prevents full penetration of the probe into sharp crevices such as that shown in Figure 3.30. Thus, depth measurements into these etch pits are understated.

Figure 3.31 exhibits the pits after 780 pulses in 1 atm SF_6. The number density of pits has increased and surface ridges have begun to form between adjacent pits. The surface ridges resemble exactly those produced in air. Each individual ridge has a bright point at its center and a diameter of 5 μm. The arrows in Figure 3.31 indicate wave-like steps

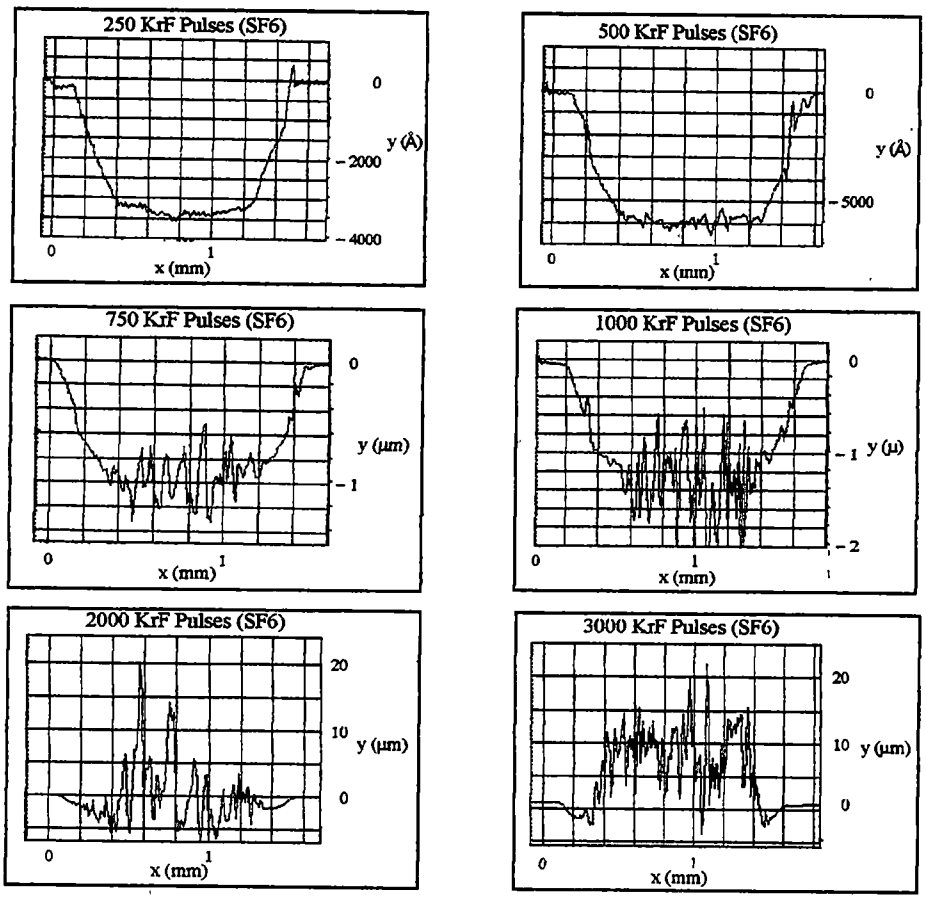

Figure 3.28 Topography profiles produced with increasing number of pulses at E_d = 2.9 J/cm^2, PRR = 3 Hz, and BG = 1 atm SF_6 (< 0.10 SCFM). Growth ensues quickly after 1 000 pulses with many columns protruding above the initial wafer surface by 20 μm. The depth of the pits are blurred due to the profilometer tip width.

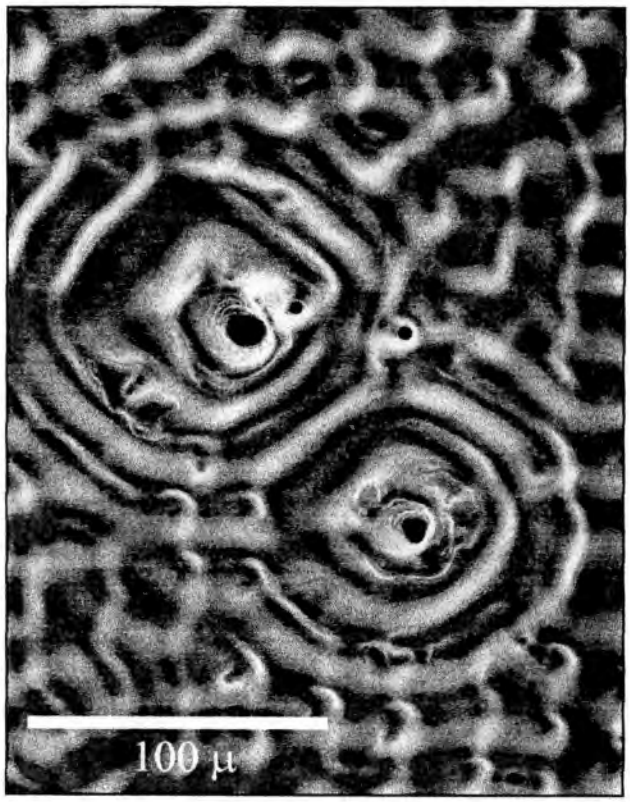

Figure 3.29 The waves surrounding the pits interrupt the background PSS. The pits penetrate deep into the wafer. E_d = 1.5 J/cm^2, NOP = 780, PRR = 3 Hz, BG = SF_6, 1 atm (0.20 SCFM).

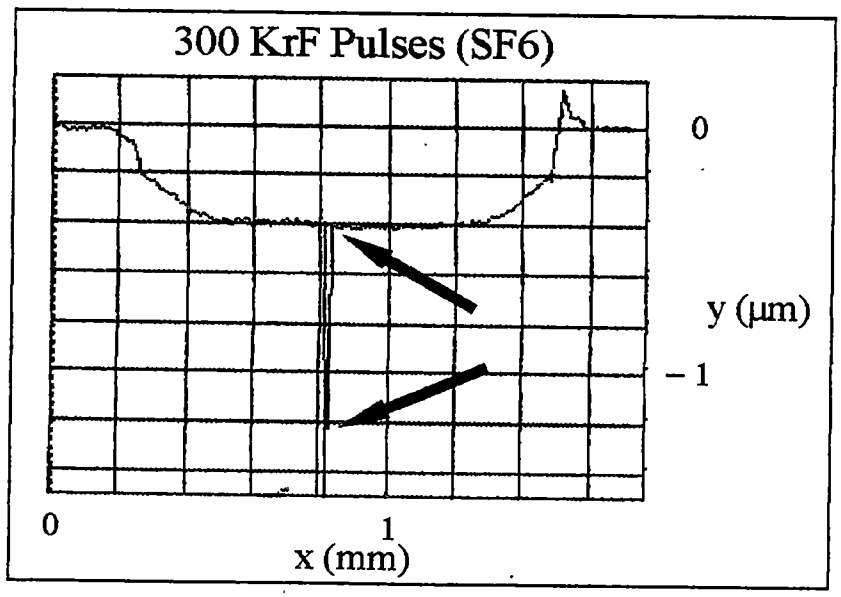

Figure 3.30 A profilometry scan across a laser groove that was produced with 300 KrF pulses in SF_6 gas. The pit shown in the profile is > 0.8 mm deep and has a diameter of ~ 20 μm at the surface. The profilometer tip width caused understatement of the pit depth shown in the above profilometry scan. E_d = 1.5 J/cm^2, NOP = 780, PRR = 3 Hz, BG = SF_6, 1 atm (0.20 SCFM).

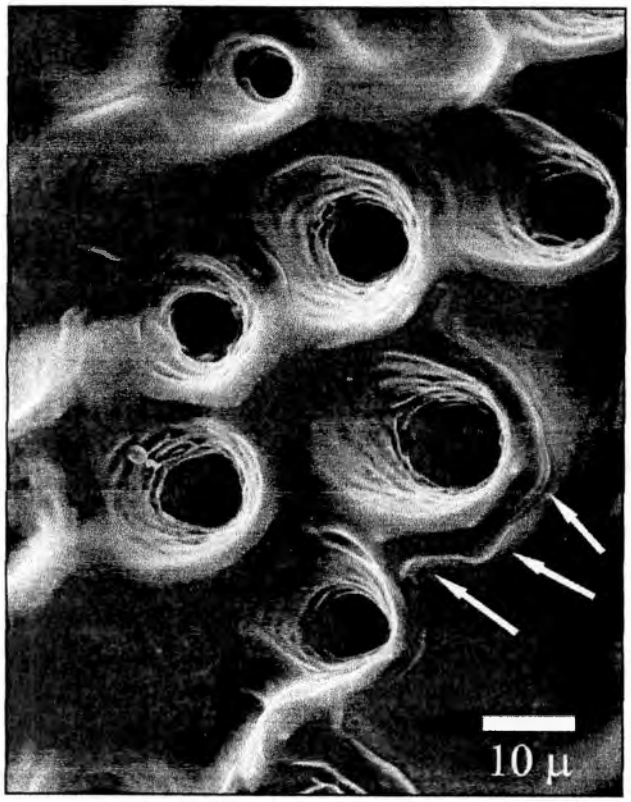

Figure 3.31 Pits have formed in the center of the laser irradiated area following 780 pulses each of energy density 1.5 J/cm^2. This photomicrograph was taken from the same wafer that is shown in Figure 3.29. This photomicrograph was taken at the center of the laser irradiated area where the pitting is more advanced. The photomicrograph shown in Figure 3.29 was taken adjacent to the center of the laser spot. Surface ridges are present around the perimeter of the pits shown in the above photomicrograph. E_d = 1.5 J/cm^2, NOP = 780, PRR = 3 Hz , BG = SF_6, 1 atm (0.20 SCFM).

running up the sides of the ridges. The ridges produced by irradiation in air and SF_6 can be compared visually by inspection of Figures 3.13 and 3.31.

As already mentioned, the structures produced by laser ablation/etching of SF_6 are more cone-like in morphology than columnar (Figure 3.26). Further, the microcones are connected at their bases in a network that spans over the laser spot area. The view looking down on the microcones, provided in Figure 3.32, clearly discerns the microcone network. The interconnection between microcones resembles the natural shape a rope attains when fixed at its ends under the force of gravity. The geometry of these interconnections is displayed in Figure 3.25. The circle superimposed on the micrograph in Figure 3.32 encloses an individual etch pit. A microcone array has developed around the pit.

The microcones begin to protrude above the initial wafer surface following 1 000 laser pulses. Following 2 000 laser pulses, the cones surpass the initial wafer surface by as much as 20 μm as shown in Figure 3.28. Also evident after 2 000 laser pulses are smaller, laterally growing cones located on the microcone sides (Figure 3.26). In fact, this lateral growth has been observed prior to microcone formation on the inside walls of several surface pits. The lateral cones located on the interior of the pits were < 1μm in length following 750 laser pulses.

The lateral cones displayed in Figure 3.26 range in size from hundreds of nanometers to 3 μm long. The more developed cones, i.e., the 3 μm structures, have growth steps, which run perpendicular to the lateral cone growth direction. Each growth step is ~ 0.1 – 0.4 μm thick. These growth steps are resolved clearly in Figure 3.33.

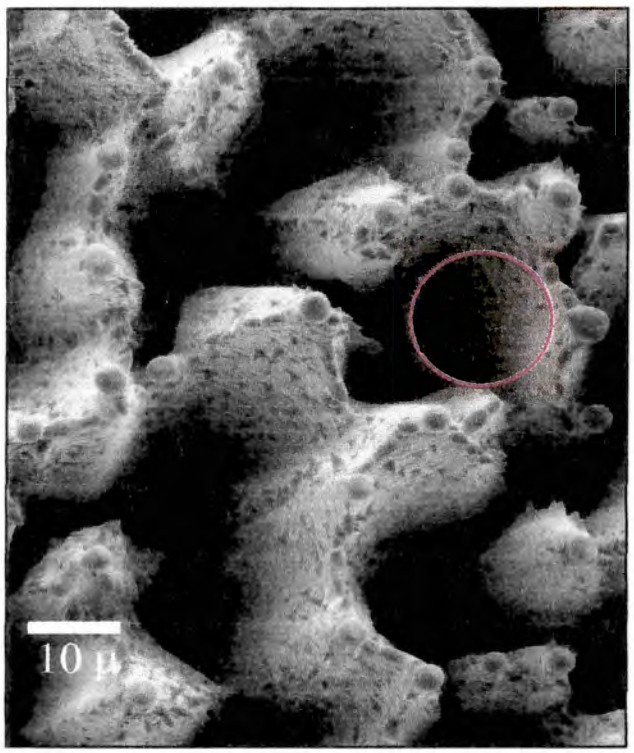

Figure 3.32 A network of interconnected Si microcones is produced when Si wafer is irradiated with 2 040 laser pulses in SF_6 gas. Each of the microcones in the figure are interconnected at their bases by Si bridges. The microcones surround pits which are at this point so deep profilometry is incapable of probing their depths. The circle above marks a pit. E_d = 1.5 J/cm^2, PRR = 3 Hz, and BG = SF_6, 1 atm (0.20 SCFM).



Figure 3.33 A secondary growth accompanies the primary microcone growth. The arrow points in the direction of the primary microcone growth direction. The secondary tips grow normal to the primary growth direction and are 1 - 3 μm long. E_d = 1.5 J/cm^2, NOP = 4 040, PRR = 3 Hz, and BG = SF_6, 1 atm (0.20 SCFM)

Figure 3.33 shows two sets of tracks on the conical surface of a microcone. One of the tracks is facing outward in the micrograph and the other is seen in side-view. The tracks run parallel to the symmetry axis of the cone and both of the tracks are ~ 2 μm in width. Lateral cones have formed along the length of both the illustrated tracks. Interestingly, the base thickness of the lateral cones and the track width are equal. In addition, each track is made of periodic steps. This morphology suggests that the lateral cones move in response to each laser pulse. Consequently, the lateral cones will leave behind tracks of periodic steps in response to cumulative laser irradiation.

3.3.3 The Fluence Dependence of the KrF – SF_6 Induced Microcone Morphology

The microcone morphology formed in a fluence range between 0.9 – 3.8 J/cm^2. A large number of pulses were required to generate the microcone morphology using an energy density of 0.9 J/cm^2. For example, microcones on the order of 10 – 15 μm high were produced following 6 000 laser pulses.[1] Referring to Figure 3.28, microcones of this length were produced between 1 000 – 2 000 pulses with a fluence of 2.9 J/cm^2. Thus, a threefold increase in fluence brought about a threefold increase in the growth rate. The same dependence of growth rate on fluence was found during KrF irradiation in air.

Irradiation in an SF_6 ambient with a fluence of 3.8 J/cm^2 induced a rapid recession of the wafer floor below the original wafer surface. The microcone morphology was still produced at this higher fluence however the cones did not protrude above the initial target

[1] In this particular comparison, the word height refers to the portion of the microcones that protrudes above the initial Si wafer surface, **not** the total microcolumn height.

surface. The tips of the microcones shown in Figure 3.34 have receded a distance of ≥ 50 μm below the original surface after 2 500 pulses. The right-edge of the laser spot is shown in Figure 3.34 to help in visualization of the recession process. Ultimately, a fluence of 3.8 J/cm^2 or greater proves an effective fluence regime for laser micro-machining.

3.4 Background Gases not Accessory to Si Microcolumn Evolution and Growth

Under conditions favorable for column growth in air and SF_6, several background gases failed to produce the high-aspect ratio, spike morphology. Irradiation performed in Ar, N_2, 5% H_2 – Ar, and He yielded "low" roughness morphologies, i.e., morphologies that did not break the original wafer surface. The surface roughness so observed fell under descriptions such as PSS or LIMS.

Figure 3.35 shows the surface modification resulting from 1 320 KrF pulses in 5% H_2 – Ar. The pitting apparent in the micrograph riddles the surface in a pepper-like fashion along the surface-exposed {100} planes. Moreover, the pits are very small, on the order of ≤ 1 μm. Round undulations, similar to those fabricated in air with 250 laser pulses (Figure 3.3), exist on the surface adjacent to the sparse pitting. However, these undulations are not surface ridges because they lack the bright point atop each ridge and fail to yield the spiked morphology.

Surface profilometry done on Si samples irradiated in He displayed a decrease in material removal compared with profilometry data from irradiation in either air or SF_6. Figure 3.36 shows material removal rates by KrF laser irradiation in the presence of air,

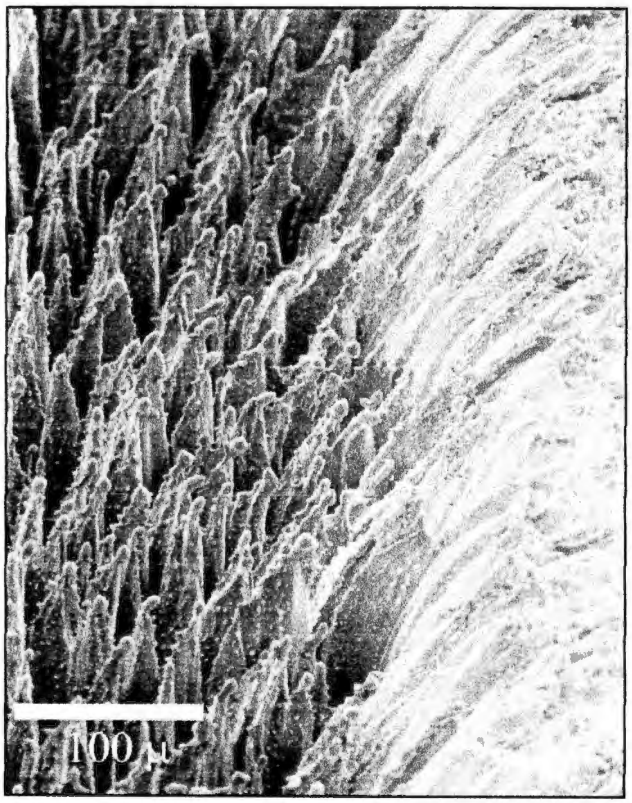

Figure 3.34 The etching rate of Si (100) in SF_6 increases substantially at fluences greater than or equal to 3.8 J/cm^2. The wafer floor has begun to recede away at such a fast rate (the above photomicrograph) that the microcones can no longer grow fast enough to protrude above the wafer surface. The microcone tips in this case are >50 μm below the wafer surface. Continuation of irradiation over the 2 500 pulses provided here would eventually drill through the back of the wafer. E_d = 3.8 J/cm^2, PRR = 5 Hz, and BG = SF_6, 1 atm (< 0.10 SCFM)

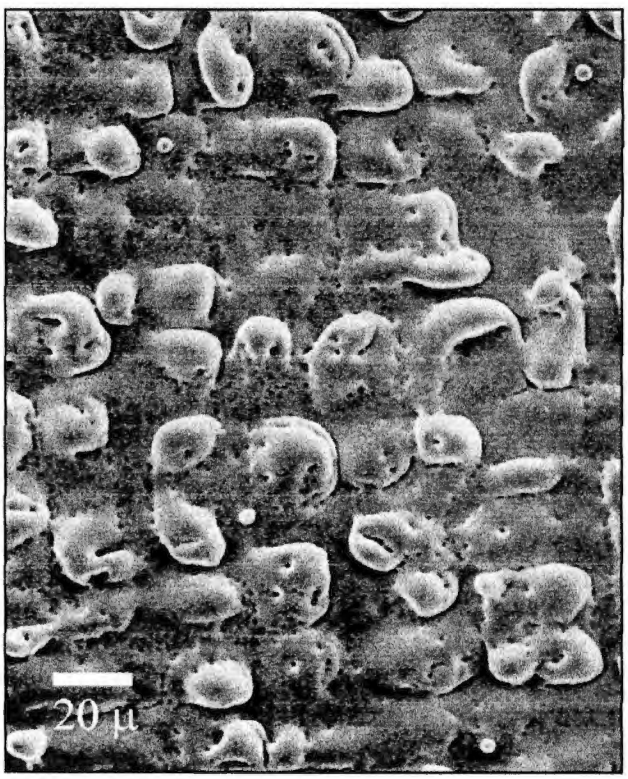

Figure 3.35 1 320 pulses in 5% H_2 - Ar did not produce the microcolumn morphology. The amount of pitting on the Si surface is reduced when irradiation iscarried out in 5% H_2-Ar compared with irradiation in either air or SF_6. E_d = 3.5 J/cm^2, PRR = 4 Hz, and BG = 5% H_2 - Ar, 1 atm (0.20 SCFM)

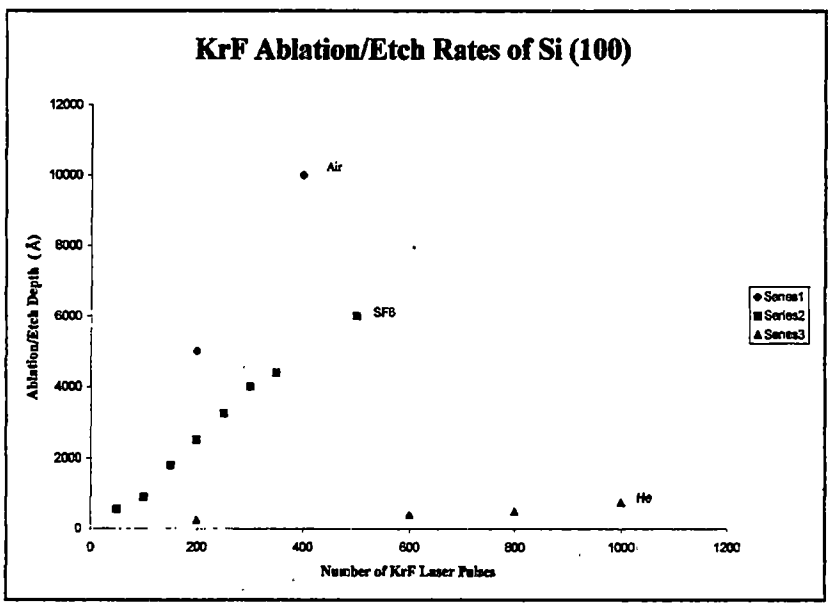

Figure 3.36 A plot of the ablation/etch depth vs. the number of laser pulses of Si in air, SF_6, and He. Material removal rates, taken as the slopes of the above plots, were 25 Å/pulse for air, 12 Å/pulse for SF_6, and 1 Å/pulse in He. The data were collected on Si samples that were irradiated with an energy density of 2.9 J/cm^2.

SF_6, and He. The data points for air and SF_6 shown in Figure 3.36 were produced at low numbers of pulses. In fact, microcolumn/microcone growth was not produced in any of these samples. The onset of microcolumn/microcone growth makes it difficult to determine ablation/etch rate data from profilometry scans.

KrF laser pulses removed silicon in the presence of air at a rate of 25 Å/pulse. When the background gas was switched to SF_6 the material removal rate fell by half to 12 Å/pulse. Helium was the least efficient aid in material removal ablating/etching at a rate of ~ 1 Å/pulse.

Irradiation was performed in air and followed by illumination in the non-spike yielding gas environments, i.e., Ar, He, etc., in an attempt to catalyze microcolumn growth. Following 400 laser pulses in air, 2 160 additional pulses in an ambient of N_2 were provided to a Si wafer. The result of the combined irradiation, a smooth, laser-induced micro-rough structure, is shown in Figure 3.37. A similar irradiation procedure carried out in air and then Ar produced a complementary morphology to the topography shown in Figure 3.35. It was found that dual irradiation in air and any of the following gases; Ar, He, or N_2, failed to initiate microcolumn evolution and growth.

3.5 The Effect of Background Gas Changes during Irradiation on Preexisting Morphology

The background gas was changed during irradiation, using several gas combinations, to aid in unveiling the active column growth mechanism. First, either air or SF_6 was used to initiate microcolumn growth. Once growth ensued, a background gas change was

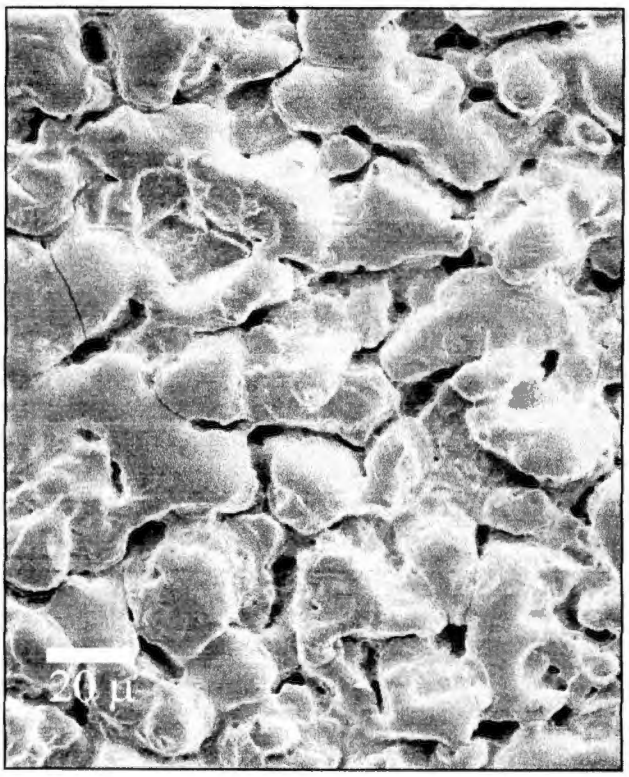

Figure 3.37 The Si wafer was irradiated in two different gas environments. 400 pulses in air at a fluence of 3.1 J/cm^2 produced the surface ridges critical for Si microcolumns evolution. An additional 2 160 pulses in N_2 produced the morphology seen above. E_d = 3.0 J/cm^2, PRR = 3 Hz, and BG = N_2, 1 atm (0.20 SCFM). Even after aid from irradiation in air, the microcolumn morphology still did not form in the N_2 ambient.

instituted to determine, for example, whether spike growth would continue atop the preexisting spike morphology or if the preexisting morphology would be replaced.

Irradiation first performed in air with 750 laser pulses is shown in Figure 3.38. The microcolumn shown in the figure has periodic steps running adjacent to the column's long dimension. The spacing of the periodic steps is ~ 1.5 μm. The steps closer to the column's base had begun to show substantial surface modification.

The experimental conditions used to generate the column in Figure 3.38 were repeated *and followed* by an additional 100 pulses in pure oxygen. The additional irradiation in 100% O_2 produced a sleeve of material which enclosed the preexisting Si microcolumns. The dual gas environment topography is displayed in Figure 3.39. The electron-beam charging phenomenon, previously shown in Si cones formed from irradiation in air with 1000 + laser shots, also occurred in the air – O_2 twofold irradiation, fabricated microcolumns.

Si wafer illuminated by KrF radiation in air followed by irradiation in SF_6 produced the morphology shown in Figure 3.40. The first surface modification, 2 000 laser pulses in SF_6, generated the microcones displayed in Figures 3.25 and 3.26. A schematic representation of the microcone morphology is shown in Figure 3.41. The second Si wafer surface modification consisted of irradiation with 500 pulses in the background gas 5% $O_2 - N_2$. Figure 3.40 shows that the irradiation in 5% $O_2 - N_2$ produces the air-specific microcolumns *atop the preexisting SF_6 microcones.* Microcolumn growth ensued during the second illumination at the 2 – 3 μm spherical tip on each microcone. A filamentary, chaotic-type fuzz surrounds the cones following the illumination in 5% O_2

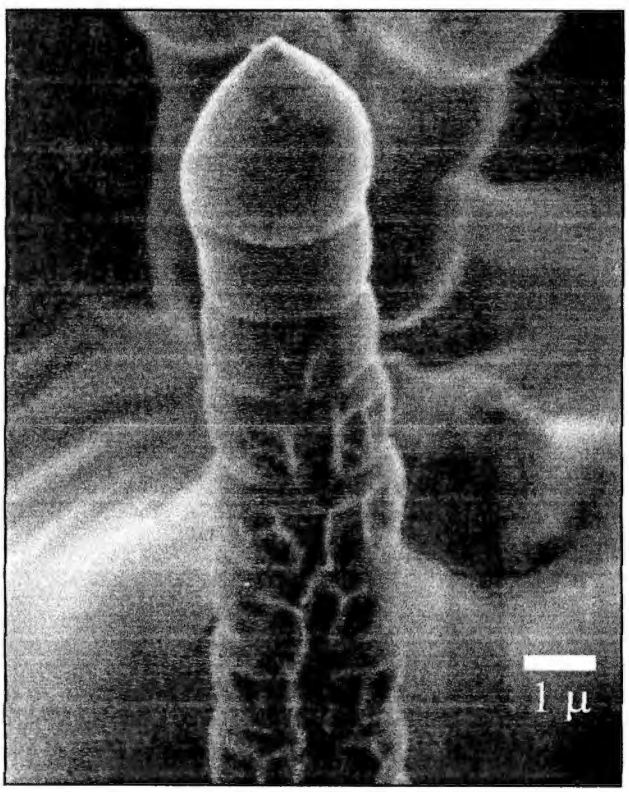

Figure 3.38 Si microcolumns grown with numbers of laser pulses between ~ 500 - 1 000 have periodic changes in their diameters that oscillate along each column's length. Locations on the lower portion of the column shown above have been modified in response to the cumulative laser illumination. E_d = 3.2 J/cm^2, PRR = 5 Hz, NOP = 750, and BG = air, 1 atm.

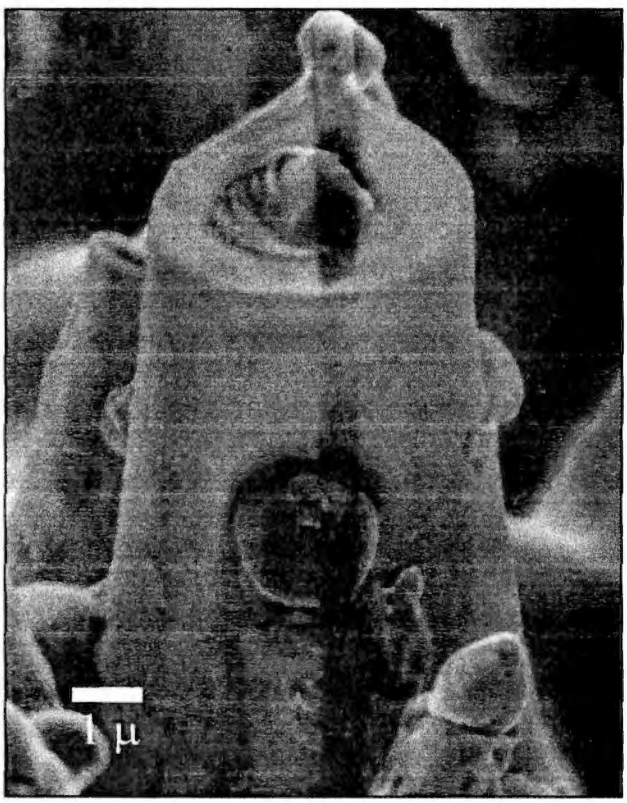

Figure 3.39 A Si microcolumn that has been wrapped in a sleeve of oxide following a two-stage laser irradiation treatment in air followed by O_2. The above structure was fabricated by first generating the morphology shown in Figure 3.38. The background gas was then changed to pure oxygen and 100 pulses were provided in this environment. The result is a column from Figure 3.38 being wrapped in a sleeve of material after illumination in O_2.

1) $E_d = 3.2$ J/cm^2, BG = air, 1 atm, NOP = 750, and PRR = 5 Hz.

2) $E_d = 3.2$ J/cm^2, BG = O_2, 1 atm (0.15 SCFM), NOP = 100, and PRR = 5 Hz.

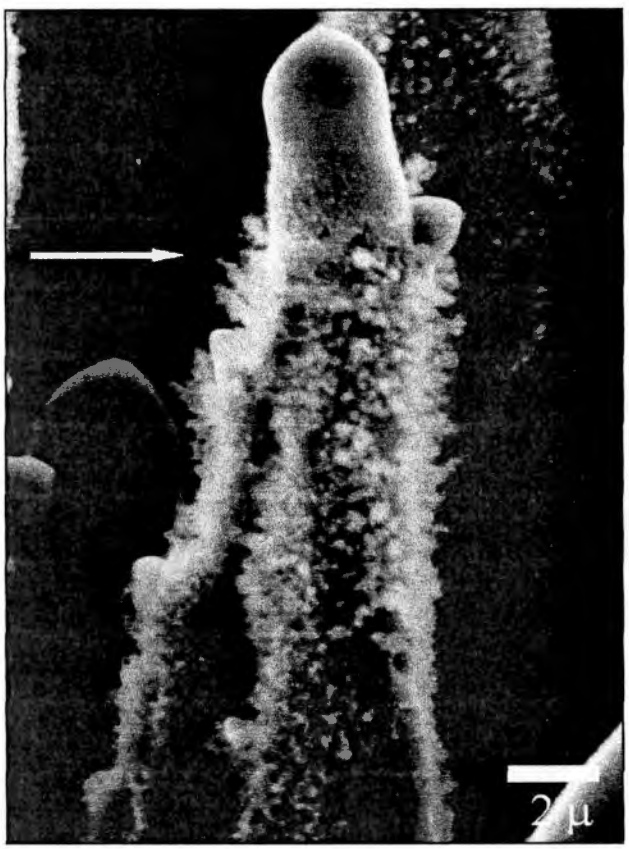

Figure 3.40 Microcolumn growth in 5% O_2 - N_2 has ensued at the preexisting SF_6 microcones tips. The arrow points to the step in growth where the background gas was switched. A filamentary, chaotic-type growth accompanied irradiation in air. 1) $E_d = 2.9$ J/cm^2, NOP = 2 000, PRR = 3 Hz, and BG = SF_6, 1 atm (< 0.10 SCFM) and 2) $E_d = 2.9$ J/cm^2, NOP = 500, PRR = 3 Hz, and BG = 5% O_2 - N_2, 1 atm (< 0.10 SCFM).

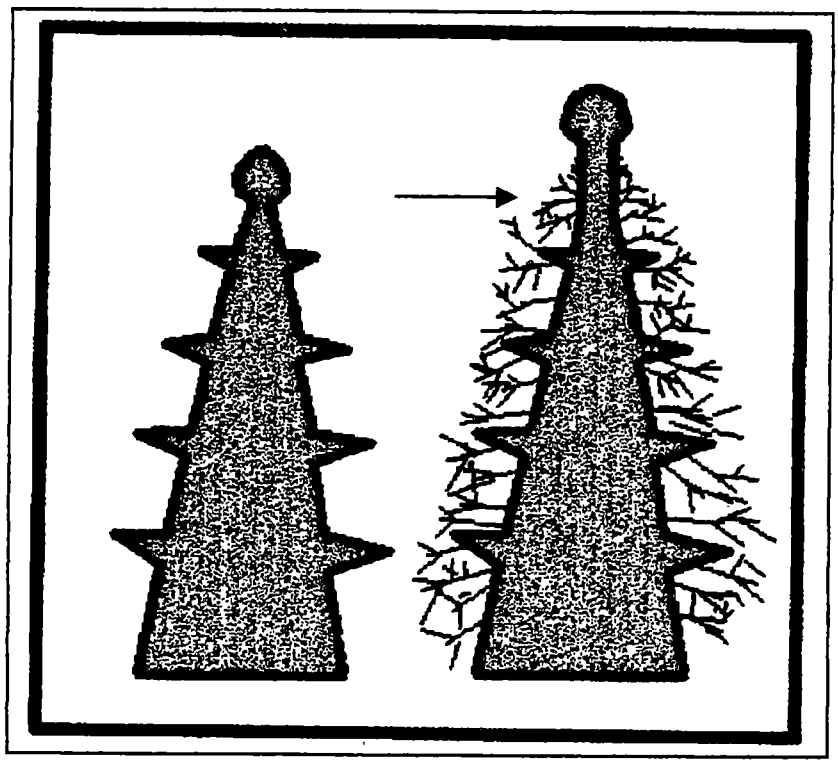

Figure 3.41 A schematic representation of the morphology that results when the fully-developed microcone structures are irradiated with 500 KrF pulses in 5% O_2 - N_2. 2 000 laser pulses in SF_6 produces the left-most morphology in the figure A background gas switch to 5% O_2 - N_2 and 500 additional laser pulses initiates continuation of growth at the microcone tips. A nanometer-sized fractal growth encompasses the microcones after irradiation in 5% O_2 - N_2. The arrow above points to the step corresponding to the cone's height when the background gas switch occurred.

- N_2 and is clearly shown in Figure 3.42. Figure 3.41 provides a schematic representation of the morphology after dual irradiation in SF_6 and air.

3.6 Microcolumn Morphology Changes Induced by an Oxygen Partial Pressure Reduction

The plot of microcolumn density vs. the number of laser pulses displayed in Figure 3.10 shows that a ¾ reduction in the oxygen concentration in a 1 atm 20% $O_2 - N_2$ gas mixture reduces the column density by ½. Figure 3.43 shows the difference in the microcolumn morphology produced from irradiation in 5% $O_2 - N_2$ contrary to air. Effectively, the microcolumns produced in 5% $O_2 - N_2$ were more perfect structures. The term "perfect" in this context means the spikes were more columnar with their periodic steps in growth resolved. The microcolumns shown in Figure 3.43b are more conical in shape with smooth, shapeless sides. Replacing N_2 with Ar in the $O_2 - N_2$ gas mixture provided another means to improve the shape of Si microcolumns produced in air.

3.7 N_2 Removal from the Microcolumn forming Ambient

The advantage of removing N_2 from the gas ambient was the production of well-defined microcolumn structures. The microcolumn shown in Figure 3.44 was produced by 2 000 pulses in 20% $O_2 - Ar$. The drawback in using Ar to produce the improved-shape microcolumn was a decrease in the microcolumn density. Ar had the affect of reducing the number of column-precursor surface ridges that in turn reduced the possible number density of microcolumns. Figure 3.45 exhibits the wafer floor topography change resulting from the nitrogen to argon gas switch.

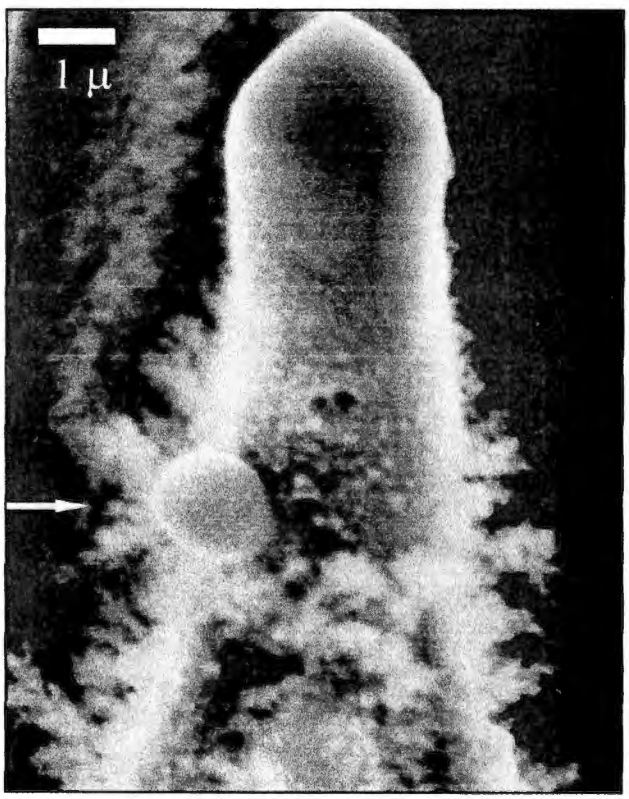

Figure 3.42 A higher magnification micrograph of the growth step in a dual microcone - microcolumn. Photo from the same sample as shown in Figure 3.41.

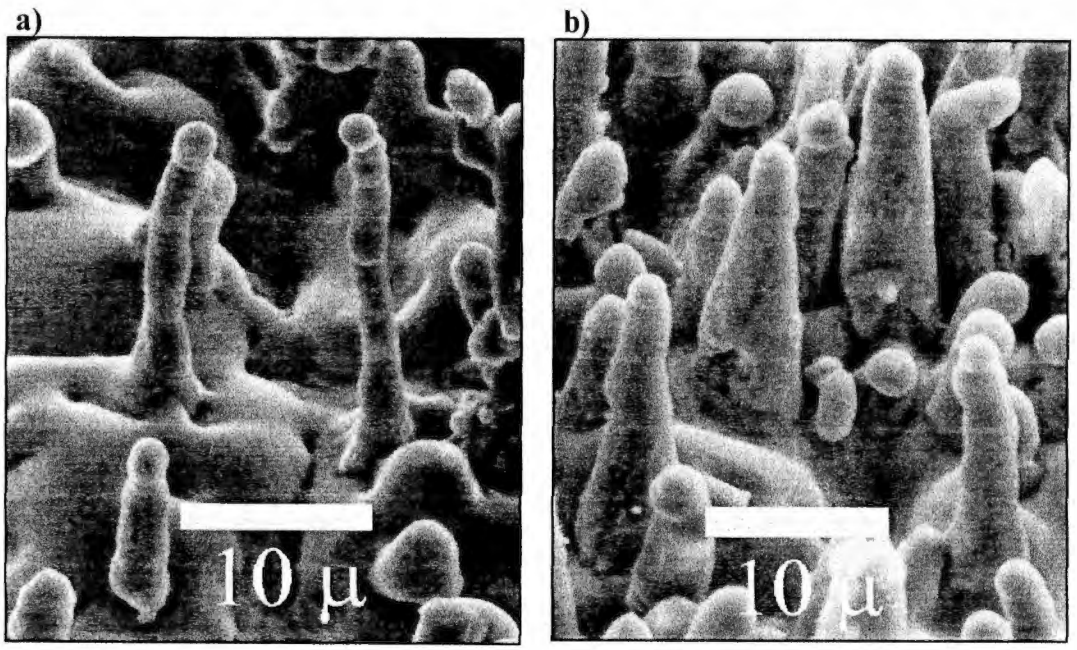

Figure 3.43 Si microcolumns fabricated in 5% O_2 - N_2 (left figure) are columnar-like structures with constant column diameters. In contrast, Si microcolumns produced in air have more cone-like shapes. As evident from comparing the figures , the microcolumn density decreases when the oxygen concentration in an O_2 - N_2 gas mixture is decreased. a) E_d = 2.9 J/cm^2, PRR = 4 Hz, NOP = 1 800, and BG = 5% O_2 - N_2, 1 atm (< 0.10 SCFM) and b) E_d = 2.9 J/cm^2, PRR = 4 Hz, NOP = 1 200, and BG = air, 1 atm.

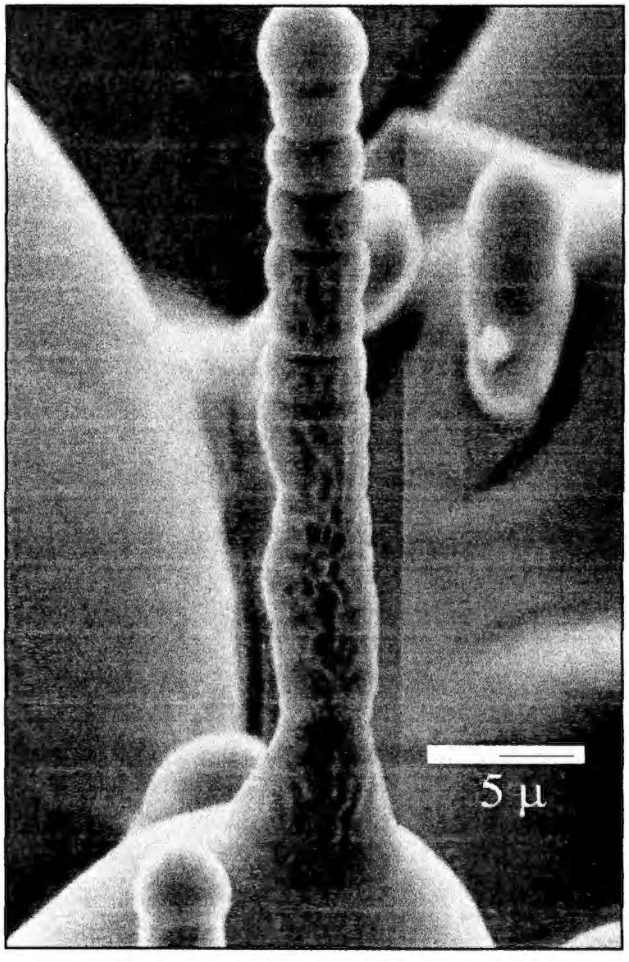

Figure 3.44 A Si microcolumn formed in 20% O_2 - Ar. Removal of N_2 gas from the ambient has further reduced the amount of lateral material encompassing the column. (Compare with the 5% O_2 - N_2 microcolumn in Figure 3.43a) E_d = 2.9 J /cm^2, PRR = 2 Hz, NOP = 2 000, and BG = 20% O_2 - Ar, 1 atm, (134 SCCM O_2 and 500 SCCM Ar)

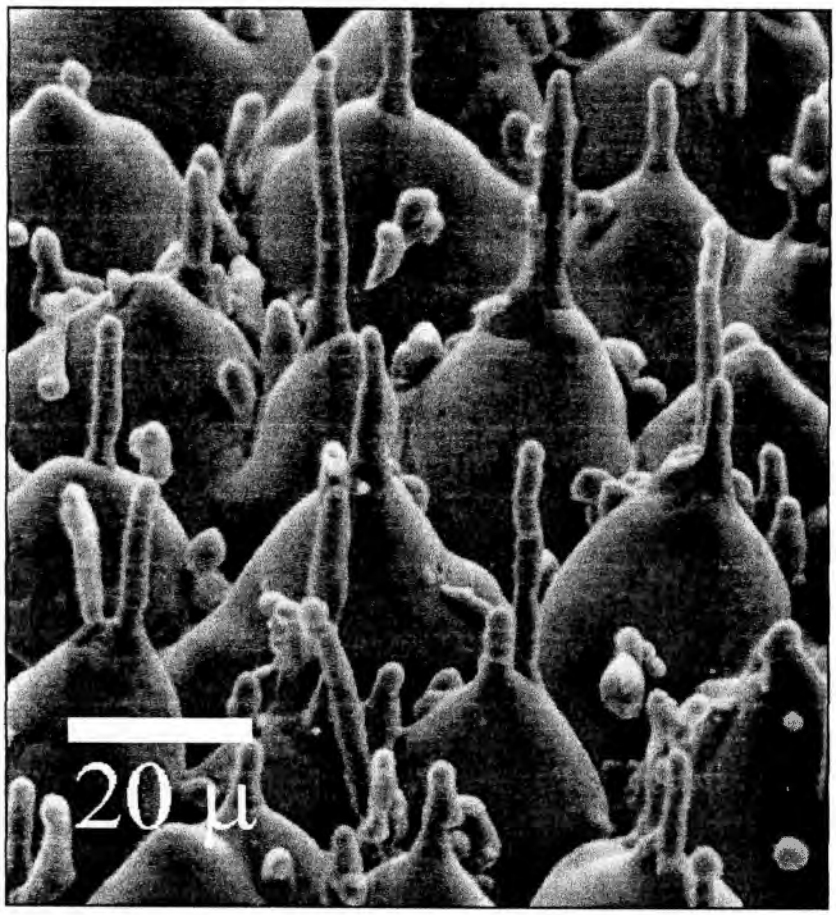

Figure 3.45 Irradiation in the presence of Ar causes a decrease in the surface ridge density and hence a reduction in the microcolumn density. A change in wafer floor morphology has also arisen from the oxygen gas solvent switch from N_2 to Ar. $E_d = 2.9$ J/cm^2, NOP = 2 000, PRR = 2 Hz, and BG = 20% O_2 - Ar, 1 atm, (134 SCCM O_2 and 500 SCCM Ar).

3.8 The Effect of Reducing the Total Pressure of Air on Si Microcolumn Height

Sequential laser irradiation in a total pressure of air < 1 atm increased individual microcolumn height and decreased the microcolumn density. Table 3.1 lists the average, maximum microcolumn height in three different background gas pressures. The averages in Table 3.1 were obtained by measuring the ten tallest microcolumns in an area of 700 x 700 μm^2. The area examined was in the very center of the laser spot and the same area in the laser spot was investigated in each sample.

The maximum Si microcolumn height produced from 1 500 laser pulses increased by ~ 10 μm when the total pressure of air in the chamber was reduced from 760 Torr to 1 Torr. After 3 000 pulses in 1 Torr air no substantial increase in the average, maximum microcolumn height was observed compared with the data at 1 500 pulses in 1 Torr air. After 6 000 laser pulses in a total air pressure of 0.2 Torr, no microcolumns formed.

Figure 3.46 shows a comparison of the microcolumn morphology produced with 1 000 laser pulses in 760 Torr air and 100 Torr air. A substantial decrease in microcolumn density occurred when the total pressure of air was decreased. Also apparent in Figure 3.46 is the increase in the maximum height of the microcolumns as the total pressure of air is decreased.

The Si microcolumns produced in 1 Torr air with 3 000 laser pulses were more cylindrical in morphology than Si microcolumns fabricated with 1 500 laser pulses in 760 Torr air. Figure 3.47 exhibits the contrast in morphology and microcolumn density from reducing the air pressure in the irradiation chamber. Many conical structures were present when the irradiation was performed in 1 atm air. Moreover, several of the conical

Table 3.1 Average, maximum microcolumn height as a function of the total pressure of air present during KrF irradiation of Si (100) wafer.

Dopant Type	Fluence (J/cm^2)	# of Pulses	Hz	Ambient	Pressure (Torr)	Wafer Orientation	Avg. Max. Microcolumn Height (μm)	Standard Deviation
n-Si	2.8	1500	3	air	760	100	22	0.187
n-Si	2.8	1500	3	air	0.86	100	31	3.50
n-Si	2.8	3000	3	air	0.86	100	33	2.92
n-Si	2.8	6000	3	air	0.16	100	0	0

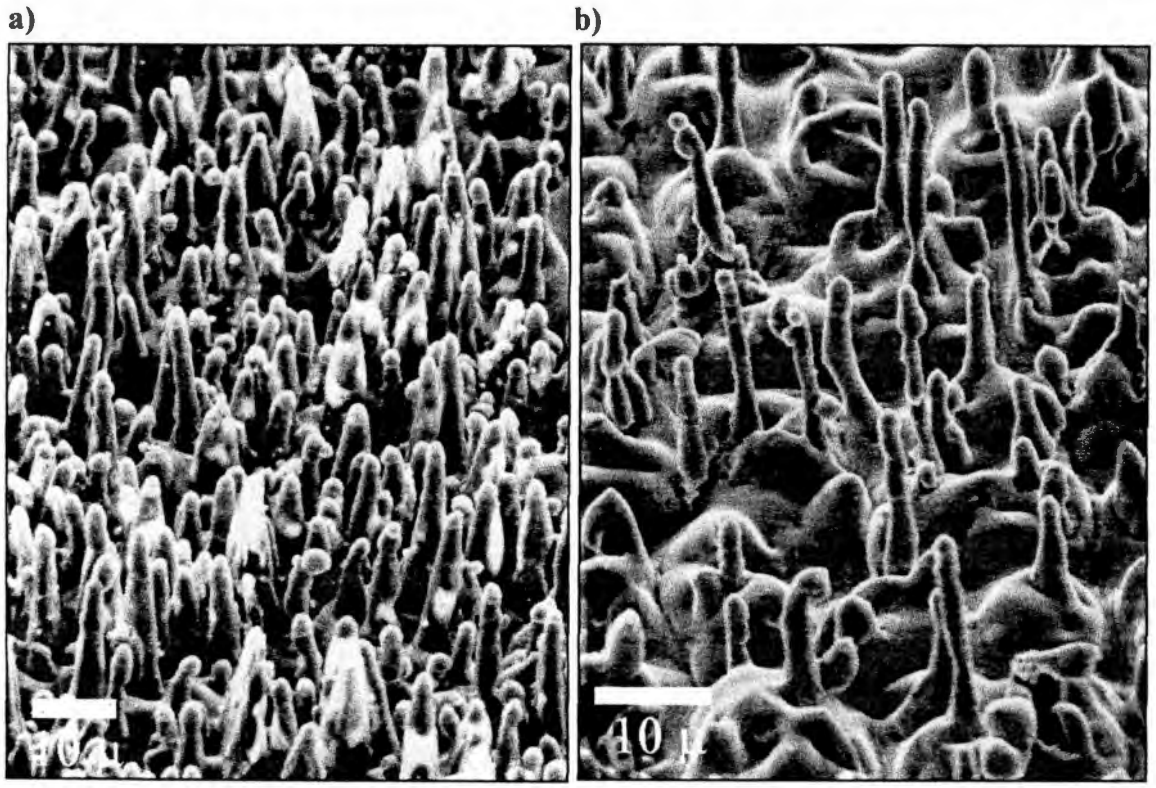

Figure 3.46 The Si wafer in a) was irradiated in 760 Torr air. $E_d = 2.9$ J/cm^2, NOP = 1 000, and PRR = 2 Hz. Irradiation under the same conditions in 100 Torr air is shown in b). The microcolumn density has decreased as a result of the decrease in total air pressure. Several of the microcolumns produced in the 100 Torr air environment are 5 - 10 μm taller than those in a).

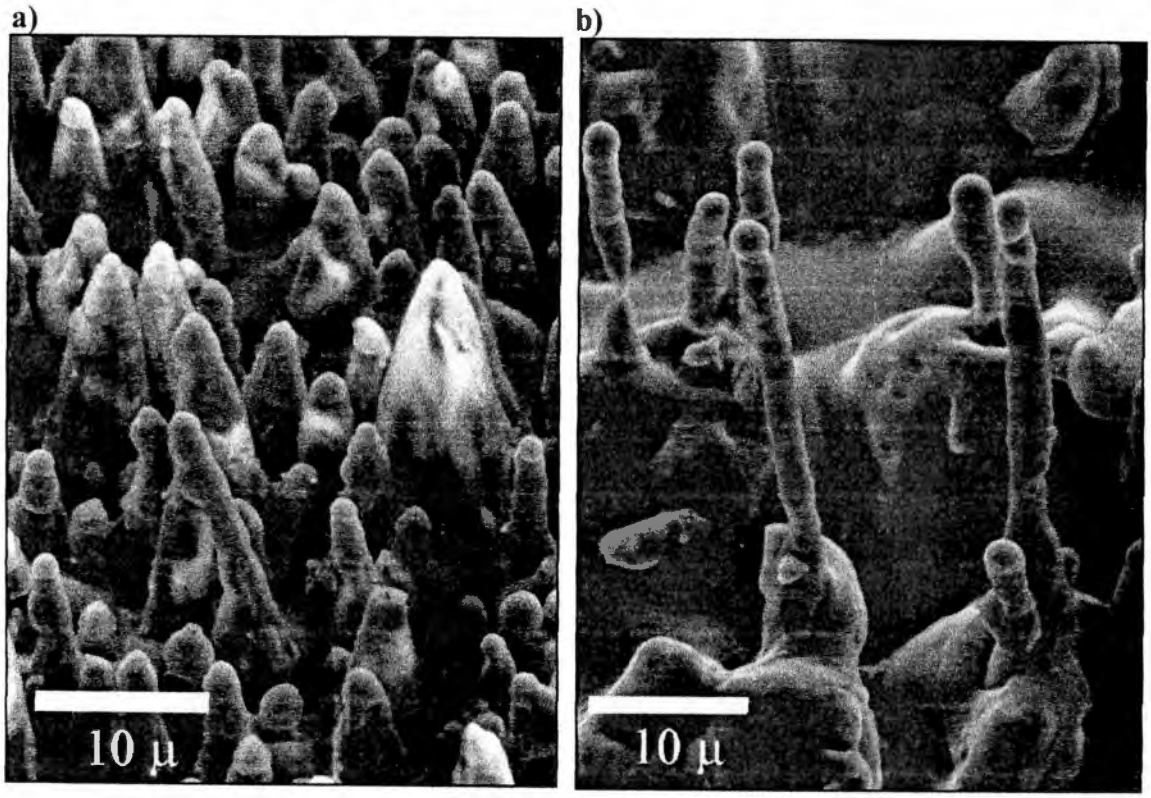

Figure 3.47 The Si microcolumns produced in 1 Torr air b) are more cylindrical than those produced in 760 Torr air a). a) $E_d = 2.8$ J/cm^2, PRR = 4 Hz, and NOP = 1 500. b) $E_d = 2.8$ J/cm^2, PRR = 4 Hz, and NOP = 3 000.

structures in Figure 3.47a charged in the SEM microscope whilst no charging was observed from the cylindrical microcolumns produced in the 1 Torr air atmosphere.

3.9 The Etching of Si Microcolumns by 5% HF Acid

Etching experiments were conducted to determine the chemical composition of the microcolumn component responsible for electron-beam charging. A minimum number of laser pulses was required to produce a substantial population of cones intermixed among columns. Once the cone morphology was produced, the wafer was dipped in 5% HF solution to preferentially attack stable SiO_2 if present. Figure 3.48 shows the result of a 15 minute etch following 2 200 KrF pulses. The microcolumn in the foreground remained unscathed through the etching procedure whilst the cone in the background was etched around its periphery.

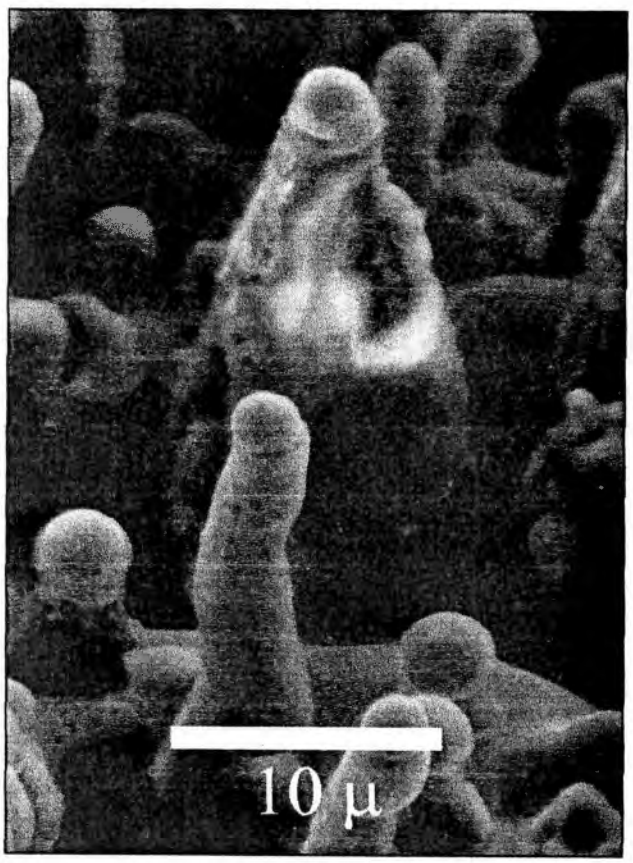

Figure 3.48 Irradiation with 2 200 pulses in air generated a forest of both Si microcolumns and cones. A 15:00 min. etching procedure followed the irradiation to determine the compositional difference between Si microcolumns and cones. The etchant did not attack the microcolumn in the foreground. However, the cone in the background was attacked around its perimeter. The etchant, HF, preferentially attacks SiO_2. 1) $E_d = 3.4$ J/cm^2, PRR = 3 Hz, BG = air, 1 atm and 2) 15:00 5% HF etch.

Chapter 4

Discussion

The Literature Review section of this work presented several currently accepted models that describe the characteristic cone morphology produced in a wide range of materials from pulsed laser irradiation treatment. In the following discussion, my experimental results were thoroughly scrutinized to determine if any of these aforementioned models properly account for the experimentally produced morphology. It was found that these models were inadequate to describe all the characteristics of the laser-treated Si wafer surface. The Si microcones/microcolumns were found to grow by a combination of hydrodynamic processes in molten Si and a "catalyst-free" VLS mechanism.

4.1 The Erosional Sputtering Mechanism

The growth mechanism of the Si microcones/microcolumns is clearly different from one involving erosion resistant tips because microcone/microcolumn growth takes place above the original wafer surface. Further, the growth of Si microcones/microcolumns depends on the background gas present in the surface modification chamber during laser irradiation. Thus, the only plausible way that an erosion resistant region could form on the surface would be through a gas phase – liquid Si chemical reaction, during melting of the Si, which could produce a radiation resistant compound.

EDS spectrum coupled with AES and ion sputtering depth profiling showed that the Si microcolumns contained only silicon with a minor oxygen component at the surface. The

tip surface of each microcolumn should be the location where the radiation resistant layer resides if present. The Si microcolumn tips were found to have the lowest concentration of oxygen of all the locations on the microcolumn checked. The small oxygen concentration at the tip surface was tied up in a passivating oxide layer ~ 50 - 100 Å thick (Figure 3.23).

This data alone rules out the formation of a radiation resistant compound via a gas phase – liquid Si interaction during melting of the Si wafer because only Si is present in the microcolumn tip. Even so, possible compounds that could form in air during irradiation, such as Si_3N_4, SiO_2, and SiO_x, are less stable than Si under pulsed excimer laser irradiation.

For example, SiO_2 etches in response to pulsed excimer laser radiation at a rate of 23 nm/pulse/J/cm^2 and SiO_x at a rate of 6 600 nm/pulse/J/cm^2. [61, 62] Pedraza et al. found high purity, synthetic fused SiO_2 to etch at a rate of 25 nm/pulse/J/cm^2 in air using a fluence of 3.0 J/cm^2. [63] An etch rate of 0.8 nm/pulse/J/cm^2 was determined in this work (Figure 3.36) for Si (100) etched with a fluence of 3.0 J/cm^2 in air. Miyamoto and Maruo found Si to be the radiation resistant component responsible for cone formation during excimer laser irradiation of a Si_3N_4 target (Figure 1.4). [16] Consequently, radiation hardening is not the active mechanism responsible for the evolution and growth of the Si microcolumn morphology.

4.2 Hydrodynamic Processes

Two hydrodynamic processes will be considered as possibly responsible for the formation of the Si microcone/microcolumn laser-induced morphology. Hydrodynamic

sputtering, as proposed by Rothenburg and Kelly and described in detail in section 1.4.3, explains the growth of the cones by the expulsion of a preexisting surface asperity away from the target surface. The hydrodynamic effects in this model are driven by the laser pulse, which generates high temperature, melted asperities. The expulsion occurs by the flow of liquid Si, i.e., the asperity, and is resisted by the inherent surface tension of the liquid.

Hydrodynamic processes as driven by non-uniform heating of the liquid Si will also be investigated. Non-uniform heating can result from using a laser pulse with an inhomogeneous energy beam profile. In this case, liquid Si will flow from the hot regions of the laser irradiated surface to the cold regions. The result is a previously atomically flat surface being made rough following laser annealing. The fundamental difference between the two hydrodynamic processes is that one causes a further roughening of an already rough surface whilst the other forms a rough surface from a previously smooth one.

4.2.1 Hydrodynamic Sputtering

The morphology of the microcolumns observed after cumulative laser irradiation of Si in air does not coincide with the morphology predicted by the hydrodynamic sputtering model. In contrast to the melted asperity shown in Figure 1.13, Si microcolumns attain such heights that the entire microcolumn body can no longer be melted with each laser pulse. Therefore, the melted column tip has no connection to the liquid pool at the column's base. A schematic representation of the disconnected melt pool is shown in Figure 4.1.

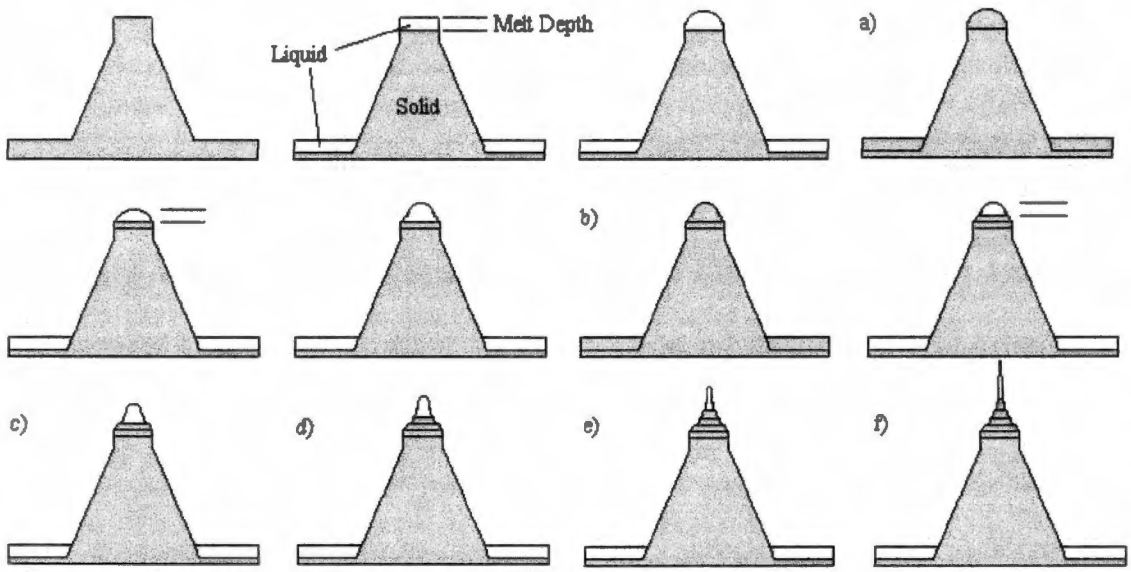

Figure 4.1 A schematic representation of the hydrodynamic sputtering process when the surface asperity height (6 – 8 μm) is greater than the melt depth (~ 900 nm). The conical asperity at top-left was formed with several hundred pulses of 248 nm laser radiation. E_d = 3.0 J/cm^2. The top row shows the morphology change at the cone tip resulting from one laser pulse. The asperity grows vertically and contracts laterally on sequential irradiation of the cone. Schematics a) – f).

The top row of Figure 4.1 shows the change in morphology of a preexisting surface cone following one laser pulse. The preexisting cone resembles the base of the microcolumn shown in Figure 3.44. The conical base is ~ 6 – 8 μm tall in the figure. Thus, the schematic in Figure 4.1 is a simulation of Si microcolumn growth after several hundred laser pulses have already been applied to the Si wafer. The melt depth from each laser pulse is only ~ 900 nm for a fluence of 3.0 J/cm^2 and a laser wavelength of 193 nm. Only the very top of the cone and surrounding wafer floor will melt because of the shallow melt penetration depth.

The cone sides will also melt during each pulse but to a much shallower depth because of fluence dilution. The steep angle of the cone's sides dilutes the fluence since the incident radiation is illuminating a much larger area. At first, the assumption made here that no melt connection between the top and bottom may seem inappropriate since the sides of the cone are melted. However, again looking at Figure 3.44, the columns eventually have vertical sides and the assumption of no melt connection becomes valid.

The far-left schematic in Figure 4.1 shows the solid, conical Si structure. Moving left-to-right, the next schematic shows the effect of the laser pulse. Both the top of the cone and the material surrounding the cone have been melted. Surface tension effects cause the melted portions to minimize their surface area (No movement of the liquid at the bottom of the pit is shown because it is irrelevant to the argument being made). Finally, and shown in a), the melted regions resolidify.

The problem now arises that no source of silicon is present to produce the *constant diameter* Si microcolumn growth observed in our results. For example, microcolumns of various height and constant diameter are shown in Figure 3.45. Returning to the

illustration in Figure 4.1, the remaining schematics show the morphology that will result in response to cumulative laser irradiation for a hydrodynamic sputtering process.

The fluence is constant for each laser pulse ensuring the melted depth of Si is constant as well. However, the amount of Si melted with each pulse at the tip will slowly decrease. The amount of material melted with each pulse decreases due to the asperity moving away from the initial wafer surface with each pulse *at constant volume*. To maintain constant volume during expansion requires the asperity to get thinner with each laser pulse. As the asperity becomes thinner the amount of melted Si decreases under constant fluence conditions.

The first schematic in the middle row of Figure 4.1 shows the material melted after the second pulse. The melt depth is unchanged and shown by the dimension lines adjacent to the drawing. The hydrodynamic expulsion process again operates and the asperity at the tip of the cone moves further from the surface.

Cumulative laser irradiation produces a high-aspect ratio needle since no additional silicon is available to the tip from the surrounding melt pools to maintain a constant tip diameter during the expansion. In other words, the hydrodynamic sputtering process must occur at *constant volume* if applied to the formation of Si microcolumns. Hydrodynamic sputtering is not the mechanism responsible for the growth of the microcolumn shown in Figure 3.44 because the microcolumn has a constant diameter over ~ 25 – 30 μm of its length.

The problem in applying the hydrodynamic sputtering model to Si is that Si contracts on melting. [64] The density of liquid silicon, 2.52 g/cm^3, is greater than the density of solid silicon which is 2.32 g/cm^3. [29] The linear thermal expansion of liquid Si is 0.038

but the linear expansion due to melting is – 0.032. Consequently, the expansion of the liquid from the temperature rise to ~ 2 700 K is compensated for by the contraction when solid Si transforms to liquid Si.

Moreover, the background gas present during irradiation should not have such a dramatic effect on morphology, as is observed, if the growth mechanism were indeed asperity expulsion. For example, it is hard to imagine a hydrodynamically controlled process producing the drastic difference in cone morphology observed after irradiation in air (Figure 3.11) and SF_6 (Figure 3.25). In addition, irradiation in He does not produce the columnar surface structure. Instead, a periodic surface structure (PSS) is observed.

4.2.2 Non-Uniform Surface Heating

Several examples of liquid surface flow, which was frozen in motion when the solid – liquid interface retreated to the surface, were found on the laser-irradiated Si surface. Extensive melting of the Si surface irradiated in air is shown in Figure 3.2. Melting features such as ripples and smooth undulations lie adjacent to the surface fractures as shown in the photomicrograph in Figure 3.2. Similar melting features on the surface of Si irradiated in air are shown in Figures 3.3, 3.4, 3.8, 3.13, and 3.20.

Examples of liquid Si flow were also found on the surface of Si laser irradiated in SF_6. Figure 3.29 shows concentric waves of Si surrounding a surface etch pit. Evidence of the movement of the lateral cones along their parent microcones, induced by cumulative irradiation in SF_6, is shown in Figure 3.33. A dense concentration of etch pits on the laser-modified Si surface is shown in Figure 3.31. Ripples are seen on the sides of the surface ridges which form a circle around one of the etch pits.

Again examining Figure 3.2, it appears the flow of Si on the surface is responsible for the formation of the surface ridges. For instance, liquid Si appears to flow away from the surface fractured regions. The liquid collects in mounds adjacent to the surface fractures forming the surface ridges. The fracturing is more extensive in Figure 3.3, compared with Figure 3.2, resulting in the formation of a greater number of surface ridges.

It is not clear why the flow of liquid Si occurs on the laser-irradiated wafer surface. The liquid flow does appear to be localized to the regions of prominent surface damage. In addition to the liquid flow around the surface fractures described above, much flow occurred around the etch pits formed by laser-irradiation in SF_6. The etch pit indicated by the arrows the Figure 3.31 clearly shows substantial melt flow around its perimeter.

Two processes could be responsible for the flow of liquid Si on the laser melted and dry-etched Si wafer surface. Non-uniform heating of the surface in and around the etch pits and surface fractures could provide the driving force for the flow of liquid Si. Impurity segregation in the liquid phase can also launch liquid flow. Segregated impurities effectively decrease the surface tension in the segregated area, which in turn, initiates the flow of liquid to surrounding regions of higher surface tension.

Impurity segregation of oxygen in pulsed-laser melted iron has been reported by Balabin et al. to balance surface tension gradients in melted iron. [65] They found that laser-induced oxygen segregation, which occurred 75 ns after irradiation, later balanced the flow of liquid Fe to the segregated regions. The oxygen segregated to the colder regions of the laser spot. [65] The flow of liquid Fe from the hotter regions to the segregated regions was reduced by the presence of the oxygen impurities. Thus, oxygen segregation reduced the surface tension gradient, the driving force for liquid flow, by

effectively decreasing the surface tension in the segregated regions. [65] The surface tension gradient across the laser spot was reduced to zero 600 ns after the laser pulse heated the thin iron film.

Impurity segregation applied to the observed flow in liquid Si would require impurities to segregate at the edges of the surface fractures and etch pits. Segregation at the edges would ensure flow away from this location. Similarly, if non-uniform heating is the culprit, the edges of the surface fractures must be the hotter regions of the laser-irradiated surface. Figure 4.2 shows a schematic cross-section of a surface fracture showing a possible liquid flow scheme to describe the observed surface morphology of laser-irradiated Si. The schematic resembles the way liquid Si has moved away from the surface fractures shown in Figure 3.2.

Whether the surface flow of liquid Si is attributable to impurity segregation or non-uniform heating is unclear at this point. Further surface characterization, such as Auger depth profiling and EDS, would provide a means to test for impurity segregation on and under the Si surface. A more complicated experimental arrangement, such as simultaneous TEM and laser irradiation, would be required to monitor time-resolved liquid surface flow. [65]

Several other observed surface morphologies related to the flow of liquid Si are worth mentioning here. Surface tension effects in the liquid Si were responsible for the "onion-dome" appearance of the spherical tip at the end of each microcone/microcolumn. [66] The "onion-dome" morphology is best observed on the Si microcolumn shown in Figure 3.38. Figure 3.14 shows a high-resolution photomicrograph of the same "onion-dome" morphology atop a Si microcone.

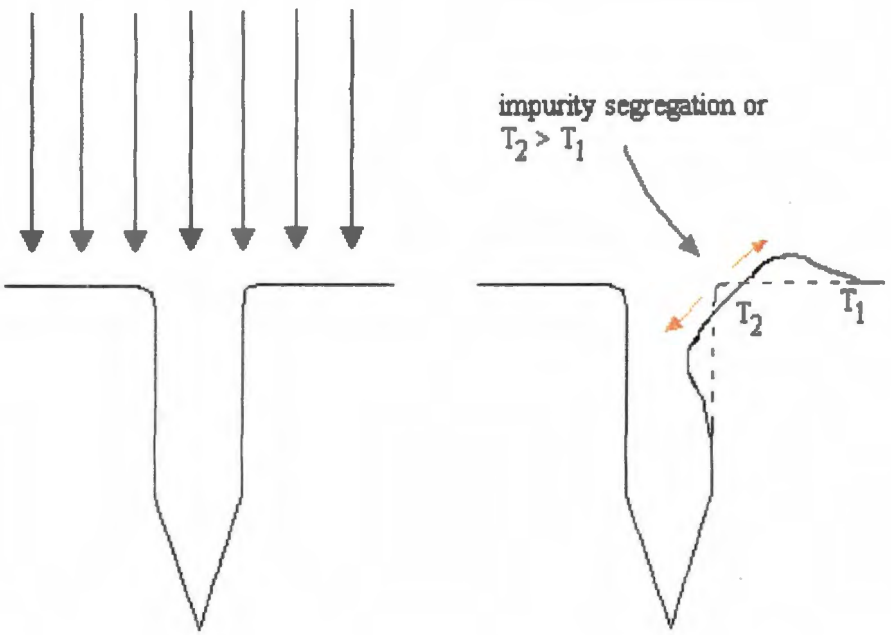

Figure 4.2 A schematic demonstration of liquid Si flowing via a surface tension gradient that has formed as a result of an excimer laser pulse. a) Incoming laser irradiation on a preexisting surface fracture (view in cross-section). b) Liquid Si has been observed to flow away from the surface fractures (Figure 3.2). Two possible explanations are that 1) the edges of the fractures are hotter than the surrounding liquid Si or 2) oxygen impurities segregate at the edges of the surface fractures. Both of these phenomena will tend to decrease the surface tension at the fracture edge causing the flow of liquid Si into the surrounding cooler, or non-contaminated, regions.

A description of the morphology shown in Figure 3.14 was provided in section 3.1.1. Figure 4.3 shows a schematic illustration of the resolidification process of a microcone/microcolumn tip following one pulse of KrF laser irradiation. The schematic progression illustrates how the concentric ring morphology develops at the tip of each "onion-dome" shaped microcolumn/microcone tip.

The portion of the microcone/microcolumn melted with each pulse is the spherical cap that resides atop each such structure. The drop will attempt to minimize its surface area while in the liquid state forming a cap atop the underlying solid Si. As the cap solidifies, the temperature of the infinitesimal liquid slab (Figure 4.3) above the solid-liquid interface will remain constant. Since the contact angle of the liquid drop is a function of temperature, the contact angle will remain constant. A constant contact angle throughout the resolidification process will produce a conical tip (Figures 3.38). Thus, the liquid ball atop each column/cone will have the appearance of an "onion-dome", following resolidification, as shown in Figure 4.3.

Two different surface ridge morphologies have been observed on laser irradiated Si, in both SF_6 and air, depending on the location of the surface ridges inside the laser spot. The surface ridges that have been shown and discussed to this point all originated in their respective laser spot centers (such as those shown in Figures 3.2, 3.3, and 3.31).

The surface ridges originating inside the laser spot, but closer to the edges of spot, are shown in Figure 3.8. The exact location of the area shown in the photomicrograph in Figure 3.8 was ~ 0.5 mm from the laser spot edge. The surface ridges have evolved here *independent* of the etch pits and surface fractures.

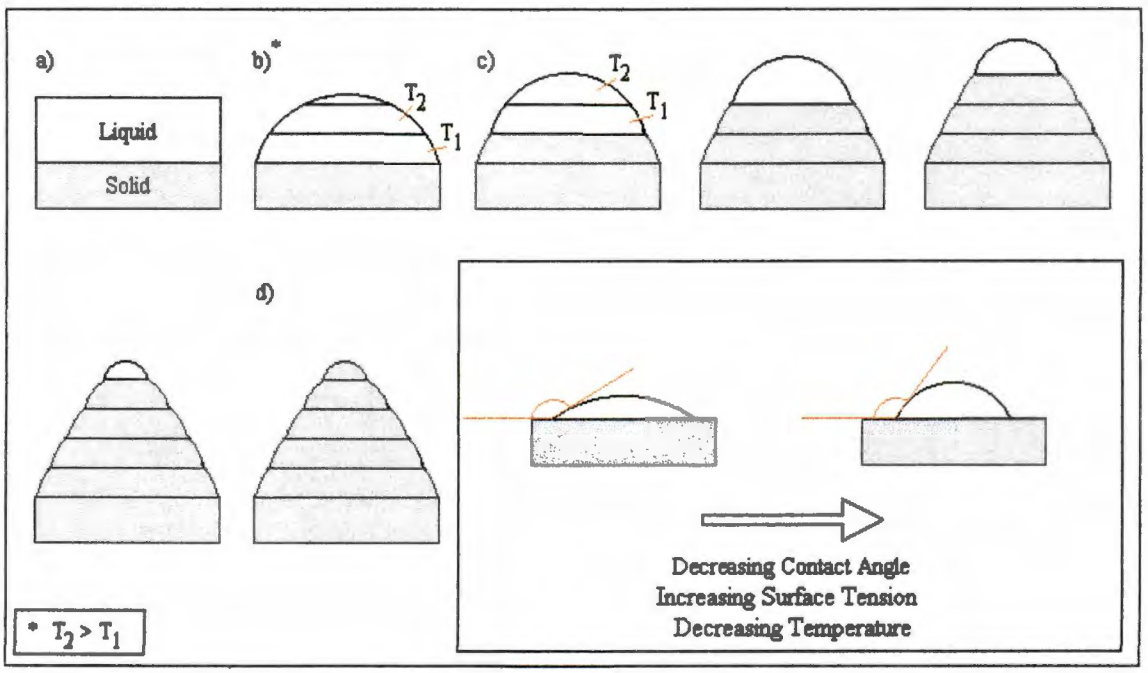

Figure 4.3 The above schematic aids in understanding the "onion-dome" morphology of the tip that resides atop each Si microcone/microcolumn. a) the material atop each microcone/micrcolumn is melted to some maximum depth with each laser pulse. b) the liquid Si wets the underlying solid Si at a specific contact angle. c) The solid-liquid interface retreats to the surface. An infinitesimal slab of liquid resolidifies and the next slab to resolidify must wet the underlying Si at the same contact angle. This is because the slab above the solid-liquid interface in each of the schematics is at the same temperature T_1. The contact angle is a function of temperature. The process continues until the tip resolidifies completely. d) The result is more conical tip than spherical as shown in Figure 3.38. The inset in the figure above shows the relation between surface tension and the contact angle.

It is interesting to note that the morphology shown in Figure 3.8 is located in an area in the laser spot that received a lower fluence than the center of the laser beam.[1] In fact, this same morphology is found at the *center* of a Si wafer irradiated in air at a fluence lower than that conducive to Si microcolumn growth, namely 2.7 J/cm^2 (Figure 3.20). Surface fractures and etch pits *are not produced* on the surface of Si wafer irradiated with an energy density of 2.7 J/cm^2. Moreover, 1 000 laser pulses, each with a fluence of 2.7 J/cm^2, has yet to produce a single microcolumn on the Si surface (Figure 3.20). Using an irradiation fluence of 3.3 J/cm^2, microcolumns ~ 20 μm high can be produced in 250 laser pulses (Figure 3.13). Thus, it appears that surface ridges can form independently of surface fractures and etch pits. However, the growth rate of the ridges, and hence the columns, is greatly reduced when surface fractures and etch pits are not present on the surface. Stated differently, the etch pits and surface fractures act to accelerate the growth rate of Si microcones/microcolumns.

The surface ridge morphology illustrated in Figure 3.8 has been observed on the surface of laser irradiated, 99.5% pure iron. [67] A Nd:YAG laser operating at a wavelength of 1.06 μm was used to melt an iron target. Dauscher et al. used a laser fluence of 1 J/cm^2 during their experiments and irradiated the iron in an atmosphere of air [67] The size, shape, and distribution of the surface ridges produced on the iron surface are very similar to those produced on the surface of laser etched Si. (Figure 3.8)

[1] The laser beam energy profile is reflected in the smooth, etched laser spot shown in the top-left Si surface profile in Figure 3.28. The laser spot resembles an inverted trapezoid. The area shown in Figure 3.8 corresponds to a location in the energy beam profile where the fluence falls off rapidly, approaching the edge of the laser spot.

Non-uniform surface heating that occurred during melting is responsible for producing the same morphology in both pure Fe and single-crystal Si in response to laser surface melting. This is the only plausible explanation considering the same morphology was obtained in two different materials with irradiation at two different laser wavelengths. Diffraction effects seem not to be responsible for the formation of the surface ridge morphology because the surface ridge spacing is independent of the laser wavelength. [68]

4.3 Si Transport via the Vapor Phase and Deposition at the Liquid Microcone/Microcolumn Tips

The Si microcones and microcolumns grow in length above the initial wafer surface as the number of laser pulses increases. Si must therefore be *transported* during each pulse from the depressions in the laser-etched spot to the cone/column elevations to account for such growth above the initial wafer surface. It has been shown that the motion of Si in the liquid state promotes the formation of surface ridges. However, this motion alone can not account for the tall, high-aspect ratio cones and columns observed on the surface (Figures 3.26 and 3.44).

Section 4.2.1 showed that hydrodynamic sputtering was incapable of producing the observed Si microcolumn morphology due to a disconnection between the liquid Si at the tips of the columns and the liquid at their bases. A liquid sink is required during hydrodynamic sputtering to provide the material necessary for expansion away from the target surface during each laser pulse. For the microcolumns to grow by hydrodynamic sputtering would require the columns to become thinner as they get taller because the

expansion away from the surface must occur at constant volume from the liquid Si "trapped" atop the column tip. The microcolumns were observed to grow in height at constant diameter.

Non-uniform heating effects were attributed to the formation of surface ridges on the laser melted Si surface. However, non-uniform heating cannot account for the tall, cylindrical microcolumns produced because, as was the case with hydrodynamic sputtering, no liquid connection exists between the column tips and bases. Non-uniform heating would require a liquid connection between the tips and bases of the columns to transport liquid via thermocapillarity effects. Liquid motion is thus not responsible for the growth of the Si microcones/microcolumns above the Si wafer surface.

Surface melting is observed at number of pulses as low as ~ 10 when Si is irradiated in air. However, an incubation period is required before the growth of microcones and microcolumns ensues. The incubation period for growth in air was in a range of ~ 200 – 300 laser pulses using a laser energy density of 3 J/cm^2. In SF_6, for the same fluence, an incubation of ~ 1 000 laser pulses was required before microcone growth ensued.

The end of this incubation period corresponds to the beginning of formation of surface fractures and etch pits (air) and etch pits (SF_6). Surface ridges form adjacent to this etching damage 100 laser pulses after the damage is observed on the surface. Microcone/microcolumn growth develops rapidly following the formation of the etching damage.

The microcones/microcolumns grow by deposition of Si at their tips via a Si containing molecules from the vapor phase. The intense flux of material that emerges from the wafer during irradiation is mirrored in the ring of material surrounding the laser

spot (Figures 3.17 & 3.18) as well as the bright, blue – white plume observed during each pulse. The splashing effect of redeposited material striking the liquid Si surface is shown in Figure 3.19. The method by which Si deposits at the liquid cone/column tips is similar to the VLS deposition process (section 1.5) used to grow high-aspect ratio single crystal Si whiskers.

The difference in the VLS mechanism used to growth Si whiskers and the "VLS-like" process proposed here is that no eutectic phase is required for the deposition of Si to occur. The VLS mechanism operating here is "catalyst-free", *the laser simultaneously produces the liquid phase necessary for Si molecule adsorption and deposition and the intense flux of Si required to saturate the liquid drop.* During the VLS whisker growth process Si containing molecules are *externally* introduced into a CVD chamber for deposition at a $(Au - Si)_{liquid}$ interface. The (Au – Si) eutectic is formed by *resistively heating* a Si substrate which contains a thin gold film on the surface. Temperatures sufficient to melt the gold film are applied to the substrate and diffusion of Si across the Au(l) – Si(s) interface ensures formation of the eutectic.

Following the formation of surface fractures and etch pits, each laser pulse etches the Si surface, and SiF_2 and SiO desorb into the vapor phase. The formation of SiF_2 and SiO in the presence of SF_6 and O respectively is analyzed in section 4.5. In section 4.4 it is shown that the flux of SiF_2 and SiO is more intense from the etch pits and surface fractures. Moreover, it is adjacent to these features that the microcones and microcolumns form. Thus, the laser is responsible for forming Si containing molecules that eventually populate the gas phase. This is in contrast to the VLS whisker growth process where Si containing molecules are flowed into the deposition chamber externally.

The SiF_2 and SiO emerging from the surface adsorb on the liquid Si atop the surface ridges. A liquid can be thought of as a surface of infinite steps and ledges. The accommodation coefficient of the liquid phase is ~ 1 meaning that most all of the atoms and molecules that come in contact with this surface adsorbs on the liquid and incorporates into the liquid drop. Embodied in the accommodation coefficient is the probability an atom will adsorb on the liquid surface as well as the probability it will incorporate into the liquid. In the VLS whisker growth process the liquid eutectic, e.g., Au – Si, is melted on a single crystal, Si substrate by heating the substrate. The externally introduced Si molecules, e.g., $SiCl_4(g)$, dissociate at the accommodating liquid eutectic surface.

The mean free path of a neutral Si atom was calculated to determine if sufficient collisions occur between the ejected species and the plasma plume to backscatter Si neutrals. The backscattered neutrals can then participate in microcolumn growth by depositing at the microcolumn tips. For instance, a mean free path on the order of ~ 10 μm would ensure many collisions of the Si neutrals before they reach a height above the wafer surface equal to the top of the microcolumn structures. The Knudsun equation was first used, assuming equilibrium conditions, to determine the pressure of Si vapor in the plume required to produce the observed growth rate of the Si microcolumns.

Between 400 and 600 laser pulses, Si microcolumns were observed to grow at a rate of 70 nm/pulse. Assuming a deposition area of $\pi(2.5\ \mu m)^2$, the volume of material deposited per pulse in 19.63 μm^2 x 70 nm, or $1.37 \times 10^{-18}\ m^3$. The atomic density of Si is 5×10^{28} atoms/m^3, thus 7×10^{10} Si atoms are deposited during each laser pulse epitaxially on the Si (100) plane.

The Knuden equation gives the flux of impinging molecules J as: [70]

$$J\ (\text{atoms/cm}^2\ \text{s}) = \alpha N_a \Delta p / (2\pi MRT)^{1/2}$$

Where $\Delta p = p - p_o$; p is the actual vapor pressure and p_o is the equilibrium vapor pressure. The temperature used in the calculation was 2 400 K. This temperature is an average of the melting temperature 1 687 K and the estimated maximum melting temperature during irradiation, ~ 3 000 K. [12] Hanabusa et al. found the emission of neutral Si to occur for ~ 50 ns following a 10 ns Nd-YAG 1 J/cm^2 laser pulse. [34]

Every molecule that impinged on the liquid tip surface was assumed to be absorbed because the accommodation coefficient (α) of the liquid phase is ~ 1. It was calculated that a pressure of 70 atm above p_o was necessary to produce the required flux of 7×10^{10} atoms / (19.63 μm^2 x 50 ns) = 7×10^{28} atoms/m^2 s.

For laser light intensities I > 10^8 W/cm^2 and irradiation in air, the pressure behind the propagating plasma front can be as high as 10^3 atm. [8] The calculated pressure of 70 atm is far less than 10^3 atm implying that the Si vapor pressure is not a limiting factor for the observed growth rate of the microcolumns.

The mean free path of laser-etched Si neutrals was calculated using the kinetic-molecular model of an ideal gas and the Δp value calculated above. A Si neutral ejected during ablation has a velocity of $1.3 \pm 0.2 \times 10^6$ cm/s when a Si target is irradiated with 248 nm radiation of fluence 1 J/cm^2. [34] An atomic radius of 1.2 Å was assumed for the ejected Si vapor species and a pressure of 70 atm was assumed above the Si wafer surface.

The mean free path using the kinetic-molecular model for an ideal gas is given as: [31]

$$\lambda = kT / 4\pi(2)^{1/2} r^2 p$$

r being the radius of the molecule and p is the ambient pressure. A mean free path of 2 μm was calculated for a Si neutral traveling at $1.3x10^6$ cm/s. For irradiation of Si (100) wafer in air with 3.0 J/cm^2 the distance to transport Si from the pits and fractures bottoms to the column tips is ~ 40 – 60 μm.

The mean free path of the Si neutrals is ~ 20 – 30 x less than the average microcolumn height. The shorter the mean free path the greater the chance a Si_I will be backscattered toward the Si target because the number of scattering events increases as the number of collisions increases. Thus, the kinetic-molecular model indicates that sufficient collisions of Si neutrals occur within the plasma plume to backscatter Si for deposition at the microcolumn tips.

Once SiF_2 and SiO is adsorbed on the liquid, dissociation occurs by the following reactions [58, 69]

$$2SiF_2(g) \rightarrow SiF_4(g) + Si(s)$$

$$2SiO(g) \rightarrow O_2(g) + 2Si(s)$$
or
$$2SiO(g) \rightarrow SiO_2(g) + Si(s)$$

The supersaturation of the liquid Si drop with Si by these reactions will induce deposition of Si at the $Si_{solid} – (Au – Si)_{liquid}$ interface resulting in the surface ridge rising above the Si wafer surface becoming a cone or column.

Growth via vapor phase deposition tends to produce high-aspect ratio needles or whiskers. Figure 1.28 shows high-aspect, VLS whiskers grown by Givargizov and co-workers. Several similarities in morphology exist between Givargizov's whiskers and the microcolumns fabricated by KrF laser irradiation in air.

Periodical changes in diameter are seen in whiskers of diameter < 0.50 μm grown by the VLS process. Similar instabilities in diameter were found in Si microcolumns grown in an atmosphere of 20% O_2 – Ar (Figure 3.44), 5% O_2 – N_2 (Figure 3.43a), and air (Figure 3.38). The reason for the formation of the instabilities is the VLS process is unclear. [44]

Each whisker shown in Figure 1.28 resides atop an undulation of larger diameter. Moreover, the wider whiskers in the figure are conical at their bases and become cylindrical ~ 1 μm above the substrate floor. These morphological features are very similar to the features of the laser grown microcolumn shown in Figure 3.44. Based on morphological characteristics alone, the microcones and microcolumns appear to grow over most of their length from the vapor phase.

Another microcolumn with periodic changes in diameter is shown in Figure 3.38. Irradiating Si (100) wafer in air with 750 laser pulses produced the microcolumn shown in Figure 3.38. This photomicrograph was taken of one of two Si wafers, both irradiated with the same fluence and number of pulses. The second wafer received an additional 100 laser pulses in an atmosphere of 100% O_2.

The surface morphology after the 100 additional pulses in O_2 is illustrated in Figure 3.39. The second irradiation wrapped a microcolumn, similar to the one shown in Figure 3.38, in a sleeve of material. The sleeve charged under the focused electron beam of the SEM suggesting it contains a substantial amount of oxide. The figure clearly indicates deposition from the vapor phase is a strong contributor to Si microcolumn growth. Moreover, the oxide concentration in the sleeve supports the idea of a SiO species transporting Si in the vapor.

To prove that the microcones/microcolumns grew by vapor deposition at the tip, the background gas was changed during irradiation from SF_6 to air (Figure 3.40) Microcones, similar in morphology to those shown in Figure 3.26, were grown in an ambient of SF_6 with 2 000 laser pulses. Further irradiation in 5% $O_2 - N_2$ with 500 laser pulses *initiated the growth of the microcolumn morphology at the tip of the Si microcone.* The step of morphology change is shown in Figure 3.42.

A "fractal-like" growth along the microcolumn/microcone sides was deposited on the sides of the microcones after the background gas switch was made. Dickinson et al. observed the same growth on the sides of a Ge cone that was grown in an atmosphere containing oxygen (Figure 1.9). [23] They reported the "fuzz" surrounding their Ge cones to be small GeO particles. The "fuzz" shown in Figure 3.42 is most likely SiO_x since the growth is not observed when microcones are grown in SF_6 only.

4.4 The Si Vapor Flux Produced in SF_6 and Air

The flux of Si[2] emerging from the wafer surface is greatly enhanced when laser irradiation is performed in the presence of SF_6 or air (Figure 3.36). The etch depth per pulse in air is 25x greater than the etch depth per pulse in He. Similarly, the etch depth per pulse in SF_6 is 12x greater than the etch depth per pulse in He. However, the data presented in Figure 3.36 *understates* the etched flux emerging from both air and SF_6! Figure 3.30 shows the reason why the etch depth per pulse is underestimated.

The etch depth per pulse data reported in Figure 3.36 were determined by measuring the depth at the center of the laser spot with respect to the initial wafer surface. For

[2] The term "Si flux" embodies Si atoms, ions, and molecules containing Si.

example, the profilometry plot shown in Figure 3.30 was read as 0.4 μm of Si being removed in response to 300 KrF pulses in 1 atm SF_6. Closer inspection of the figure shows a sharp spike penetrating deeper into the Si at the center of the laser-irradiated area.

The sharp spike shown in the profile coincides with the location of a surface etch pit in the Si wafer. Thus, the Si flux emerging from the etch pits and surface fractures in the Si wafer surface is much greater than the flux produced from the uniform etching of the entire laser irradiated area.

As shown in Figure 4.4 the etching of the irradiated area in SF_6 is more uniform and deeper than that produced in He under the same irradiation conditions. Also, etch pits are not produced when laser irradiation is carried out in He. Therefore, it appears that a laser-induced chemical reaction is responsible for the observed enhancement in etching. The exact progression of the photochemical etching sequence in both air and SF_6 is not fully understood.

4.5 Laser – Induced Etching of Si

4.5.1 Etching in SF_6

SF_6 dissociates in response to 248 nm laser light forming fluorine. The odor of F_2 gas was present upon opening of the vacuum chamber following laser irradiation of Si wafer in SF_6. The UV photon energy is sufficient to excite and dissociate SF_6 because this molecule dissociatively chemisorbs on Si following vibrational excitation in the IR. [8]

The dissociation products of SF_6^* are listed in section 1.6 of the Literature Review. The fluorine ions, $2F^-$, produced from the dissociation, penetrate into the Si surface

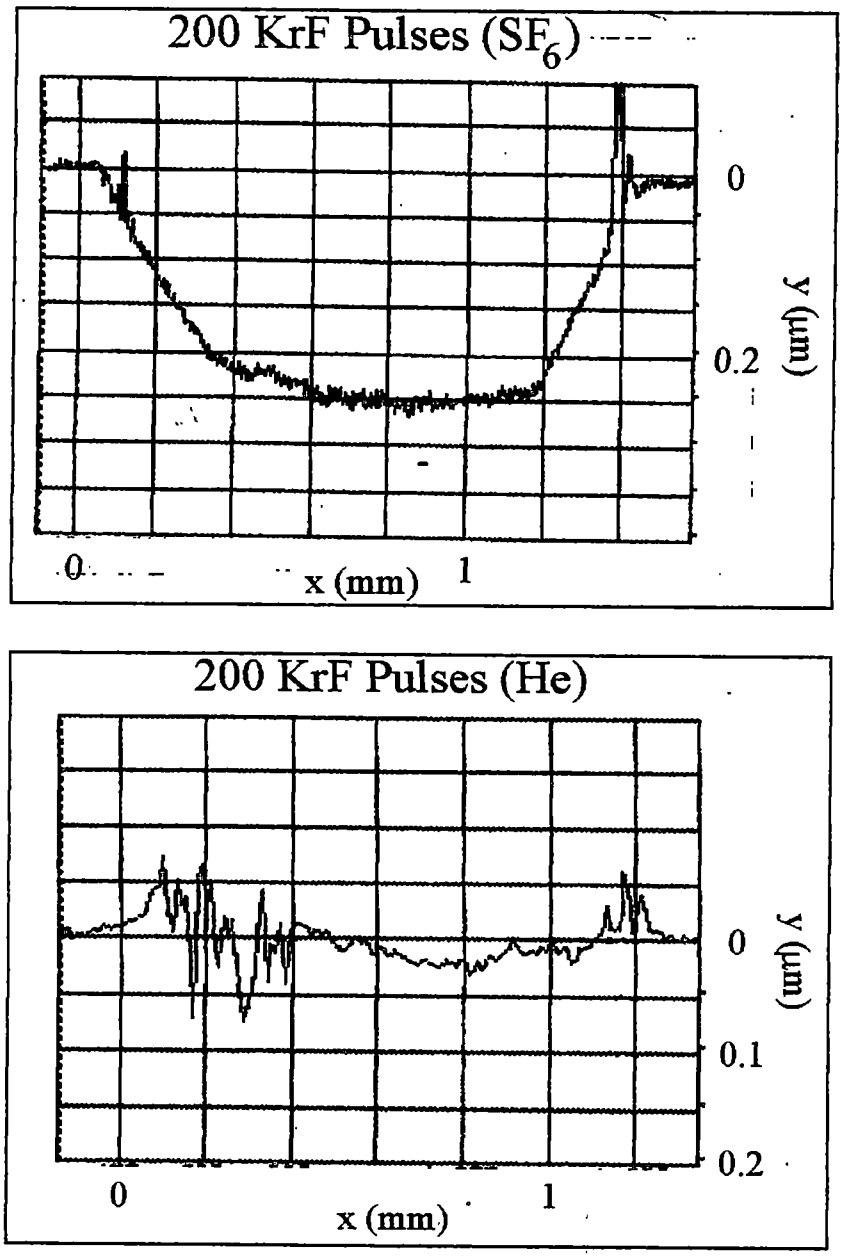

Figure 4.4 The groove produced in Si (100) wafer from laser irradiation in SF_6 is more uniform and deep than the groove produced from laser irradiation in He. E_d = 2.9 J/cm^2, PRR = 3 Hz, and BG = 1 atm.

forming a fluorosilyl layer ~ 10 – 30 Å thick. [8, 53 – 56] The layer is reported in literature to contain mostly SiF_3. [8] $SiF_x(g)$ desorbs from the fluorosilyl layer, the primary etch product above T = 800 K being $SiF_2(g)$.

An abundant amount of literature exists documenting $SiF_2(g)$ as the primary etch product from Si at high temperature. [71 – 73] It is well documented that $SiF_2(g)$ is the major desorption product from the Si surface. For instance [73]

$$F(g) + Si(surface) - F(chemisorbed) \rightarrow SiF_2(absorbed)$$

$$SiF_2(absorbed) \rightarrow SiF_2(g).$$

4.6 The High Temperature Etching of Si by O_2 Gas

Section 1.6.3 described experiments conducted by Ohkubo et al. to determine the vapor species produced following the etching of Si (100) and (111) wafer at high temperatures with a pulsed O_2 beam. They found SiO(g) to be the major desorption product etched from Si at T > 1 000 K. [57] The etching of Si by O_2 has also been described in the literature by Nakamura et al. [58] They proposed the surface reaction

$$O_2(g) + 2Si(s) \rightarrow 2SiO(g)$$

as responsible for the production of the SiO(g).

4.7 The Geometry of the Si Surface Etch Pits

The side-walls of the etch pits in air are steep and conical as shown in Figure 3.16. The etch pits produced by KrF irradiation in SF_6 have even steeper side-walls making them almost cylindrical pits (Figure 3.31). Due to the geometry of these pits, radiation is

almost completely absorbed within the pit. In contrast, radiation that strikes the flat portions of the irradiated area will be partly reflected.

The probability that a SF_6 molecule will be excited adjacent to the Si surface is increased by multiple reflections in the etch pits. Each additional reflection on the Si surface increases the probability that the photon will be absorbed by an SF_6 molecule and contribute to the photochemical laser etching process. Figure 4.5 shows a schematic illustration of the improved efficiency of the photochemical etching process by multiple reflections.

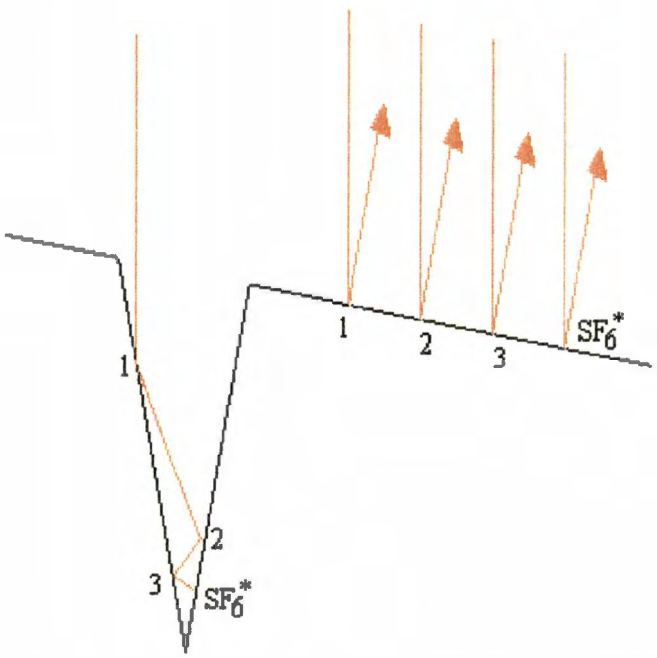

Figure 4.5 The probability of exciting an SF_6 molecule is increased by multiple reflections that occur in the KrF – SF_6 induced etch pits. Assuming a 25% excitation efficiency of SF_6 by 248 nm laser light, the absorption efficiency of SF_6 will increase by at least 4x in the surface etch pits.

Chapter 5

Conclusions

1. Si microcolumns were produced on the surface of Si (100) and Si (111) wafers by KrF (248 nm) pulsed-laser irradiation in 1 atm, air.

2. Si microcones were produced on the surface of Si (100) wafers by KrF (248 nm) pulsed-laser irradiation in 1 atm, SF_6.

3. Using energy dispersive spectroscopy (EDS) and Auger depth profiling the Si microcolumns were found to contain Si in the bulk with a small concentration of oxygen located at the surface to a depth of ~ 10^3 Å under the surface. The oxygen concentration decreased linearly from the surface to 10^3 Å inside the bulk.

4. The Si microcolumn morphology grew only in the laser pulse fluence range 2.7 – 3.6 J/cm^2. The growth initiated anywhere between 200 – 300 laser pulses depending on the fluence used in the above range. The higher the fluence the fewer the number of laser pulses required to initiate growth. The microcolumns saturated in height and density between 1 000 – 1 200 laser pulses. Each columnar microcolumn saturated in height at ~ 30 – 35 μm with diameters of ~ 2 – 3 μm. Situated atop each microcolumn was a 2 – 3 μm spherical tip.

5. The Si microcone morphology developed over the entire fluence range tested, 0.9 - 3.8 J/cm^2. The growth of the microcones initiated after ~ 1 000 laser pulses using a laser fluence of 2.9 J/cm^2. The microcones protrude above the initial Si (100) wafer surface by as much as 40 μm. Each Si microcone had a 2 – 3 μm spherical tip at its vertical termination.

6. Both the microcolumn and microcone morphologies could be grown above their initial Si wafer surfaces provided sufficient numbers of laser pulses were applied to each target.

7. The Si microcone/microcolumn morphology did not develop when the pulsed-laser irradiation of Si was performed in Ar, N_2, 5% H_2 – Ar, and He up to 3 000 laser pulses.

8. The amount of Si sputtered per pulse was increased when pulsed-laser irradiation was carried out in SF_6 or air. This result was attributed to laser-induced etching of the Si surface. F_2, formed in the gas phase by electronic excitation and dissociation of SF_6, was responsible for etching Si. O_2 was found to etch both Si (100) and (111) wafer. F_2 was found to etch Si (100) at a rate of 12 Å/pulse whilst O_2 etched Si (100) at a rate of 25 Å/pulse up to ~ 500 laser pulses. Similar experiments conducted in He found Si to desorb at a much slower rate of 1 Å/pulse.

9. Si microcolumns and microcones grew in height as the number of laser pulses was increased. An incubation period was required before growth ensued in both the SF_6 and air background gases. Approximately 200 – 300 laser pulses in air and 750 – 1 000 pulses in SF_6 were required before the microcolumn/microcone morphology developed on the Si surface.

10. Surface ridges populate the surface of Si irradiated with low numbers pulses in SF_6 and air. The surface ridges form just prior to the growth of Si microcones/microcolumns and the morphology of these ridges is the same in both gases. The ridges form in air at number of pulses greater than ~ 200. The ridges appear on the Si surface at numbers of pulses greater than ~ 750 when irradiation is performed in SF_6. Each ridge grows into a microcone/microcolumn with ~ 50 – 100 additional laser pulses.

11. The surface ridge morphology appears to form by the flow of liquid Si during the ~ 200 – 300 ns the surface is melted after each pulse. The surface ridges evolve preferentially adjacent to the primary surface damage. Surface fractures and etch pits are the prominent surface damage present following pulsed-laser treatment in air. Etch pits are the primary damage present on laser-modified Si wafer in SF_6.

12. The surface fractures and etch pits penetrate far deeper into the Si surface than does the overall, rectangular laser groove. Scanning profilometry indicated the fractures and pits penetrate as much as twice the overall laser spot depth into the Si

surface. These deeper penetration show that more Si is etched into the gas phase from these locations.

13. The microcones/microcolumns grow by deposition of Si from the vapor phase at their molten tips. The surface ridges evolve in prime locations for the growth of cones and columns because the densest flux of Si emerges from the adjacent fractures and pits. The vapor phase deposition occurs by a "catalyst-free" VLS mechanism. The laser pulse acts to simultaneously produce the flux of Si required for deposition and melt the tips of the microcolumns and microcones providing the deposition location.

14. The sides of the microcones and microcolumns are molten for a very short time period, and in some cases not at all depending on cone/column morphology. The Si vapor deposits preferentially at the molten tips of the cones and columns because of the high accommodation coefficient of the liquid phase compared with the solid phase.

15. High pressures of Si vapor are present around the microcolumn and microcone tips. The high pressure, non-equilibrium conditions surrounding the tips cause them to supersaturate with Si. The molten tips attempt to reestablish equilibrium by depositing Si at the solid Si-liquid Si interface. The tips thus raise above the wafer as each additional pulse again supersaturates the liquid.

References

References

1. W. W. Duley, p. 6 and 36 in UV Lasers : Effects and Applications in Materials Science, Cambridge University Press, 1996.
2. D. J. Elliot, p. 48 in Ultraviolet Laser Technology and Applications, Academic Press, Inc., San Diego, 1995.
3. M. VonAllmen, p. 6 – 19 in Laser Beam and Electron Beam Processing of Materials, Academic Press, Inc., 1980.
4. G. E. Jellison Jr., D. H. Lowndes, D. N. Mashburn, and R. F. Wood, *Phys. Rev. B* **34(4)**, 2408 (1986).
5. D. E. Aspnes and A. A. Studna, *Phys. Rev. B* **27**, 985 (1985).
6. C. W. White and M. J. Aziz, "Energy Desposition, Heat Flow, and Rapid Solidification during Pulsed-Laser- and Electron Beam Irradiation of Metals" p. 21 – 22 in Surface Alloying by Ion, Electron, and Laser Beams, ASM International, Metals Park, Ohio, 1987
7. W. L. Brown, Laser and Electron Beam Processing of Materials, (C. W. White and P. S. Peercy, eds.) Academic Press, New York, 1980.
8. D. Bauerle, p. 15 – 28, 173 –190, 251 – 254, and 262 – 264, Laser Processing and Chemistry, 2nd Ed., Springer – Verlag, Berlin, Heidelburg, 1996.
9. C. Kittel, p. 98, Introduction to Solid State Physics, 7th Ed., John Wiley & Sons, New York, 1996.
10. J. B. Bruks, Photophysics of Aromatic Molecules, Wiley-Interscience, London, 1970.

11. R. E. Hummel, p. 207, Electronic Properties of Materials, 2nd Ed., Springer – Verlag, Berlin, Heidelburg, 1993.

12. G. B. Shinn, F. Steigerwald, H. Stiegler, R. Sauerbrey, F. K. Tittel, and W. L. Wilson Jr., *J. Vac. Sci. Technol. B* **4(6)**, 1273 (1986).

13. R. F. Wood and G. E. Jellison Jr., "Melting Model of Pulsed Laser Processing", p.204 in Semiconductors and Semimetals, Vol. 23, Pulsed Laser Processing of Semiconductors (R. F. Wood, C. W. White, and R. T. Young, eds.), Academic Press Inc., Orlando, 1984.

14. S. De Unamuno and E. Fogarassy, *Appl. Sur. Sci.* **36**, 1 (1989).

15. R. Kelly, A. Miotello, B. Braren, A. Gupta, and K. Casey, *Nucl. Instrum. Meth. Phys. Res. B* **65**, 187 (1992).

16. I. Miyamoto and H. Maruo, *Proc. SPIE* **1279**, 66 (1990).

17. D. J. Krajnovich and J. E. Vazquez, *J. Appl. Phys.* **73(6)**, 3001 (1993).

18. S. R. Foltyn, R. E. Muenchausen, R. C. Estler, E. Peterson, W. B. Huthcinson, K. C. Ott, N. S. Nogar, K. M. Hubbard, R. C. Dyer, and K. D. Wu, *Appl. Phys. Lett.* **59(5)**, 594 (1990).

19. T. Aselage and K. Keefer, *J. Mater. Res.* **3(6)**, 1279 (1988).

20. S. Ono, S. Nakaoka, J. Wang, H. Ninno, and A. Yabe, *Jpn. J. Appl. Phys. Vol.* **36**, 1387 (1997).

21. S. R. Foltyn, "Surface Modification of Materials by Cumulative Laser Irradiation" p. 89 –113 in Pulsed Laser Deposition of Thin Films (D. B. Chrisey and G. K. Hubler, eds.) Wiley – Interscience, New York, 1994.

22. R. K. Singh and J. M. Fitz-Gerald, *Nucl. Instrum. Meth. Phys. Res. B* **121**, 363 (1997).

23. M. L. Dawes, J. T. Dickinson, L. C. Jensen, and S. C. Langford, *Nanotechnology* **5**, 101 (1994).

24. D. Ghose, D. Basu, and S. B. Karmohapatro, *Nucl. Instrum. Meth. Phys. Res. B* **1**, 26 (1984).

25. R. Kelly, J. J. Cuomo, P. A. Leary, J. E. Rothenburg, B. E. Braren, and C. F. Aliotta, *Nucl. Instrum. Meth. B* **9**, 329 (1985).

26. H. Keilmann and Y. H. Bai, *Appl. Phys. A* **29**, 9 (1982).

27. J. F. Young, J. E. Sipe, and H. M. van Driel, *Phys. Rev. B* **30(4)**, 2001 (1984).

28. J. E. Rothenburg and R. Kelly, *Nucl. Instrum. Meth. B* **1**, 291 (1984).

29. F. Sanchez, J. L. Morenza, R. Aguiar, J. C. Delgado, and M. Varela, *Appl. Phy. A* **66**, 83 (1998).

30. I. Noorbacha, R. R. Lucchese, and Y. Zeiri, *J. Chem. Phys.* **89**, 5251 (1988).

31. H. D. Young, p. 460 – 465, 470 in University Physics with Modern Physics, Addison-Wesley Publishing Company, Massachusetts, 1992.

32. K. L. Saenger, "Angular Distribution of Ablated Material" p. 199 – 227 in Pulsed Laser Deposition of Thin Films (D. B. Chrisey and G. K. Hubler, eds.) Wiley – Interscience, New York, 1994.

33. R. D. Benedict, p. 60 – 72, Fundamentals of Gas Dynamics, John Wiley & Sons, Inc., New York, 1983.

34. M. Hanabusa and M. Suzuki, *Mater. Res. Soc. Symp. Proc.* **4**, 559 (1982).

35. M. M. Bialkowskil, G. S. Hurst, J. E. Parks, D. H. Lowndes, and G. E. Jellison, Jr., *J. Appl. Phys.* **68(9)**, 4795 (1990).

36. D. B. Geohegan, *Mater. Res. Soc. Symp. Proc.* **201**, 557 (1991).

37. I. A. Movtchan, W. Marine, R. W. Dreyfus, H. C. Le, M. Sentis, and M. Autric, *Appl. Sur. Sci.* **96 – 98**, 251 (1996).

38. H. C. Le, R. W. Dreyfus, W. Marine, M. Sentis, and I. A. Movtchan, *Appl. Sur. Sci.* **96 – 98**, 164 (1996).

39. I. A. Movtchan, R. W. Dreyfus, W. Marine, M. Sentis, M. Autric, G. Le Lay, and N. Merk, *Thin Solid Films* **255**, 286 (1995).

40. D. B. Geohegan, A. A. Puretzky, G. Dusher, and S. J. Pennycook, *Appl. Phys. Lett.* **73(4)**, 438 (1998).

41. R. S. Wagner and W. C. Ellis, *Appl. Phys. Lett.* **4(5)**, 84 (1964).

42. D. R. Lide, p. 4-122, CRC Handbook of Chemistry and Physics, 79th Ed., 1998 – 1999, CRC Press, Boca Raton, 1998.

43. R. S. Wagner, "VLS Mechanism of Crystal Growth", p. 47 – 119 in Whisker Technology (A. P. Levitt, ed.) Wiley – Interscience, New York, 1970.

44. E. I. Givargizov, "Growth of Whiskers by the Vapor-Liquid-Solid Mechanism", p. 79 – 145 in Series : Current Topics in Materials Science, Vol. 1 (E. Kaldis, ed.), North – Holland, Amsterdam, 1978.

45. J. Westwater, D. P. Gosain, and S. Usui, *Jpn. J. Appl. Phys. Vol.* **31**, *pt. 1, no. 10* (1997).

46. J. P. Hirth and G. M. Pound, *J. Phys. Chem.* **64**, 619 (1960).

47. J. P. Hirth and G. M. Pound, *Progr. Mater. Sci.* **11**, 107 (1963).

48. E. I. Givargizov, *J. Crys. Growth* **20**, 217 (1973).

49. E. I. Givargizov, A. N. Kiselev, L. N. Oblenskaya, and A. N. Stepanova, *Appl. Sur. Sci.* **67**, 73 (1993).

50. R. B. Marcus, T. S. Ravi, T. Gmitter, K. Chin, D. Liu, W. J. Orvis, D. R. Ciarlo, C. E. Hunt, and J. Trujillo, *Appl. Phys. Lett.* **56**, 236 (1990).

51. V. S. Aliev, V. N. Kruchinin, and M. R. Baklanov, *Sur. Sci.* **347**, 97 (1996).

52. H. F. Winters and J. W. Coburn, *Sur. Sci. Rep.* **14**, 190 (1992).

53. M. Seel and P. S. Bagus, *Phys. Rev. B* **28**, 2023 (1983).

54. F. R. McFreely, J. F. Morar, and F. J. Himpsel, *Surf. Sci.* **165**, 277 (1986).

55. H. F. Winters and I. C. Plumb, *J. Vac. Sci. Technol. B* **9**, 197 (1991).

56. N. Cabrera and N. F. Mott, *Rep. Prog. Phys.* **12**, 163 (1949).

57. K. Ohkubo, Y. Igari, S. Tomoda, and I. Kusunoki, *Sur. Sci.* **260**, 44 (1992).

58. K. G. Nakamura, H. Kuroki, and M. Kitajima, *J. Appl. Phys.* **75**(8), 4261 (1994)

59. Dr. A. J. Pedraza, private communication.

60. Dr. D. H. Lowndes, HR-SEM & EDS on Si microcolumns

61. P. R. Herman, B. Chen, D. J. Moore, and M. Canaga – Retnam, *Mater. Res. Soc. Symp. Proc.* **236**, 53 (1992)

62. R. A. B. Devine, C. Fiori, and J. Robertson, *Mater. Res. Soc. Symp. Proc.* **61**, 177 (1986)

63. A. J. Pedraza, *Nucl. Instrum. Meth.* **B(141)**, 709 (1998)

64. R. Kelly and A. Miotello, "Mechanisms of Pulsed Laser Sputtering" p. 54 – 87 in Pulsed Laser Deposition of Thin Films (D. B. Chrisey and G. K. Hubler, eds.) Wiley – Interscience, New York, 1994.

65. V. Yu Balandin, D. Otte, and O. Bostanjoglo, *J. Appl. Phys.* **78**(3), 2037 (1995)

66. N. Oldham and A. J. Pedraza, SEM on Si microcones

67. A. Dauscher, V. Feregotto, P. Cordier, and A. Thomy, *Appl. Sur. Sci.* **96 – 98**, 410 (1996)

68. J.E. Sipe, J. F. Young, J. S. Preston, and H. M. van Driel, *Phys. Rev.* B **27**, 1141 (1983)

69. M. Wolf, *J. Vac. Sci. Technol.* **12**, 984 (1975)

70. D. L. Smith, "Gas Kinetics" p. 9 – 34 in Thin Film Deposition, Principles & Practice McGraw Hill, Inc., New York, 1995

71. Y. Matsumi, S. Toyoda, T. Hayashi, M. Miyamura, H. Yoshikawa, and S. Komiya, *J. Appl. Phys.* **60**(12), 4102 (1986)

72. S. Vanhaelemeersch, J. Van. Hoeymissen, D. Vermeylen, and J. Peters, *J. Appl. Phys.* **70**(7), 3892 (1991)

73. V. M. Donnelly and D. L. Flamm, *J. Appl. Phys.* **51**, 5273 (1980)

74. R. L. Webb, L. C. Jensen, S. C. Langford, and J. T. Dickenson, *J. Appl. Phys.* **74**(4), 2323 (1993)

Vita

Jason Fowlkes was born in Wytheville, Virginia on August 10, 1974. He graduated from George Wythe High School in Wytheville in 1992 and entered the engineering program at the University of Alabama, Tuscaloosa that same year. After two years in the Metallurgical Engineering department at U.A. he transferred to the University of Tennessee, Knoxville where he completed the requirements for his Bachelor of Science degree in Materials Science and Engineering.

Following completion of his Masters of Science degree, Jason plans to continue his studies at the University of Tennessee by pursuing a Ph.D. degree in Materials Science and Engineering. His work will be a continuation of the work presented in this Masters thesis.